

COPPER NANOWIRE NETWORK BASED TRANSPARENT THIN FILM  
HEATERS

A THESIS SUBMITTED TO  
THE GRADUATE SCHOOL OF NATURAL AND APPLIED SCIENCES  
OF  
MIDDLE EAST TECHNICAL UNIVERSITY

BY

DOĞANCAN TİGAN

IN PARTIAL FULFILLMENT OF THE REQUIREMENTS  
FOR  
THE DEGREE OF MASTER OF SCIENCE  
IN  
METALLURGICAL AND MATERIALS ENGINEERING

SEPTEMBER 2018



Approval of the thesis

**COPPER NANOWIRE NETWORK BASED TRANSPARENT THIN FILM  
HEATERS**

submitted by **DOĞANCAN TİGAN** in partial fulfillment of the requirements for the degree of **Master of Science in Metallurgical and Materials Engineering Department, Middle East Technical University** by,

Prof. Dr. Halil Kalıpçılar  
Dean, Graduate School of **Natural and Applied Sciences** \_\_\_\_\_

Prof. Dr. C. Hakan Gür  
Head of Department, **Metallurgical and Mat. Eng. Dept.** \_\_\_\_\_

Prof. Dr. H. Emrah Ünalın  
Supervisor, **Metallurgical and Mat. Eng. Dept., METU** \_\_\_\_\_

Assist. Prof. Dr. Bilge İmer  
Co-Supervisor, **Metallurgical and Mat. Eng. Dept., METU** \_\_\_\_\_

**Examining Committee Members:**

Prof. Dr. Cevdet Kaynak  
Metallurgical and Mat. Eng. Dept., METU \_\_\_\_\_

Prof. Dr. H. Emrah Ünalın  
Metallurgical and Mat. Eng. Dept., METU \_\_\_\_\_

Assist. Prof. Dr. Bilge İmer  
Metallurgical and Mat. Eng. Dept., METU \_\_\_\_\_

Assoc. Prof. Dr. E. Gökem Günbaşı  
Chemistry Dept., METU \_\_\_\_\_

Assoc. Prof. Dr. Jongee Park  
Metallurgical and Mat. Eng. Dept., Atılım University \_\_\_\_\_

**Date:** \_\_\_\_\_ 04.09.2018 \_\_\_\_\_

**I hereby declare that all information in this document has been obtained and presented in accordance with academic rules and ethical conduct. I also declare that, as required by these rules and conduct, I have fully cited and referenced all material and results that are not original to this work.**

Name, Last name: Dođancan Tigan

Signature:

## ABSTRACT

### COPPER NANOWIRE NETWORK BASED TRANSPARENT THIN FILM HEATERS

Tigan, Dođancan  
MSc, Department of Metallurgical and Materials Engineering  
Supervisor: Prof. Dr. H. Emrah Ünalán  
Co-Supervisor: Assist. Prof. Dr. Bilge İmer

September 2018, 103 pages

Metallic nanowire random networks are highly promising as transparent thin film heaters (TTFHs) due to their significant optoelectronic performance and thermal conductivity. Typically silver nanowires (Ag NWs) are utilized as TTFHs but in recent years, copper nanowires (Cu NWs) started to replace them in many applications as an economic alternative. The electrical conductivity of Cu is almost equal to that of Ag and it is much cheaper than Ag at least in bulk form. However, stability of Cu NWs is a lot poor compared to that of Ag NWs due to ease of oxidation upon air exposure. The problem gets even worse at elevated temperatures considering TTFH applications. Therefore, a protection layer to be deposited onto Cu NW networks is necessary for their large scale utilization in TTFHs. In this study, aluminum oxide ( $\text{Al}_2\text{O}_3$ ) and zinc oxide (ZnO) shells were deposited onto Cu NW networks by atomic layer deposition (ALD) method. Cu NW networks with a sheet resistance of  $10 \text{ } \Omega/\text{sq}$  failed only after attaining a temperature of  $100 \text{ } ^\circ\text{C}$  due to oxidation. On the other hand, deposition of only  $5 \text{ nm}$   $\text{Al}_2\text{O}_3$  and ZnO shell layers onto Cu NW networks ( $10 \text{ } \Omega/\text{sq}$  sheet resistance at  $80.8\%$  transmittance and  $15 \text{ } \Omega/\text{sq}$  sheet resistance at  $84.4\%$  transmittance) increased the maximum attainable temperatures to  $153 \text{ } ^\circ\text{C}$  and  $139 \text{ } ^\circ\text{C}$ , respectively. This was a clear indication of oxidation protection by the deposition of the shell layer onto Cu NW networks. Moreover, in order to further increase the protection level, the effect of oxide shell

thickness was investigated in sacrifice of network transmittance. Attained maximum temperatures were increased up to 309 °C and 237 °C for 50 nm thick Al<sub>2</sub>O<sub>3</sub> and ZnO shell layers on Cu NW networks, respectively. Moreover, prominent heating rates of 14 °C/s and 12 °C/s were obtained from these core shell networks with Al<sub>2</sub>O<sub>3</sub> and ZnO shells, respectively. Finally, an extensive parametric study on NW density, type and thickness of metal oxide shells in comparison to optoelectronic properties of networks and their thermal response is reported. The performance of the networks reported herein lie among the highest achieved for Cu NW TTFHs. In order to demonstrate the feasibility of these networks as TTFHs in a real life application, they were utilized as defrosters.

Keywords: transparent thin film heaters, copper nanowires, atomic layer deposition.

## ÖZ

### BAKIR NANOTEL AĞLAR ESASLI ŞEFFAF İNCE FİLM ISITICILAR

Tigan, Dođancan  
Yüksek Lisans, Metalurji ve Malzeme Mühendisliđi Bölümü  
Tez Yöneticisi: Prof. Dr. H. Emrah Ünalın  
Ortak Tez Yöneticisi: Yrd. Doç. Dr. Bilge İmer

Eylül 2018, 103 sayfa

Metalik nanotel rasgele ağlar, önemli optoelektronik performansları ve termal iletkenlikleri nedeniyle şeffaf ince film ısıtıcılar olarak oldukça ümit vericidir. Tipik olarak gümüş nanoteller şeffaf ince film ısıtıcı olarak kullanılmakta, ancak son yıllarda, bakır nanoteller ekonomik bir alternatif olarak şeffaf ince film ısıtıcı olarak gümüş nanotellerin yerini almıştır. Bakırın elektrik iletkenliđi neredeyse gümüşünkine eşittir ve gümüşten çok daha ucuzdur. Bununla birlikte, bakır nanotellerin stabilitesi, hava ile temasında oksidasyon kolaylıđı nedeniyle gümüş nanotellere kıyasla çok zayıftır. Şeffaf ince film ısıtıcılar göz önüne alındığında bu sorun yüksek sıcaklıklarda daha da kötüleşir. Bu nedenle, bakır nanotel ağlarına biriktirilecek bir koruma katmanı, şeffaf ince film ısıtıcı olarak büyük ölçekli kullanımlar için gereklidir. Bu çalışmada, alüminyum oksit ( $Al_2O_3$ ) ve çinko oksit ( $ZnO$ ) kabukları, bakır nanotel ağlarına atomik katman biriktirme yöntemi ile çökeltilmiştir.  $10 \Omega/sq$ 'lik bir levha direncine sahip bakır nanotel ağları, oksidasyona bađlı olarak ancak  $100 \text{ }^\circ C$ 'lik bir sıcaklıđa ulaşıldıktan sonra başarısız olmuştur. Diđer yandan, sadece 5 nm bakır nanotel ağları üzerine  $Al_2O_3$  ve  $ZnO$  kabuk tabaka kaplamaları ( $10 \Omega/sq$  levha direnci %80.8 şeffaflık ve 15 levha direnci %84.4 şeffaflık) maksimum ulaşılabilir sıcaklıkları sırası ile  $153 \text{ }^\circ C$  ve  $139 \text{ }^\circ C$ 'ye çıkarmıştır. Bu, kabuk katmanının bakır nanotel ağlarına çökertilmesiyle oksidasyon korumasının açık bir göstergesidir. Ayrıca, koruma seviyesini daha da artırmak için, oksit kabuk kalınlıđının etkisi, şeffaflık uğrunda araştırılmıştır. Elde edilen

maksimum sıcaklıklar sırasıyla bakır nanotel ağlarında 50 nm kalınlığındaki  $Al_2O_3$  ve ZnO kabuk tabakaları için 309 °C ve 237 °C'ye yükselmiştir. Ayrıca, bu çekirdek kabuk ağlarından  $Al_2O_3$  ve ZnO kabuk tabakaları için sırasıyla 14 °C/s ve 12 °C/s'lik belirgin ısıtma oranı elde edilmiştir. Son olarak ağların optoelektronik özelliklerine göre nanotel yoğunluğu, metal oksit kabuklarının tipi ve kalınlığı üzerine yapılan kapsamlı bir parametrik çalışma ve bunların termal tepkisi rapor edilmiştir. Burada bildirilen ağların performansı, bakır nanotel ağları esaslı şeffaf ince film ısıtıcılar için elde edilen en yüksek oranlar arasında yer almaktadır. Gerçek bir yaşam uygulamasında bu ağların şeffaf ince film ısıtıcılar olarak uygulanabilirliğini göstermek için, buz çözücü olarak kullanılmıştır.

Anahtar kelimeler: şeffaf ince film ısıtıcılar, bakır nanoteller, atomik katman biriktirme.

To my parents

## ACKNOWLEDGEMENTS

This work was financially supported by Middle East Technical University, Scientific Research Projects Programme under project numbers BAP-07-02-2016-003, BAP-07-02-2017-011 and BAP-07-02-2017-004-265.

Firstly, I would like to express my deepest appreciation to my advisor Prof. Dr. H. Emrah Ünal for his support, guidance and patience throughout the study. It is a great honor to work under his supervision. I want to express my special thanks to Assist. Prof. Dr. Bilge İmer for her guidance and support throughout my study.

I am also thankful to my research partner Sevim Polat Genlik for her both emotional and technical support throughout my study. Without her, I have already given up. I would also like to express my special thanks to Onur Türel, Ece Alpuğan, Mete Batuhan Durukan and Selin Özkul for their intimate friendship. I would like to thank my lab mates Recep Yüksel, Alptekin Aydın, Şahin Coşkun, Doğa Doğanay, Pantea Aurang, Yusuf Tutel, İpek Bayraktar, İtir Bakış Doğru, Şeyma Koç, Selen Yüksel, Şensu Tunca, Serkan Koylan, Efe Boyacıgiller, Elif Özlem Güner and Özlem Ünal. I always feel lucky to be a part of this productive research group. I am thankful to Bersu Baştuğ and Özlem Ünal for their help in UV-VIS analysis.

I would also like to thank Mert Koçer, Gülce Öngör, Beril Arı, Ezgi Güleç, Ahmet Kuzucanlı and Esra Kaderli for their intimate friendship and emotional support.

Finally, I must express my very profound gratitude to my parents, Şahin Tigan and Melek Tigan for providing me unfailing support and encouragement throughout my study. This thesis would not have been possible without them.

## TABLE OF CONTENTS

ABSTRACT .....	v
ÖZ .....	vii
ACKNOWLEDGEMENTS .....	x
TABLE OF CONTENTS .....	xi
LIST OF TABLES .....	xiv
LIST OF FIGURES .....	xv
LIST OF ABBREVIATIONS .....	xix
CHAPTERS	
1. INTRODUCTION .....	1
1.1. Transparent Conductors.....	1
1.2. Transparent Thin Film Heaters.....	2
1.2.1. Working Principle of Transparent Thin Film Heaters .....	3
1.2.2. Transparent Thin Film Heater Materials .....	4
1.2.2.1. Metal Oxides .....	4
1.2.2.2. Carbon Nanotube Networks .....	11
1.2.2.3. Graphene .....	12
1.2.2.4. Metal Nanowire Random Networks .....	14
1.2.2.5. Hybrid Materials .....	28
1.2.2.6. Metal Mesh .....	31
1.3. Motivation for This Thesis .....	33
2. EXPERIMENTAL DETAILS .....	35

2.1. Synthesis of Copper Nanowires .....	35
2.2. Fabrication of Copper Nanowire Networks .....	37
2.3. Contact Formation with Physical Vapor Deposition.....	38
2.4. Atomic Layer Deposition onto Copper Nanowire Networks.....	39
2.5. Characterization Methods .....	40
2.5.1. Scanning Electron Microscopy (SEM).....	40
2.5.2. Transmission Electron Microscopy (TEM).....	40
2.5.3. Sheet Resistance Measurements .....	40
2.5.4. Transparency Measurements .....	41
2.5.5. Areal Mass Density Calculations .....	41
2.5.6. X-Ray Diffraction (XRD) Analysis.....	43
2.5.7. X-Ray Photoelectron Spectroscopy (XPS) Analysis.....	43
2.5.8. Atomic Force Microscopy (AFM).....	43
2.5.9. Ellipsometry Measurements .....	44
2.5.10. Thermal Measurements .....	44
2.5.11. Thermal Camera Imaging.....	46
3. RESULTS AND DISCUSSION .....	47
3.1. Characterization of Cu NWs .....	47
3.2. Effect of Nanowire Density on Optoelectronic Properties.....	49
3.3. Bare Copper Nanowire Networks .....	50
3.3.1. Thermal Measurements .....	53
3.4. Aluminum Oxide Deposited Copper Nanowire Networks .....	56
3.4.1. Thermal Measurements .....	59
3.4.2. Repetitive Heating and Cooling Cycles.....	64
3.4.3. Long Term Stability.....	65

3.4.4. Failure Mechanism .....	66
3.4.5. Thermal Imaging.....	69
3.4.6. Defrosting Application .....	70
3.5. Zinc Oxide Deposited Copper Nanowire Networks.....	71
3.5.1. Thermal Measurements.....	78
3.5.2. Failure Mechanism .....	83
4. CONCLUSIONS AND FUTURE RECOMMENDATIONS .....	87
4.1. Conclusions .....	87
4.2. Future Recommendations.....	88
REFERENCES.....	91

## LIST OF TABLES

### TABLES

<b>Table 1. 1</b> The comparison of five common production methods for metal NW networks. The number of plus signs indicate the suitability of the process.[60].....	15
<b>Table 1. 2</b> Properties of hybrid TTFHs (PEDOT:PSS: poly(3,4 - ethylenedioxythiophene) polystyrene sulfonate, HRP: Heat Resistant Polymer, PVA: poly(vinyl alcohol), PMMA: poly(methyl methacrylate)).....	29
<b>Table 1. 3</b> Comparison chart for different TTFH materials [20]. .....	34
<b>Table 3. 1</b> Optoelectronic properties and thermal response characteristics of bare Cu NW networks with different amds used in this work. ....	56
<b>Table 3. 2</b> Optoelectronic properties and thermal response characteristics of Al <sub>2</sub> O <sub>3</sub> deposited Cu NW networks with different amds and different Al <sub>2</sub> O <sub>3</sub> thicknesses....	63
<b>Table 3. 3</b> R <sub>a</sub> and RMS values of Al <sub>2</sub> O <sub>3</sub> and ZnO thin films with different thicknesses. ....	73
<b>Table 3. 4</b> Optoelectronic properties and thermal response characteristics of Cu NW networks with different amds and ZnO thicknesses. ....	81

## LIST OF FIGURES

### FIGURES

<b>Figure 1. 1</b> Photographs of SWNT based TTFH (a) before frost formation, (b) after frost formation and (c) defrosting application at an applied bias of 30V [16].....	2
<b>Figure 1. 2</b> Classification of TTFH materials in chronological order [20]. .....	4
<b>Figure 1. 3</b> The ternary TCO compounds between In, Sn, Zn and O <sub>2</sub> [27]. .....	5
<b>Figure 1. 4</b> The effect of ITO thin film thicknesses on (a) sheet resistance and (b) optical transmittance spectra [30]. .....	6
<b>Figure 1. 5</b> Time dependent thermal behavior of solution deposited ITO TTFH under 3 different applied biases [31].....	7
<b>Figure 1. 6</b> Time dependent thermal behavior of FTO based TTFH under an applied bias of 12 V for 120 minutes [37]. .....	9
<b>Figure 1. 7</b> The time dependent thermal response of GZO based TTFHs under an applied bias of 12 V and the relationship between temperature and applied voltage [43]. .....	10
<b>Figure 1. 8</b> The relationship between (a) optical transmittance and sheet resistance with respect to number of layers. (b) Attained temperatures with respect to applied voltages for MWCNT based TTFHs [50]. .....	12
<b>Figure 1. 9</b> The time dependent thermal response of AuCl <sub>3</sub> and HNO <sub>3</sub> doped 4 layers of graphene and ITO under an applied bias of 12 V [51].....	13
<b>Figure 1. 10</b> Graphs showing the relationship between (a) sheet resistance and area fraction, (b) transmittance and sheet resistance for different L/D ratios [64]. .....	16
<b>Figure 1. 11</b> Thermal response of (a) thin films with 3 different sheet resistances under an applied bias of 4 V. Thermal response of Ag NW networks with sheet resistances of (b) 4.3, (c) 25 and (d) 30 Ω/sq [74]. .....	19
<b>Figure 1. 12</b> The general oxidation reaction of glucose with the help of HDA [79].	21
<b>Figure 1. 13</b> Schematic illustration of ALD process cycle, which consists of (a) first half reaction, (b) purging of by-products, (c) second half reaction and (d) purging of by-products [90]. .....	25

<b>Figure 1. 14</b> Schematics showing oxidation behavior of bare Cu NFs and AZO / Al <sub>2</sub> O <sub>3</sub> deposited Cu NFs [89].....	26
<b>Figure 1. 15</b> SEM micrographs of Ag NW networks (a) that are as deposited, annealed at (b) 100, (c) 200, (d) 300, (e) 400 and (f) 500 °C [7].....	28
<b>Figure 1. 16</b> Thermal response of networks with (a) 6.1 Ω/sq and (b) 17 Ω/sq sheet resistance, under various applied voltages [98]. .....	30
<b>Figure 1. 17</b> Time dependent thermal behavior of Cu mesh based TTFH under different applied voltages [103]. .....	32
<b>Figure 2. 1</b> Photographs of Cu NW solutions before and after the synthesis with Teflon lined autoclave.....	36
<b>Figure 2. 2</b> Spray deposition of Cu NWs onto quartz substrates. ....	37
<b>Figure 2. 3</b> Parallel Ag thin film contacts deposited onto Cu NW network. ....	38
<b>Figure 2. 4</b> Illustration of the thermal measurement setup used in this work. ....	45
<b>Figure 3. 1</b> A SEM image of Cu NW network on Si wafer substrate.....	47
<b>Figure 3. 2</b> (a) Diameter and (b) length distributions of synthesized Cu NWs in this work. ....	48
<b>Figure 3. 3</b> (a) Cross sectional TEM image of an individual Cu NW and (b) XRD pattern for as synthesized Cu NWs.....	48
<b>Figure 3. 4</b> (a) Sheet resistance and (b) optical transmittance with respect to amd within the Cu NW networks fabricated in this work. ....	49
<b>Figure 3. 5</b> Transmittance versus sheet resistance graph for Cu NW networks fabricated in this work. ....	50
<b>Figure 3. 6</b> SEM images of Cu NW networks with amds of (a) 68.8, (b) 101.2 and (c) 142.0 mg/m <sup>2</sup> . All scales are the same.....	51
<b>Figure 3. 7</b> Spectral transmittance of Cu NW networks with amds of 68.8, 101.2 and 142.0 mg/m <sup>2</sup> used in this work for Al <sub>2</sub> O <sub>3</sub> deposition.....	51
<b>Figure 3. 8</b> SEM images of Cu NW networks with amds of (a) 40.7, (b) 73.1 and (c) 101.6 mg/m <sup>2</sup> . All scales are the same. ....	52

<b>Figure 3. 9</b> Spectral transmittance of Cu NW networks with amds of 40.7, 73.1 and 101.6 mg/m <sup>2</sup> used in this work for ZnO thin film deposition. ....	53
<b>Figure 3. 10</b> Time dependent thermal responses of Cu NW networks with different amds of (a) 40.7, (b) 68.8, (c) 73.1, (d) 101.2, (e) 101.6 and (f) 142.0 mg/m <sup>2</sup> under various applied voltages. ....	54
<b>Figure 3. 11</b> (a) SEM and (b) TEM images of an individual 50 nm Al <sub>2</sub> O <sub>3</sub> deposited Cu NW. ....	56
<b>Figure 3. 12</b> Spectral transmittance of Cu NW networks with an amd of 68.8 mg/m <sup>2</sup> and different Al <sub>2</sub> O <sub>3</sub> thicknesses of 5, 15, 25 and 50 nm. ....	57
<b>Figure 3. 13</b> XPS spectra of (a) Cu2p <sub>1/2</sub> and Cu2p <sub>3/2</sub> , (b) Cu LMM Auger and (c) Cu3p and Al2p for 5 nm Al <sub>2</sub> O <sub>3</sub> deposited Cu NW network. ....	58
<b>Figure 3. 14</b> Time dependent thermal response of Al <sub>2</sub> O <sub>3</sub> deposited Cu NW networks with an amd of 68.8 mg/m <sup>2</sup> and different Al <sub>2</sub> O <sub>3</sub> thicknesses of (a) 5, (b) 15, (c) 25 and (d) 50 nm. ....	60
<b>Figure 3. 15</b> Time dependent thermal response of 50 nm Al <sub>2</sub> O <sub>3</sub> deposited Cu NW networks with different amds of (a) 101.2 and (b) 142.0 mg/m <sup>2</sup> . ....	61
<b>Figure 3. 16</b> Heating and cooling rate as a function of time for Cu NW network with an amd of 68.8 mg/m <sup>2</sup> and Al <sub>2</sub> O <sub>3</sub> thickness of 50 nm under an applied bias of 11 V. ....	62
<b>Figure 3. 17</b> Thermal response of 25 nm Al <sub>2</sub> O <sub>3</sub> deposited Cu NW network with an amd of 68.8 mg/m <sup>2</sup> under repetitive heating and cooling cycles with an applied bias of 7 V. ....	64
<b>Figure 3. 18</b> Long term thermal response of 25 nm Al <sub>2</sub> O <sub>3</sub> deposited Cu NW network with an amd of 68.8 mg/m <sup>2</sup> under an applied bias of 6 V. ....	65
<b>Figure 3. 19</b> XPS spectra of (a) Cu2p <sub>1/2</sub> and Cu2p <sub>3/2</sub> , (b) Cu LMM Auger, and (c) Cu3p and Al2p of 5 nm Al <sub>2</sub> O <sub>3</sub> deposited Cu NW network at failed points. ....	67
<b>Figure 3. 20</b> SEM images of failed Cu NW networks with an amd of 68.8 mg/m <sup>2</sup> with different Al <sub>2</sub> O <sub>3</sub> thicknesses of (a) 5, (b) 15, (c) 25 and (d) 50 nm. ....	68
<b>Figure 3. 21</b> Thermal camera images of the Cu NW network with an amd of 68.8 mg/m <sup>2</sup> and 50 nm Al <sub>2</sub> O <sub>3</sub> thickness (a) before (10 V applied bias) and (b) after (11 V applied bias) failure. ....	69

<b>Figure 3. 22</b> Photos of the 5 nm Al <sub>2</sub> O <sub>3</sub> deposited Cu NW network with an amd of 68.8 mg/m <sup>2</sup> (a) before and (b) after defrosting application. ....	70
<b>Figure 3. 23</b> (a) SEM and (b) TEM images of an individual 50 nm ZnO deposited Cu NW. ....	71
<b>Figure 3. 24</b> (a) 3D and (b) 2D topographical AFM images of Al <sub>2</sub> O <sub>3</sub> thin film. (c) 3D and (d) 2D topographical AFM images of ZnO thin film. ....	72
<b>Figure 3. 25</b> Spectral transmittance of Cu NW networks with an amd of 40.7 mg/m <sup>2</sup> and different ZnO thicknesses of 5, 15, 25 and 50 nm. ....	74
<b>Figure 3. 26</b> Refractive index (n) as a function of the wavelength for (a) Al <sub>2</sub> O <sub>3</sub> and (b) ZnO thin films. ....	75
<b>Figure 3. 27</b> GIXD patterns for bare (a) Al <sub>2</sub> O <sub>3</sub> and (b) ZnO thin films on quartz substrates. ....	76
<b>Figure 3. 28</b> XPS spectra of (a) Cu2p <sub>1/2</sub> and Cu2p <sub>3/2</sub> , (b) Cu LMM Auger, and (c) Zn p <sub>1/2</sub> and Zn p <sub>3/2</sub> of 5 nm ZnO deposited Cu NW network. ....	77
<b>Figure 3. 29</b> Time dependent thermal response of ZnO deposited Cu NW networks with an amd of 40.7 mg/m <sup>2</sup> and different ZnO thicknesses of (a) 5, (b) 15, (c) 25 and (d) 50 nm. ....	78
<b>Figure 3. 30</b> Time dependent thermal responses under various applied voltages of 50 nm ZnO deposited Cu NW networks with different amds of (a) 73.1 and (b) 101.6 mg/m <sup>2</sup> . ....	79
<b>Figure 3. 31</b> Heating and cooling rate as a function of time for Cu NW network with an amd of 101.6 mg/m <sup>2</sup> and ZnO thickness of 50 nm under an applied bias of 7 V. ....	80
<b>Figure 3. 32</b> (a) The sheet resistance, (b) transmittance, (c) T <sub>max</sub> and (d) input power densities of Cu NW networks with amds of 101.2 mg/m <sup>2</sup> (for Al <sub>2</sub> O <sub>3</sub> deposition) and 101.6 mg/m <sup>2</sup> (for ZnO deposition) with different oxide thicknesses. Lines are for visual aid. ....	82
<b>Figure 3. 33</b> XPS spectra of (a) Cu2p <sub>1/2</sub> and Cu2p <sub>3/2</sub> , (b) Cu LMM Auger and (c) Zn p <sub>1/2</sub> and Zn p <sub>3/2</sub> of 5 nm ZnO deposited Cu NW network at failed points. ....	84
<b>Figure 3. 34</b> SEM images of Cu NW networks with an amd of 40.7 mg/m <sup>2</sup> and ZnO thicknesses of (a) 5, (b) 15, (c) 25 and (d) 50 nm, at failed points. ....	85

## LIST OF ABBREVIATIONS

<b>AFM</b>	Atomic Force Microscopy
<b>Ag</b>	Silver
<b>Al</b>	Aluminum
<b>Al<sub>2</sub>O<sub>3</sub></b>	Aluminum Oxide
<b>ALD</b>	Atomic Layer Deposition
<b>amd</b>	Areal Mass Density
<b>Au</b>	Gold
<b>AZO</b>	Aluminum doped Zinc Oxide
<b>CNT</b>	Carbon Nanotube
<b>Cu</b>	Copper
<b>CVD</b>	Chemical Vapor Deposition
<b>F</b>	Fluorine
<b>FTO</b>	Fluorine doped Tin Oxide
<b>GIXD</b>	Grazing Incidence X-ray Diffraction
<b>GZO</b>	Galium doped Zinc Oxide
<b>HDA</b>	Hexadecylamine
<b>In</b>	Indium
<b>In<sub>2</sub>O<sub>3</sub></b>	Indium Oxide
<b>ITO</b>	Indium Tin Oxide
<b>LCD</b>	Liquid Crystal Display
<b>LED</b>	Light Emitting Diode
<b>MWCNT</b>	Multi-walled Carbon Nanotube
<b>N<sub>c</sub></b>	Percolation Threshold
<b>NW</b>	Nanowire
<b>PVD</b>	Physical Vapor Deposition
<b>PVP</b>	Polyvinylpyrrolidone
<b>R<sub>s</sub></b>	Sheet Resistance
<b>SEM</b>	Scanning Electron Microscopy

<b>Sn</b>	Tin
<b>SnO<sub>2</sub></b>	Tin Oxide
<b>SWCNT</b>	Single-walled Carbon Nanotube
<b>TC</b>	Transparent Conductor
<b>TCO</b>	Transparent Conductive Oxide
<b>TEM</b>	Transmission Electron Microscopy
<b>TTFH</b>	Transparent Thin Film Heater
<b>ZnO</b>	Zinc Oxide

## CHAPTER 1

### INTRODUCTION

#### 1.1. Transparent Conductors

Transparent conductors (TCs) are simply thin films with high electrical conductivity and optical transparency. The terms used to define electrical conductivity and optical transparency for TCs are sheet resistance ( $R_s$  with unit  $\Omega/\text{sq}$ ) and percent transmittance (T, %). Generally, thin films having  $R_s$  below  $100 \Omega/\text{sq}$  and transmittance (at a wavelength of 550 nm) above 80% are accepted as TCs. The optical band gap of thin films must be above 3 eV to have optical transparency in visible portion of the spectra. The combination of electrical conductivity with this optical band gap criteria is hard to achieve in intrinsic stoichiometric oxides [1]. Therefore, non- stoichiometric oxides or doped oxides are used for TC applications [2]. The conventional TC material is indium tin oxide (ITO), which is the most widely used and commercialized transparent conductive oxide (TCO). Over the years, due to insufficient properties of ITO, alternative TCO materials are investigated extensively. Alternatives include other metal oxides such as fluorine doped tin oxide (FTO), aluminum doped zinc oxide (AZO), gallium doped zinc oxide (GZO) and antimony doped tin oxide (ATO) [3]. In addition to TCOs, TC materials could be made of electrically conductive discontinuous nanomaterial networks so that light can pass through the empty spaces between the networks. The examples of these types of TCs are carbon nanotube (CNT) networks [4], graphene [5] and metallic nanowire random networks [6]. The combination of electrical conductivity and optical transparency is easily achievable in these types of TCs.

In recent years, TCs had drawn a lot of attention due to the advancements in the optoelectronic industry. Excessive amount of applications and gadgets make use of TCs. The application areas include but not limited to panel displays, light emitting

diodes (LEDs) [7], solar cells, photodetectors [8], touch screens, electromagnetic interference (EMI) shields [9] and transparent heaters.

## 1.2. Transparent Thin Film Heaters

TTFHs are TCs that simply convert electrical energy to heat. TCs that can withstand high temperatures can be utilized as TTFHs. Therefore, as stated before general TTFH materials include metal oxides [10], CNT networks [11], graphene [12] and metallic nanowire random networks [13]. The application areas primarily include heating surfaces that require optical transmittance such as increasing the operating temperatures of liquid crystal displays (LCDs) in incompatible environments [14], defrosting and defogging of windows and displays [15]. The example photos of single-walled carbon nanotube (SWCNT) based TTFH used for defrosting is provided in Figure 1.1.



**Figure 1. 1** Photographs of SWCNT based TTFH (a) before frost formation, (b) after frost formation and (c) defrosting application at an applied bias of 30V [16].

### 1.2.1. Working Principle of Transparent Thin Film Heaters

Optical transmittance of TTFHs must be above 80%. This criterion is ensured by either an optical band gap of 3 eV or higher for metal oxides or letting light to pass through free spaces between nanomaterial networks. Operating mechanism of TTFHs simply relies on ‘‘Joule Heating’’ principle, where electrical energy is converted to heat. According to Joule heating, when voltage is applied to an electrical conductor, electric field is created. As a result of that, electrons are accelerated in the reverse direction of this electric field and create an electrical current. These electrons have kinetic energy due to acceleration and when they collide with the ions inside the electrical conductor, the particles are scattered randomly. Thermal motion becomes dominant and electrical energy is converted to heat consequently. The power of converted energy is calculated using Equation 1.1.

$$P = I \cdot V = \frac{V^2}{R} = I^2 R \quad (1.1)$$

,where  $P$  is power,  $V$  is voltage,  $I$  is the electrical current and  $R$  is the resistance of the conductor [17].

The power should be as high as possible for higher heat dissipation. When  $P = I^2 R$  is considered, for power to be maximum,  $I$  must be maximum and  $R$  must be minimum because  $I$  and  $R$  are inversely proportional as dictated by Ohms Law. While the converted energy is dissipated as radiation and convection from the heater material and the substrate, the remaining energy is left for conduction to heat the TTFH [18]. Therefore, higher power and heat dissipation means higher energy for conduction to heat the TTFH. At the same applied bias, TTFHs reach higher temperatures at lower resistances [19]. Since thin films are considered in this application, sheet resistance ( $R_s$ ) is more appropriate to use instead of resistance ( $R$ ). The relationship between  $R$  and  $R_s$  is given by Equation 1.2.

$$R = R_s \frac{L}{W} \quad (1.2)$$

, where  $L$  is the length and  $W$  is the width of the thin film if the thickness is considered as unity.

$R_s$  and  $R$  are directly proportional to each other thus in order the TTFH material to attain higher temperatures, thin films with  $R_s$  as low as possible are needed. Therefore, TC materials can be used as TTFHs since both  $R_s$  and optical transmittance values meet the requirements.

### 1.2.2. Transparent Thin Film Heater Materials

TTFHs evolved over the years in terms of electrical, optical and thermal performance thanks to vastly developing materials science field. Novel materials show promising performance improvements in TTFHs. Most common TTFH materials that are utilized by researchers over the years are provided in Figure 1.2. Detailed optoelectronic and thermal behaviors of these materials will be given in the following sections.

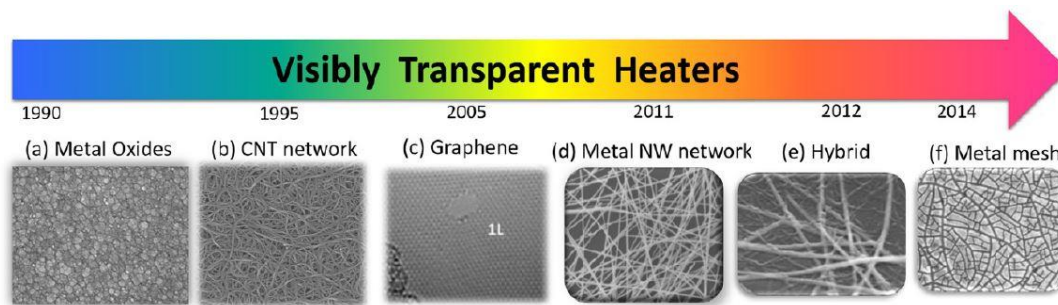


**Figure 1. 2** Classification of TTFH materials in chronological order [20].

#### 1.2.2.1. Metal Oxides

Metal oxides that are used as TCOs have sufficient electrical conductivity and optical transmittance. Electrical conductivity of TCOs can be explained by oxygen vacancy

or interstitial defects in their intrinsic forms or higher valence extrinsic dopants. The dopant concentration and resistivity of TCOs lie around  $10^{20} - 10^{21} \text{ cm}^{-3}$  and  $10^{-4} \text{ }\Omega\cdot\text{cm}$ , respectively [21]. The first TCO was discovered more than 100 years ago when cadmium (Cd) was oxidized thermally to cadmium oxide (CdO) [22]. CdO is an n-type semiconductor with an intrinsic band gap of 2.28 eV. To use CdO as TCO, doping with In (indium), Sn (tin) and F (fluorine) have been practiced which increased its band gap to 3.35 eV [23]. As a result of that, optical transmittances of 85-90% were obtained [24]. However, due to high toxicity of Cd, CdO has never been commercialized for TCO applications.

The most common TCO materials include indium oxide ( $\text{In}_2\text{O}_3$ ), tin oxide ( $\text{SnO}_2$ ) and zinc oxide ( $\text{ZnO}$ ). The intrinsic band gaps of  $\text{In}_2\text{O}_3$ ,  $\text{SnO}_2$  and  $\text{ZnO}$  are 2.9, 3.62 and 3.4 eV, respectively [25] [26]. They are generally utilized with extrinsic dopants to improve their electrical conductivity.  $\text{In}_2\text{O}_3$  is generally doped with Sn and germanium (Ge).  $\text{SnO}_2$  is generally doped with F, antimony (Sb) and tantalum (Ta).  $\text{ZnO}$  is generally doped with gallium (Ga) and aluminum (Al) [21]. In addition to these, ternary compounds between two of these materials can also be utilized as TCOs. The ternary TCO compounds are shown in a simple phase diagram provided in Figure 1.3.

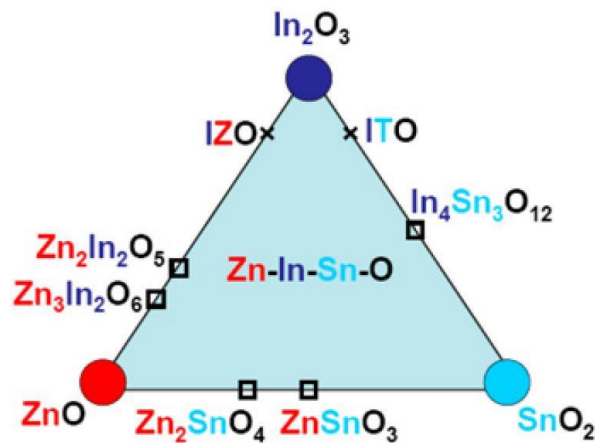


**Figure 1. 3** The ternary TCO compounds between In, Sn, Zn and  $\text{O}_2$  [27].

Among the ternary compounds, intrinsic and extrinsic TCOs, the most widely utilized and commercialized TCO materials are ITO, FTO, AZO and GZO.

### 1.2.2.1.1. Indium Tin Oxide

ITO is  $\text{In}_2\text{O}_3$  rich ternary compound between In, Sn and  $\text{O}_2$  even though there are some reports that it is tin doped indium oxide. It is an n-type semiconductor with low resistivity ( $2 - 4 \times 10^{-4} \Omega\cdot\text{cm}$ ) and wide band gap around 3.5 – 4.3 eV. Moreover, the carrier density of low resistivity ITO is around  $10^{20} - 10^{21} \text{ cm}^{-3}$  and mobility is around  $25 - 32 \text{ cm}^2 / \text{V}\cdot\text{s}$  [28]. ITO can be deposited by several techniques such as magnetron sputtering, chemical vapor deposition (CVD), physical vapor deposition (PVD), spray pyrolysis and sol-gel [29].

The sheet resistance and transmittance of ITO are both dependent on the film thickness. As the ITO thickness increase, both sheet resistance and transmittance decreases. Low sheet resistance is a must for TTFHs in terms of Joule heating but low transmittance is not desired at all. Therefore, the thickness of ITO should be optimized to have low sheet resistance and high transmittance. The effect of ITO thickness on sheet resistance and transmittance are provided in Figures 1.4 (a) and (b), respectively. Decreases in both sheet resistance and optical transmittance are evident in the figures.

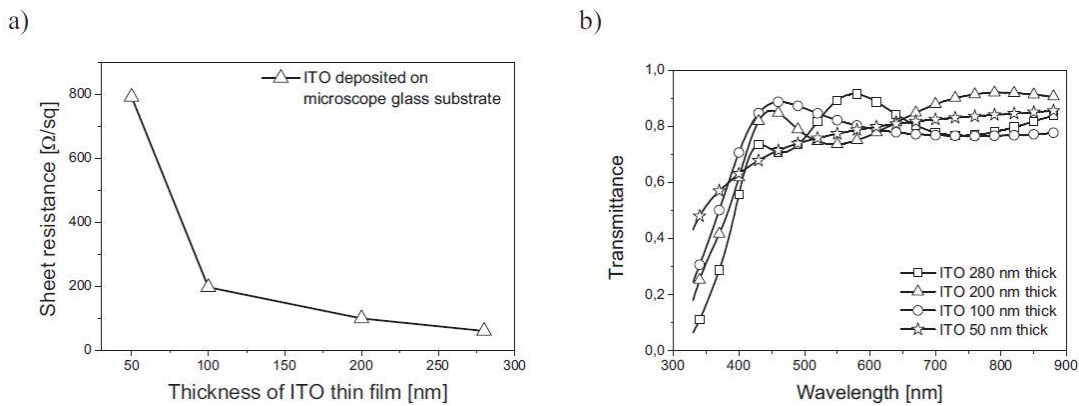


**Figure 1. 4** The effect of ITO thin film thicknesses on (a) sheet resistance and (b) optical transmittance spectra [30].

In literature, solution based ITO deposition was also investigated as an alternative to vacuum deposition. The time dependent thermal response of solution deposited ITO with a TTFH under different applied voltages is provided in Figure 1.5. This TTFH with a transmittance and sheet resistance of 90% and 0.633 k $\Omega$ /sq, respectively, was heated to 163 °C under an applied bias of 20 V. This correspond to power value of 2 W [31]. Although the transmittance value of this TTFH was very promising due to high sheet resistance value of TCO, high applied biases were required to reach a temperature of only 163 °C for this application.

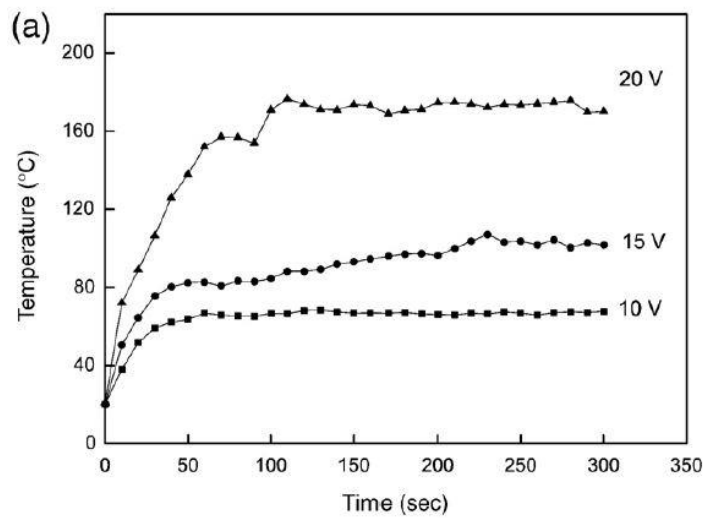


**Figure 1. 5** Time dependent thermal behavior of solution deposited ITO TTFH under 3 different applied biases [31].

In another study, ITO nanoparticle based TTFHs with a transmittance and sheet resistance of 89.5% and 319  $\Omega$ /sq, respectively, are heated to 89 °C at a power density of 0.21 W/cm<sup>2</sup>. For this work, a maximum attained temperature of 150 °C was reported under an applied bias of 35 V [32]. Similar to the previous study [31], thin films with a relatively high sheet resistance was used in this work. Thereby again a high bias was required to attain high temperatures.

ITO TTFHs have sufficient electrical conductivity and optical transmittance. However, ITO has significant drawbacks to be used as TTFHs. High brittleness, high deposition temperatures that are above 300 °C within vacuum and high cost due to In scarcity are some of its drawbacks [33]. Therefore, research to find out alternatives to ITO both as TC and TTFH material become a critical issue over the years.

#### **1.2.2.1.2. Fluorine doped Tin Oxide**

FTO is F doped SnO<sub>2</sub> which forms an n-type semiconductor with a wide band gap of 3.6 eV. Moreover, it has high carrier density, transmittance around 80% and electrical resistivity around 10<sup>-3</sup> Ω.cm [34]. FTO thin films can be deposited with several deposition techniques such as CVD, spray pyrolysis, sol-gel and pulsed-laser deposition [11,36]. It is the most widely utilized TCO following ITO. It has higher thermal stability compared to that of ITO. It was reported that the resistivity of FTO remains stable up to 600 °C; but, resistivity of ITO started to increase severely above 400 °C [36]. Moreover, FTO has better chemical stability than ITO in hydrogen-rich environments [21]. However, FTO has larger surface roughness values compared to ITO which makes FTO thin films unsuitable for touch screens.

There are some reported TTFHs based on FTO. Hudaya et al. utilized FTO thin films with 253 Ω/sq sheet resistance and 85% transmittance. The time dependent thermal behavior of these FTO thin films is provided in Figure 1.6. The 12 V bias was applied to thin films with different carbon concentration (FTO-A, FTO-B and FTO-C). The thin film having 253 Ω/sq (FTO-B) was heated to 39 °C under an applied bias of 12 V. The other ones were heated to around 39 °C at the same applied bias. Long term stability of thin films was also studied and they were found to be stable for at least 2 hours under an applied bias of 12 V [37]. Although transmittance values were appropriate for TTFHs, thin films with high sheet resistance values were used in this work. Therefore, high biases were required to reach high temperatures.

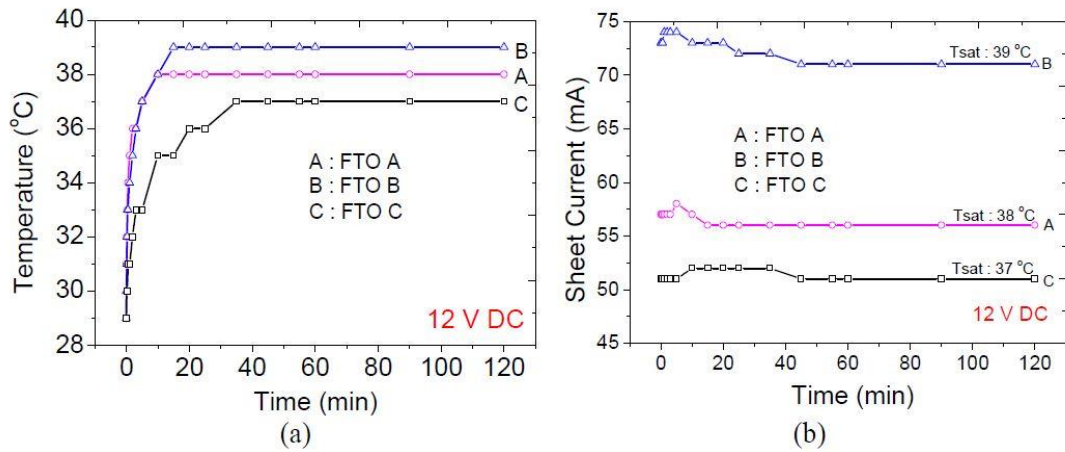


**Figure 1. 6** Time dependent thermal behavior of FTO based TTFH under an applied bias of 12 V for 120 minutes [37].

In another study, FTO based TTFH with an electrical conductivity and transmittance of  $383 \text{ S cm}^{-1}$  and 85%, respectively, was heated to  $90 \text{ }^\circ\text{C}$  under an applied bias of 12 V. To increase the maximum attained temperature, nickel (Ni), chromium (Cr) and nichrome (NiCr) nanorods were scattered onto the thin film. The maximum attained temperatures showed improvements and reached  $116 \text{ }^\circ\text{C}$  in this hybrid structure. To sum up, the sheet resistance of FTO based TTFHs should be decreased to achieve higher temperatures.

### 1.2.2.1.3. Aluminum doped Zinc Oxide / Gallium doped Zinc Oxide

AZO is Al doped and GZO is Ga doped ZnO both of which are n-type semiconductors. The transmittance values of the thin films are superior to both that of ITO and FTO. Transmittances above 90% were reported due to wide band gap of ZnO [38]. Electrical resistivity of thin films lie around  $8 \times 10^{-5} \text{ } \Omega \cdot \text{cm}$ , which is highly appropriate value for TC applications [39] [40]. Advantages of AZO and GZO thin films over ITO and FTO thin films include low cost and non-toxicity [41]. Moreover, they have better thermal stability than ITO. The resistivity of AZO starts to increase only above  $500 \text{ }^\circ\text{C}$  [42].

GZO based TTFHs were reported in literature. A TTFH with an electrical resistivity and transmittance of  $2.14 \times 10^{-4} \Omega \cdot \text{cm}$  and 90%, respectively, was heated to 160 °C under an applied bias of 20 V [43]. The time dependent heating characteristics of this thin film under an applied bias of 12 V and the relation between temperature and applied voltage are provided in Figure 1.7. As it can be deduced from the figure, attained maximum temperature is increased due to Joule heating with an increase in the applied voltage.

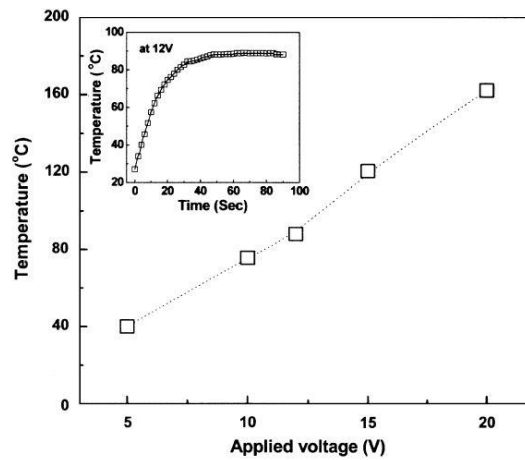


**Figure 1. 7** The time dependent thermal response of GZO based TTFHs under an applied bias of 12 V and the relationship between temperature and applied voltage [43].

AZO based TTFHs were also explored in literature. TTFH with an electrical resistivity of  $1.08 \times 10^{-3} \Omega \cdot \text{cm}$  and transmittance of 90% was heated to 102 °C under an applied bias of 12 V [44]. There are some other AZO based TTFHs but they were used in hybrid structures with other complementing materials [45]. AZO seems to be the best possible candidate for ITO replacement in TCOs due to abundant resources of materials. However, the properties of AZO is not stable under humid environments and its mass production costs are high [46]. Therefore, different materials that can be solution deposited were sought in literature to replace TCOs in TTFHs.

### 1.2.2.2. Carbon Nanotube Networks

Carbon nanotubes are nanostructures that are made up of rolled up graphene layers. They are classified as one dimensional (1D) structures. Initially, SWCNTs in ensemble form called as networks are utilized as TCs. Then, multi-walled carbon nanotube (MWCNT) networks are started to be used as TCs since SWCNTs are expensive [47]. The flexibility of CNT networks is far more superior compared to ITO. Although their optoelectronic performance is comparable to metal oxide based TCs, there are some drawbacks associated with the CNT networks. Firstly, the resistance across the junctions is higher than resistance through a CNT [48]. It means that the CNT network resistance is high even though individual CNTs are perfect conductors. Secondly, the phase purity of CNT networks is poor. There are some carbonaceous impurities in both as synthesized SWCNTs and MWCNTs such as amorphous carbon, nanographites and residual metal catalyst impurities [49].

The sheet resistance and optical transmittance of CNT networks depend on the number of CNTs on the substrate. This can be controlled by the number of layers deposited, where both sheet resistance and transmittance decrease with the number of layers deposited. The change in sheet resistance with respect to optical transmittance with the number of MWCNT layers is provided in Figure 1.8 (a). It is clear that following the deposition of 5 layers, a sheet resistance and transmittance of 756  $\Omega/\text{sq}$  and 90%, respectively, was obtained. In this particular study, TTFH performance of CNT networks was also investigated. A plot showing the change in maximum attained temperatures with respect to applied voltages is provided in Figure 1.8 (b). This heater was heated to 140 °C under an applied bias of 40 V [50].

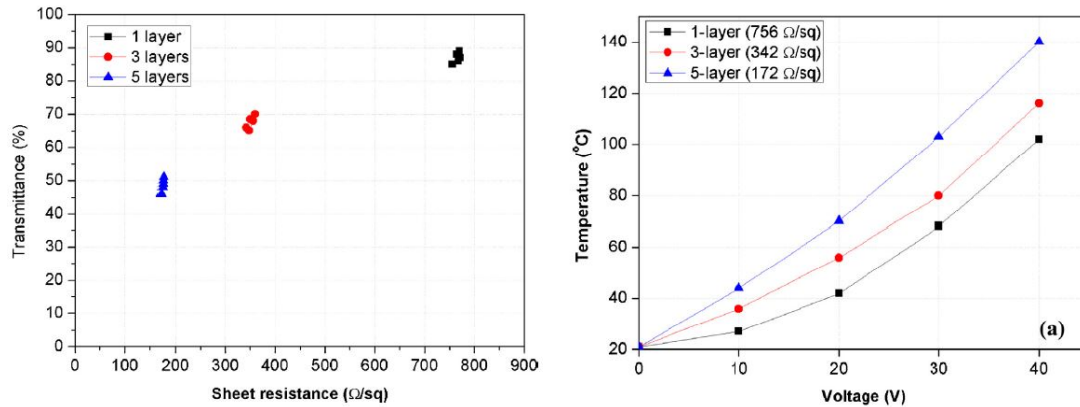


**Figure 1. 8** The relationship between (a) optical transmittance and sheet resistance with respect to number of layers. (b) Attained temperatures with respect to applied voltages for MWCNT based TTFHs [50].

In another study, TTFHs were also fabricated using SWCNT networks. A network with sheet resistance and optical transmittance of 93 Ω/sq and 90%, respectively, was heated to 140 °C under and applied bias of 7 V [11]. Although, electrical and thermal performances were improved in recent years, CNT network based TTFHs still need further developments particularly in terms of electrical conductivity.

### 1.2.2.3. Graphene

Graphene is a 2 dimensional (2D) structure that consists of a hexagonal lattice formed of single layer carbon (C) atoms. It has high thermal conductivity around 5000 W/m.K and high flexibility along with high electrical conductivity and optical transparency [51]. The high thermal conductivity of graphene provide homogeneous temperature distributions over the substrate and shorter thermal response times, which are highly critical parameters for TTFHs. Monolayer of graphene has excellent optical transmittance around 97% but very poor sheet resistance around 10 kΩ/sq [52]. The sheet resistance and transmittance decreases with increasing the number of layers. To use graphene in TTFHs, 3 to 5 layers are necessary. The transmittance and sheet resistance of these thin films lie around 80% and 100 Ω/sq, respectively [53]. The sheet resistance values of graphene are not extremely low due

to high contact resistance, defects and grain boundaries. However, new advancements in CVD based growth methods allowed the synthesis of defect free graphene [54]. The thin films that were fabricated with this method had a transmittance and sheet resistance of 90% and  $30 \Omega/s$ , respectively, for 4 layers of graphene. Moreover, doping can be performed to decrease the sheet resistance of the graphene. For instance, the sheet resistance of 3 layers of graphene was decreased from 403 to  $66 \Omega/sq$  through doping with gold chloride ( $AuCl_3$ ). This thin film had a transmittance of 90% [12]. This  $AuCl_3$  doped graphene thin film was also used as a TTFH in a defogger. This thin film was heated to  $110^\circ C$  under an applied bias of 12 V, corresponding to a power value of 0.14 W.

In another study, doping was performed on 4 layers of graphene synthesized by roll to roll CVD method. Doping was practiced by  $AuCl_3$  and nitric acid ( $HNO_3$ ). Thin films with a transmittance as low as 89% and sheet resistance of  $43 \Omega/sq$  were obtained. Time dependent thermal response of these doped thin films in comparison to ITO reference under an applied bias of 12 V is provided in Figure 1.9. The  $AuCl_3$  doped graphene was heated to  $100^\circ C$  under an applied bias of 12 V [51].

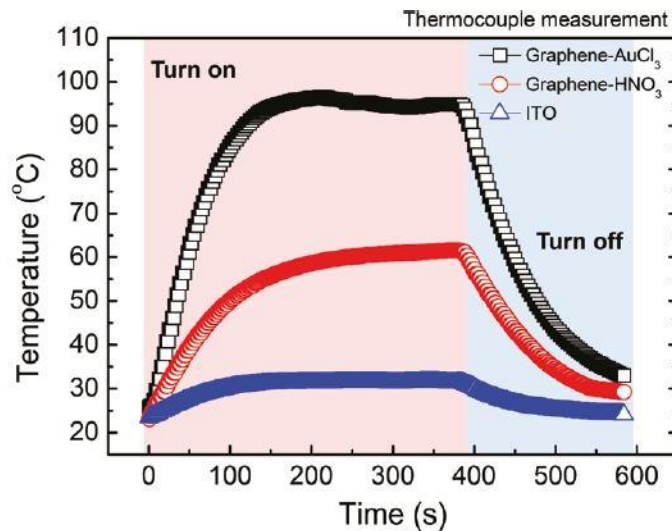


**Figure 1. 9** The time dependent thermal response of  $AuCl_3$  and  $HNO_3$  doped 4 layers of graphene and ITO under an applied bias of 12 V [51].

The optical transmittance of multilayered graphene thin films is suitable for TTFH applications. However, high sheet resistance of these films necessitates higher applied biases. Among all TCs, metal nanowire random networks with low sheet resistances without sacrificing optical transmittance are highly promising for TTFH applications.

#### **1.2.2.4. Metal Nanowire Random Networks**

The conductivity of metals, especially silver (Ag), copper (Cu) and gold (Au) are higher than that of ITO. However, their continuous thin films are not very much transparent. Instead, metal nanowire random network are demonstrated in literature. Metal nanowire random networks are formed by overlapping metal nanowires that generate junctions. Cost effective, solution based processes were used for the synthesis of metal NWs [55]. Bulk Ag has the highest electrical conductivity among metals so silver nanowires (Ag NWs) are extensively investigated in literature as TCs. Cu and Au have good electrical conductivities so for similar reasons copper nanowires (Cu NWs) and gold nanowires (Au NWs) followed Ag NWs in literature.

Once the NWs are synthesized, metal NW random networks can be fabricated using various solution based methods such as drop casting, vacuum filtration, spin coating, spray coating and Meyer rod coating. Drop casting is practiced simply by dropping NW solution onto a substrate, which was followed by drying of the solvent. However, uniform NW networks cannot be deposited by this method due to drying marks that occur around the droplets [56]. Vacuum filtration includes formation of NW networks on a filter membrane, which were then transferred to a target substrate. However, transferring NW networks to a substrate is not an efficient and scalable method [57]. Spin coating includes dropping NW solution to a substrate and obtaining a uniform NW network with the help of centrifugal force. However, this method necessitates the use of excessive amount of NW solution and thus is not scalable [58]. Spray deposition includes spraying NW solution to a substrate with the help of an airbrush. Substrates are preferentially placed onto a hot plate during

deposition for the instant evaporation of the solvent. This method is cost effective, easy and very scalable. Moreover, it has a rich parameter space to adjust the optoelectronic properties of NW random networks [59]. Meyer rod coating method simply works by rolling a stainless steel rod over the substrate which eliminates the excess NW solution. This method is simple and scalable, provided that substrate size rods can be found. However, due to the homogeneity, scalability and cost effectiveness, spray coating is the most widely utilized fabrication method for the formation of NW networks [60]. A table comparing aforementioned deposition methods for NW networks is provided in Table 1.1.

**Table 1. 1** The comparison of five common production methods for metal NW networks. The number of plus signs indicate the suitability of the process.[60]

<b>Method</b>	<b>Homogeneity</b>	<b>Scalability</b>	<b>Cost</b>
Spin Coating	+	+	+++
Spray Coating	+++	+++	++
Vacuum Filtration	+++	+	+
Drop Casting	+	+	+
Meyer Rod	++	+++	++

The electrical conductivity and optical transparency of the metal NW random networks are among the highest for TCs. For instance, at a transmittance of 95% sheet resistances of 20  $\Omega$ /sq and 100  $\Omega$ /sq were achieved for Ag NWs [61] and Cu NWs [62], respectively. The electrical conductivity of metal NW networks is governed by the percolation theory. According to this theory, to have an electrical conduction between two points, a continuous path among NWs must be formed. At a critical nanowire density ( $N_C$ , percolation threshold), this path is formed and further increase in the NW density results in a decrease in sheet resistance of the networks [63]. Moreover, percolation threshold strongly depends on the ratio between NW lengths and diameters ( $L/D$ ) since this ratio is directly related to the number of pathways in the network. Provided that the  $L/D$  ratio is high,  $N_C$  becomes lower. In

addition, sheet resistance and optical transmittance do depend on each other and both must be optimized to use metal NW networks in TTFHs [64]. The relationship between sheet resistance and NW density, which is given as the area fraction of NWs in this study and the relation between sheet resistance and transmittance for different L/D ratios of Ag NW network are provided in Figures 1. 10 (a) and (b), respectively. The percolation threshold, which is expressed by a critical area fraction in this study decreases with increasing the L/D ratio. Moreover, sheet resistance shows a decreasing behavior with increasing L/D ratio under the same transmittance [64].

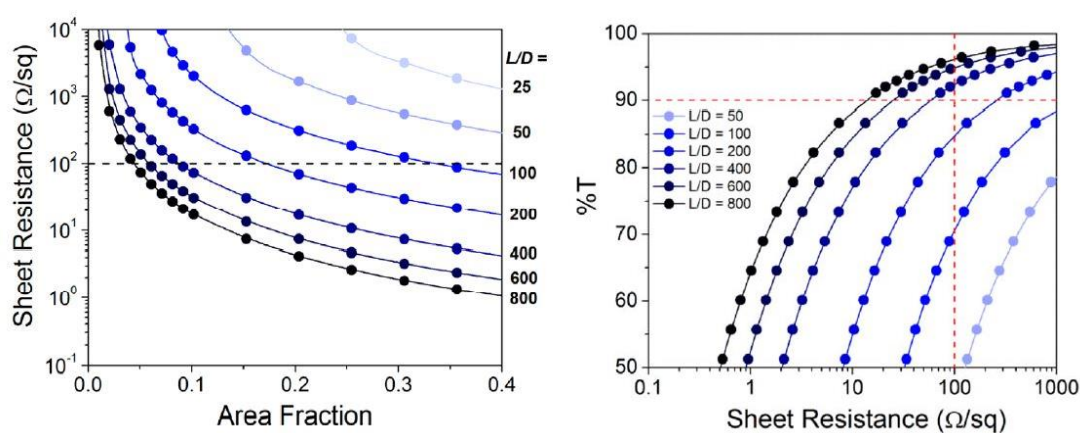
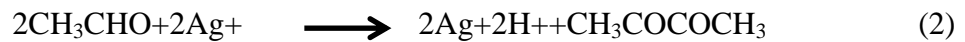


**Figure 1. 10** Graphs showing the relationship between (a) sheet resistance and area fraction, (b) transmittance and sheet resistance for different L/D ratios [64].

Metal NW random networks also have excellent flexibility along with promising optoelectronic performance. One of the main uses of Ag NW networks is in TTFHs. Cu NW TTFHs are relatively novel compared to Ag NW TTFHs and only a few reports can be found in the literature [65].

#### 1.2.2.4.1. Silver Nanowire Random Networks

Ag NWs are generally synthesized by solution based polyol method. All solution based NW syntheses make use of a metal source, a reducing agent and a capping agent to ensure directional growth and sometimes a solvent for dissolution of all the chemicals. In polyol synthesis, three chemicals were used in general, which are silver nitrate ( $\text{AgNO}_3$ ) as the metal source, polyvinylpyrrolidone (PVP) as the capping agent and ethylene glycol (EG) as both the reducing agent and solvent. The reaction takes place above  $150\text{ }^\circ\text{C}$  since EG is transformed into glycolaldehyde at those temperatures [66]. Glycolaldehyde reduces Ag ions to Ag [67]. Therefore, 2 important reactions that govern Ag NW synthesis during polyol method are [68];



Generally, seeds that have decahedron structure were formed and build up in nanowire form. Polyol synthesized Ag NWs have face centered cubic structure (FCC) and a penta-twinned special geometry. The penta twinned structure have five  $\{100\}$  planes at the sides and five  $\{111\}$  planes at the tips. This results in a pentagonal cross section and a growth direction of  $\langle 110 \rangle$  [69].

Ag NWs with an average length around  $10\text{ }\mu\text{m}$ , diameter around  $40\text{ nm}$  and L/D around 100 are synthesized using polyol synthesis [70]. These dimensions are highly suitable for the fabrication of high performance TCs. However, contact resistance between the NWs in as deposited networks can be high due to silver oxide formation around the NWs and the residual polymer layers. There are several ways to decrease the contact resistance. Firstly, contact resistance can be decreased by annealing the Ag NW networks at temperatures that are high enough to burn the surfactant or residual polymer layers. This eliminates the spaces between overlapping Ag NWs and fuse Ag NWs together at contact points. Therefore, dramatic decreases in sheet

resistance of the networks can be observed. For example, Lee et al. reported a decrease in sheet resistance from 1 k $\Omega$ /sq to 100  $\Omega$ /sq upon annealing at 200 °C for 20 minutes [71]. It should also be mentioned that following the achievement of optimum sheet resistance, further annealing must be avoided. This is because the sheet resistance of the networks increase back again with further annealing. This is due to fragmentation and spherodization of NWs which is called as Rayleigh instability [72]. This problem is equally important for TTFHs and the details of this phenomenon will be discussed in the following sections. Secondly, mechanical pressing can be performed on Ag NW networks following deposition to reduce the contact resistance. This method decreases the overall sheet resistance of the networks as well as their roughness. For example, the sheet resistance of Ag NW networks was found to decrease from 100  $\Omega$ /sq to 10  $\Omega$ /sq simply by mechanical pressing [73].

Ag NW based TTFHs were extensively explored over the years due to possession of excellent electrical conductivity combined with optical transparency. Ag NW networks with a sheet resistance and transmittance of 6.5  $\Omega$ /sq and 91%, respectively, were reported in literature. Moreover, Ag NW networks have good thermal conductivity reported due to high thermal conductivity of bulk Ag, which is also an important parameter for TTFHs to have a homogeneous temperature distribution. In a Ag NW based TTFH study, networks with sheet resistances of 4.3, 25 and 30  $\Omega$ /sq at corresponding transmittance values of 86.3, 88.3 and 89.6%, respectively, were used and heated under applied biases. The time dependent thermal response of these networks under various biases are provided in Figure 1.11. Reasonably high temperatures were attained at low applied biases (200 °C under 4 V) due to excellent electrical conductivity (4.3  $\Omega$ /sq). Moreover, Ag NW based TTFHs were found to have long term stability and handle repetitive heating cooling cycles. In addition, highly uniform temperature distribution was obtained using an IR camera from these materials with parallel contacts. Ag NW based TTFH was endured heating at 126 °C for 22 hours and survived at least 5 repetitive heating and cooling cycles. Maximum attained temperature was 275 °C for this study and degradation mechanism of Ag NWs (Rayleigh Instability) was also discussed [74].

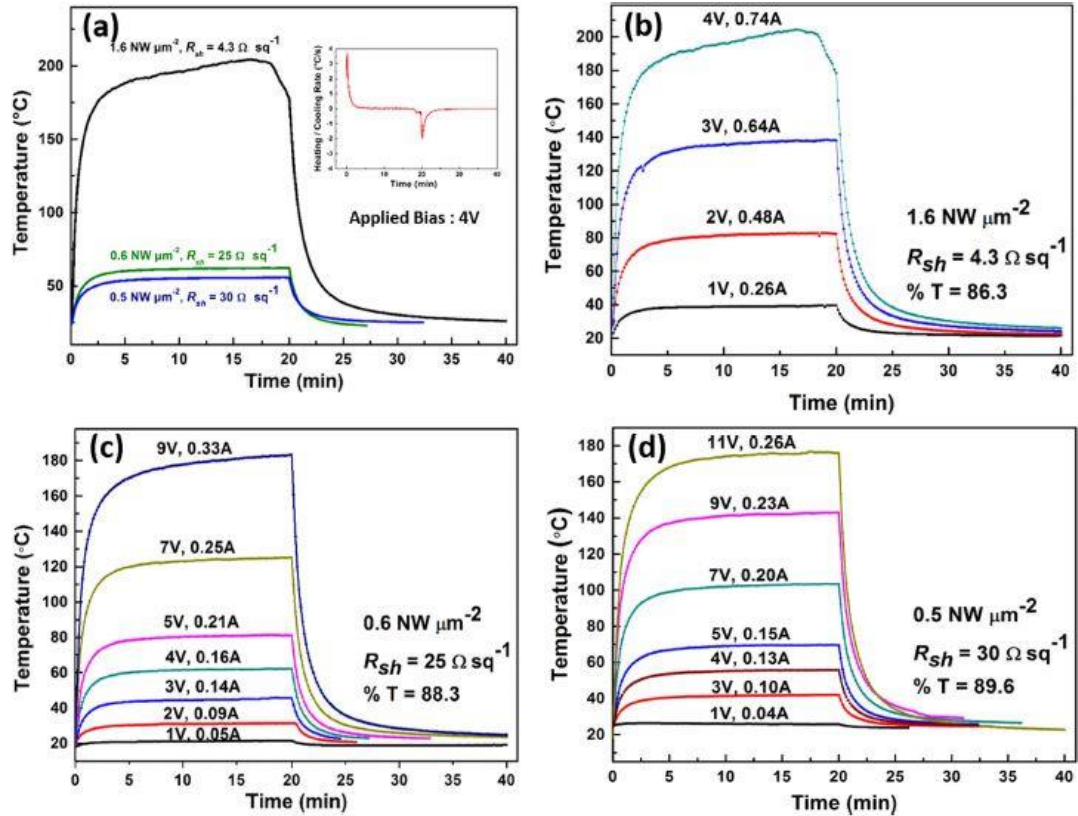


**Figure 1.11** Thermal response of (a) thin films with 3 different sheet resistances under an applied bias of 4 V. Thermal response of Ag NW networks with sheet resistances of (b) 4.3, (c) 25 and (d) 30  $\Omega/\text{sq}$  [74].

There are some Ag NW based TTFHs that are used in hybrid form combined with other materials to prevent the drawbacks associated with bare Ag NW networks. These TTFHs will be discussed in the following sections.

#### 1.2.2.4.2. Copper Nanowire Random Networks

In the last few years, the use of Cu NW random networks as an alternative to Ag NWs were also demonstrated as TCs. Cu is almost equally conductive and much cheaper than Ag in bulk form. Moreover, its thermal conductivity is also similar to that of Ag, which is an important parameter for TTFHs. Therefore, various synthesis

methods were explored for Cu NWs. Synthesis methods of Cu NWs can be divided into two groups, namely ethylenediamine (EDA, C<sub>2</sub>H<sub>8</sub>N<sub>2</sub>) and alkylamine assisted syntheses. Initially, EDA assisted synthesis was utilized for the synthesis. In this method, hydrazine (N<sub>2</sub>H<sub>4</sub>) was used as the reducing agent, which reduces Cu<sup>2+</sup> ions to Cu and EDA was used as the capping agent in basic conditions with the help of sodium hydroxide (NaOH) at low temperatures (around 25 - 100 °C) [75]. The reduction reaction is provided below;



Cu NWs with average lengths around 40 μm, diameters around 100 nm and L/D ratio around 400 were synthesized with the EDA assisted method. However, the use of N<sub>2</sub>H<sub>4</sub> is highly dangerous due to its toxicity. Therefore, Cu NW synthesis methods were evolved to replace N<sub>2</sub>H<sub>4</sub> with more environmentally friendly reducing agents.

In alkylamine assisted synthesis, relatively higher temperatures are used in neutral conditions. There are several methods to replace N<sub>2</sub>H<sub>4</sub> in literature. For instance, octadecylamine (ODA, C<sub>18</sub>H<sub>37</sub>N) was used as both the reducing and capping agent at a reaction temperature of 120-180 °C [76]. Oleylamine (OLA, C<sub>18</sub>H<sub>37</sub>N) was used with nickel (II) acetylacetonate (Ni(acac)<sub>2</sub>) as a catalyst for the reduction reaction at 175 °C [77]. Finally, glucose and hexadecylamine (HDA) were used as reducing and capping agents, respectively, at a reaction temperature of 100 °C [78]. The major advantage of last synthesis is the lower reaction temperature due to glucose. Average diameters of 25 nm and lengths of 50 μm were obtained with the synthesis method that utilizes glucose and hexadecylamine (HDA). The reduction reaction of alkylamine assisted synthesis is more complex than EDA assisted counterpart. The illustration of oxidation reaction of glucose is provided in Figure 1.12. RNH<sub>2</sub> is HDA for this illustration and R is [-(CH<sub>2</sub>)<sub>15</sub>CH<sub>3</sub>] for HDA. According to this study, at temperatures above 100 °C, Maillard reaction takes place between glucose and HDA, which then leads to the formation of glucoseamine. This glucoseamine is converted to amadori products and then subsequently to Maillard reaction products. These

Maillard reaction products react with amine and then forms melanoid. Maillard reaction products and melanoids are responsible for the reduction of  $\text{Cu}^{2+}$  ions to Cu. According to this study, HDA act as both the capping agent and assistant to reduction reaction of Cu [79].

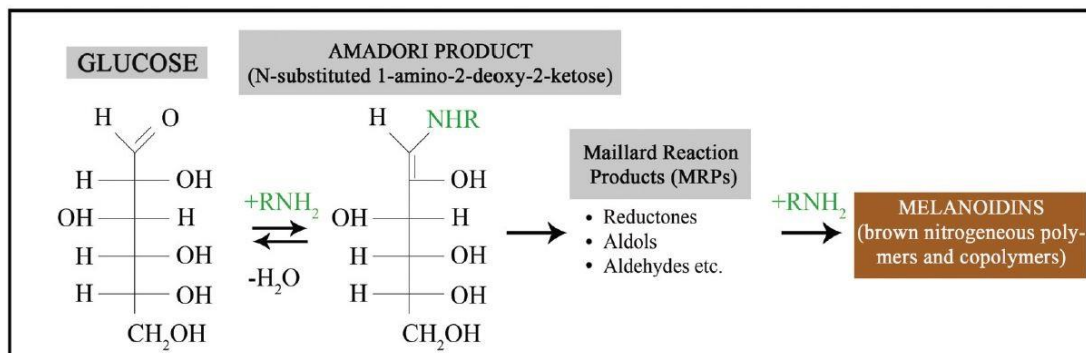


**Figure 1. 12** The general oxidation reaction of glucose with the help of HDA [79].

The Cu NWs synthesized with glucose and HDA has penta-twinned structure, just like polyol synthesized Ag NWs. Cu also has FCC structure and decahedral seeds are initially formed in the synthesis. These seeds are build up to form penta-twinned NW structure, which has five  $\{100\}$  planes at the sides and five  $\{111\}$  planes at the tips and grows in  $\langle 110 \rangle$  direction [80].

The major disadvantage of Cu NWs compared to Ag NWs is the ease of oxidation of Cu NWs upon reacting with air even at room temperature. Three compounds can be formed by the oxidation of Cu NWs namely, cuprous oxide ( $\text{Cu}_2\text{O}$ ), copper hydroxide ( $\text{Cu}(\text{OH})_2$ ) and cupric oxide ( $\text{CuO}$ ). The first oxide formed by oxidation is generally  $\text{Cu}_2\text{O}$ .  $\text{Cu}_2\text{O}$  forms very rapidly at a thickness of 2.8 nm and then reaction slows down. Then metastable  $\text{Cu}(\text{OH})_2$  is formed and eventually turns into  $\text{CuO}$  [81]. The formation reactions of these oxides are provided below;



The oxidation of Cu NWs takes place upon reacting with air. Some studies reported that Cu NWs start to get oxidized even in the synthesis step upon reacting with water [82]. In the network form, the surface oxides increase the sheet resistance of the networks. Moreover, as discussed for Ag NWs, the residual polymer layers or surfactants increase the contact resistance between Cu NWs. Similarly, mechanical pressing or thermal annealing can be used to decrease the sheet resistance of the Cu NW networks. In addition, weak acid treatments are demonstrated to get rid of the surface oxide so to decrease the sheet resistance [82] [83]. In literature, glacial acetic acid (GAA) and lactic acid treatments are used for this purpose. In GAA treatment, GAA is mixed with Cu NW solution prior to the fabrication of electrodes and then removed with isopropanol. The Cu NW networks with an optical transmittance of 94% showed sheet resistances of  $10^6$  and  $15 \Omega/\text{sq}$  before and after the GAA treatment, respectively [83]. In lactic acid treatment, lactic acid was mixed with Cu NWs and then removed by ethanol before network fabrication. Networks with a sheet resistance and optical transmittance of  $19.8 \Omega/\text{sq}$  at 88.7%, respectively, was obtained by this method [82]. However, the use of weak acids for the removal of organic residues and surface oxides is only a temporary solution since Cu NWs will be oxidized again upon reacting with air. Therefore, protection layers should be utilized to increase the stability of Cu NWs.

#### 1.2.2.4.2.1. Protection Layers of Copper Nanowires

A protection layer is necessary for the long-term use of Cu NW networks. There are some attempts to increase the stability of Cu NWs. Since Cu NW networks are usually utilized as TCs, the effects of a protection layer on the total transmittance are

investigated in parallel to the oxidation stability. In a study by Rathmell et al., Ni was used as a protection layer on Cu NWs. This was simply practiced by the reduction of Ni onto Cu NWs in solution. Cupronickel NWs with a core / shell structure were obtained in this process. Then, transparent networks were prepared with these cupronickel NWs using Meyer rod coating. To compare the transmittance and oxidation resistance, networks with the same sheet resistance ( $60 \text{ } \Omega/\text{sq}$ ) were prepared with Cu and cupronickel NWs. It was stated that the cupronickel NW networks are 1000 times more resistant to oxidation; but, a 10% sacrifice in transmittance (from 94.4% to 84.3%) was observed [84].

Noble metals that are resistant to oxidation such as Ag, Au and Pt were also used as the protection layer. They were prepared by reducing noble metal ions onto Cu NWs in solution state. Stewart et al. used ascorbic acid to remove the native oxide layer on Cu NWs and to help reducing noble metal ions without galvanic replacement. Core shell structure of Cu - Ag, Cu - Au and Cu - Pt were observed. The networks were fabricated by Meyer rod coating following the deposition of a protection layer. The oxidation resistance tests of these networks were carried out at  $160 \text{ } ^\circ\text{C}$  in open atmosphere. The sheet resistance of bare Cu NW networks was increased from 39 to  $80 \text{ } \Omega/\text{sq}$  in 30 minutes. On the other hand, the sheet resistance of 15 nm Ag coated Cu NW networks were only increased slightly from 26 to  $49 \text{ } \Omega/\text{sq}$  in 24 hours. The oxidation resistance of Cu NWs with noble metal coating is certainly much better than that of bare Cu NWs. Moreover, at the same sheet resistance ( $45 \text{ } \Omega/\text{sq}$ ), 15 nm Ag coated Cu NW thin films showed a transmittance loss of 5%. The transmittance loss was worse for Cu - Au and Cu - Pt core shell structure networks [85].

Graphene and graphene oxide were also utilized as protection layers on Cu NWs. Graphene was deposited onto Cu NW networks that were prepared by vacuum filtration method. A transmittance loss of 2.4% (from 78.1% to 75.7%) and a sheet resistance increase (from  $11 \text{ } \Omega/\text{sq}$  to  $14 \text{ } \Omega/\text{sq}$ ) were observed upon deposition of single layer graphene. The oxidation resistance tests were carried out at  $60 \text{ } ^\circ\text{C}$  in terms of  $R/R_0$ , where R was the instantaneous resistance and  $R_0$  was the initial

resistance. It was reported that  $R/R_0$  increased to 2 after 4 days for bare Cu NW networks. On the other hand,  $R/R_0$  was increased only to 1.48 for graphene coated Cu NW networks after 35 days. Graphene coating certainly provided oxidation resistance to Cu NWs [86]. In another study, graphene oxide (GO) nanosheets were wrapped onto Cu NWs in solution through ultrasonication using core / shell GO / Cu NWs. The networks were then prepared via vacuum filtration. Then, thermal annealing was performed to reduce the GO. The networks with a sheet resistance and a transmittance of 28  $\Omega$ /sq and 90%, respectively, were prepared by this method. The oxidation resistance was monitored at 80 °C. While the sheet resistance of bare Cu NW networks was increased in a few hours, that of reduced GO / Cu NW networks was only increased from 40 to 80  $\Omega$ /sq in 2 days [87].

Common TCO materials such as  $\text{In}_2\text{O}_3$ ,  $\text{SnO}_2$  and  $\text{ZnO}$  were also utilized as a protection layer onto Cu NWs due to their excellent optical transmittance. Cu NW networks were prepared by Meyer rod coating. Then, In, Sn or Zn was electroplated onto these networks. Oxidation of these metals was performed using hydrogen peroxide ( $\text{H}_2\text{O}_2$ ). At the end, core / shell  $\text{In}_2\text{O}_3$  / Cu NW,  $\text{SnO}_2$  / Cu NW and  $\text{ZnO}$  / Cu NW networks were obtained. The thicknesses of the oxides were recorded as 3-5 nm. Sheet resistance of the networks remained the same through the processes and only 1% transmittance loss (from 85% to 84.3%) was recorded. The oxidation resistance of the networks was monitored at 160 °C. The sheet resistance of bare Cu NW networks was increased very fast and they became insulating after 12 hours. On the other hand, only 15% sheet resistance increase was recorded for  $\text{ZnO}$  / Cu NW networks after 18 hours. To sum up, core / shell structure achieved with TCOs in network form showed a small transmittance loss with improved oxidation stability even at 160 °C [88].

Hsu et al. reported the use of AZO and  $\text{Al}_2\text{O}_3$  as protection layers for copper nanofibers (Cu NFs). Electrospun nanostructures with average diameters of 100 nm were termed as NFs. 25 nm AZO and 1 nm  $\text{Al}_2\text{O}_3$  were deposited onto Cu NFs using

atomic layer deposition (ALD) method [89]. ALD is a special deposition technique that is classified as a subgroup of CVD. There are 2 chemical precursors in ALD and thin film is formed by sequential introduction of precursors onto a substrate. In every pulse, half reaction takes place on the substrate surface and with 2nd precursors pulse, the reaction is completed. In between every pulse, byproducts are carried away with an inert gas such as argon (Ar) or nitrogen (N<sub>2</sub>). The pulse times are around 10 milliseconds and at each reaction cycle 1 layer is deposited onto the substrate. The thickness of the thin films is adjusted by the number of cycles. Schematic illustration of ALD process is provided in Figure 1.13.

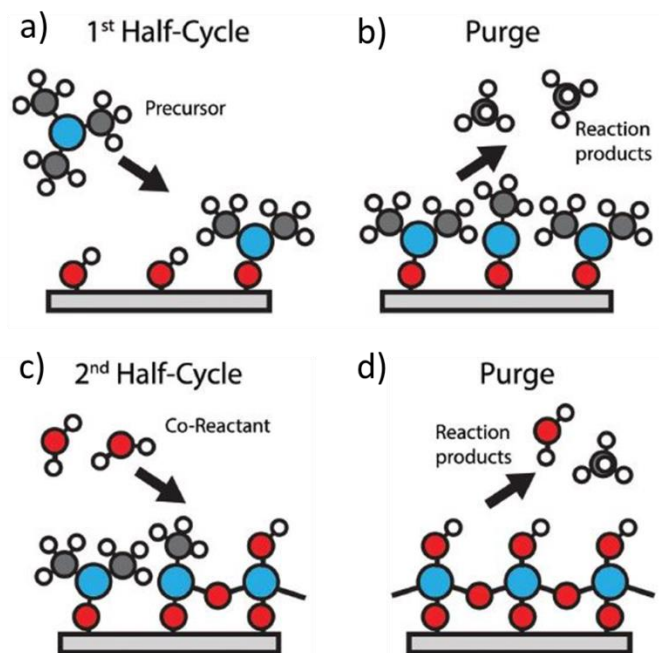


**Figure 1. 13** Schematic illustration of ALD process cycle, which consists of (a) first half reaction, (b) purging of by-products, (c) second half reaction and (d) purging of by-products [90].

The ALD process takes place under vacuum at temperatures below 350 °C. There are a lot of advantages of ALD over common deposition techniques such as CVD and PVD. These include conformal deposition on high aspect ratio and 3 dimensional (3D) structures, uniform thin film growth, good compositional control for doped metal oxides and precise thickness control even at angstrom levels. The slow

deposition rate around 100-300 nm/h is the main drawback of ALD; but, uniformity of the grown thin films is strongly related with that [91]. Therefore, protection layers that are deposited using ALD are ideal for metallic NW networks. For AZO / Al<sub>2</sub>O<sub>3</sub> deposited Cu NFs, the sheet resistance (47 Ω/sq) remained the same after the deposition and transmittance loss was reported as 1%. The oxidation resistance was monitored at 160 °C. The sheet resistance of bare Cu NF networks was found to increase rapidly to 10 M Ω/sq after 20 minutes. On the other hand, the sheet resistance of AZO / Al<sub>2</sub>O<sub>3</sub> deposited Cu NF networks was found to increase by only 10% after 8 hours [89]. The thickness of ALD deposited layers can be increased to further improve the temperature stability in sacrifice of network transmittance. Schematic illustration of the oxidation behavior of bare Cu NFs and AZO / Al<sub>2</sub>O<sub>3</sub> deposited Cu NFs are provided in Figure 1.14.

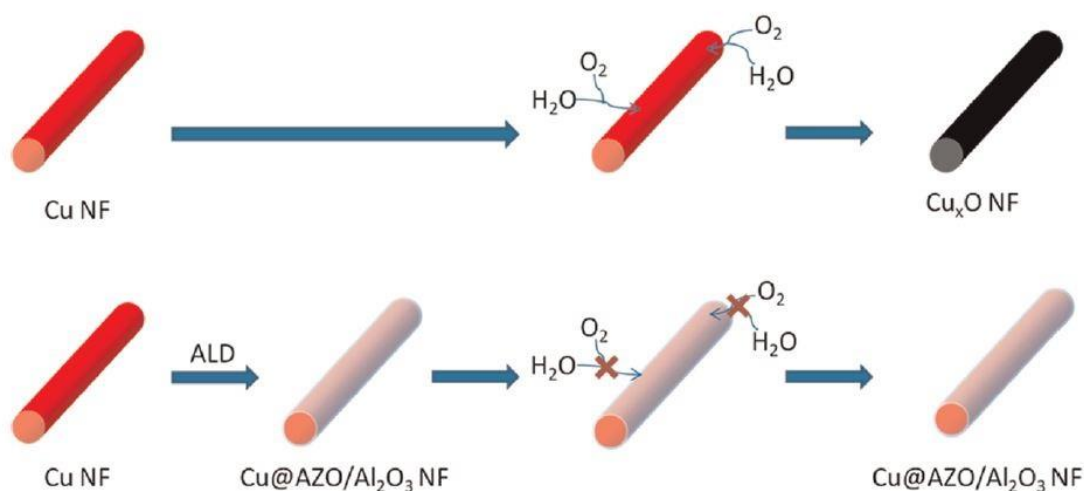


**Figure 1. 14** Schematics showing oxidation behavior of bare Cu NFs and AZO / Al<sub>2</sub>O<sub>3</sub> deposited Cu NFs [89].

There are no reports on the use of bare Cu NW networks as TTFHs in literature due to ease of oxidation of Cu at elevated temperatures. There are only a few reports on the use of a protection layer to improve the TTFH performance of Cu NWs and these are classified as hybrid heaters and will be discussed in the following sections.

#### **1.2.2.4.3. Failure Mechanism of Metallic Nanowire Random Networks at Elevated Temperatures**

Current passes through metallic NW networks and the temperature of NWs increase due to Joule heating upon application of bias. Ag and Cu have high melting points of 961.8 °C and 1085 °C, respectively. However, metallic NW random network based TTFHs fail at temperatures much below than their melting points due to Rayleigh instability [72]. Rayleigh instability states that as the temperature increases, NWs start to melt at the junction points. As a result of that metal accumulates at the junction points due to surface diffusion and metal NWs get thinner and even break away at some points. Therefore, sheet resistance increases due to a decrease in the number of current carrying pathways. At the end, NWs break off as spherical fragments and consecutively networks become insulating due to loss of pathways for electron transport [74]. It is reported that NW density is strongly related with the temperature in which Rayleigh instability occurs [92]. Lower NW density networks fail more quickly compared to higher NW density networks. Since there are lower number of NWs and pathways at lower NW density networks, the current density in junctions and individual NWs are higher.

Thermal annealing of metallic NW networks is performed to decrease their sheet resistance. Rayleigh instability is also observed in thermal annealing. The sheet resistance decreases with increasing annealing temperature until a critical temperature is reached. After that point, melting and accumulation at junctions and then thinning and fragmentation of NWs are observed. Rayleigh instability is strongly related with the NW diameter. It is reported that, the temperature in which Rayleigh instability occurs increase with NW diameter. However, it should be noted that NW diameter is also related with the optical transmittance of the network. It is reported that, Rayleigh instability occurs at around 300°C for both Ag and Cu NWs [72] [93]. Moreover, passivation layer around metallic NWs can increase the temperature in which Rayleigh instability occurs compared to bare metallic NW networks. SEM micrographs of Ag NW networks annealed for 30 minutes at

different temperatures are provided in Figures 1.15 (a) - (f). The Rayleigh instability occurred around 300 °C and fragmentation was found to increase with annealing temperature.

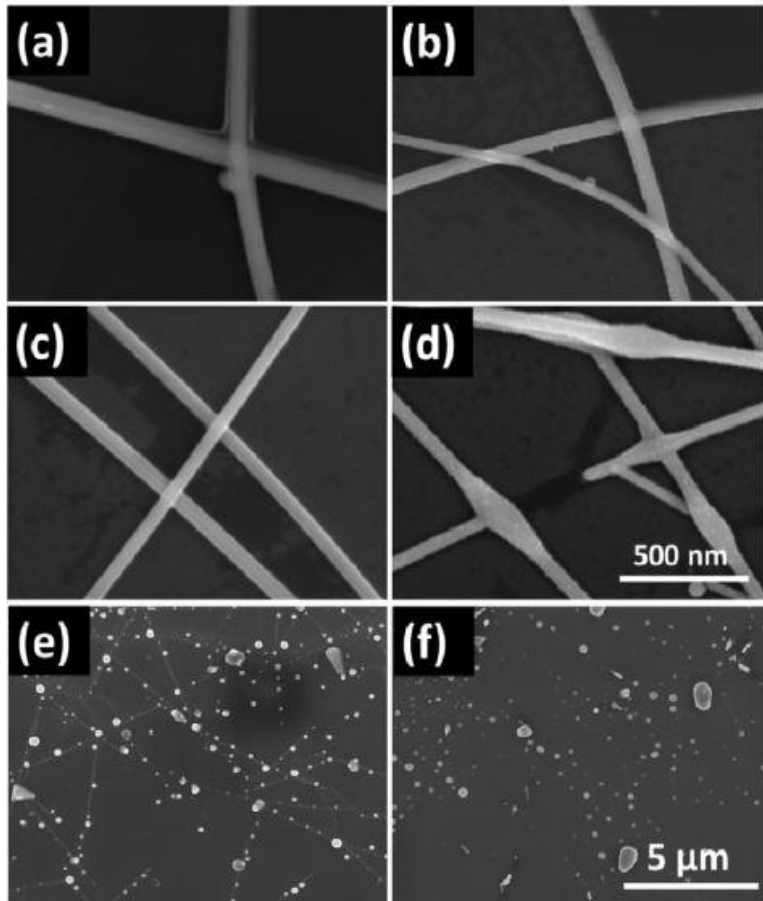


**Figure 1. 15** SEM micrographs of Ag NW networks (a) that are as deposited, annealed at (b) 100, (c) 200, (d) 300, (e) 400 and (f) 500 °C [7].

#### 1.2.2.5. Hybrid Materials

Metal oxides, CNT networks and graphene are used in TTFHs due to their good environmental stability and homogeneous temperature distribution. However, their sheet resistance is still considered high at high transmittance values. Thus, high operating voltages are needed to attain high temperatures. In contrast, metallic NW

networks have low sheet resistances at high transmittances. However, their environmental stability is not as good as CNT networks and graphene. Ag NWs are prone to sulfidization [94], where Cu NWs are prone to oxidation [84] at atmospheric conditions. To overcome the disadvantages of all TTFH materials, hybrid materials are started to be used as TTFHs. There are two ways to fabricate hybrid TTFHs, combining metal oxides, CNT networks, graphene and insulating polymers with metal NW networks either by depositing protective layers onto NW networks or by embedding NW networks in them. Examples of some of the hybrid TTFHs with their performances are provided in Table 1.2.

**Table 1. 2** Properties of hybrid TTFHs (PEDOT:PSS: poly(3,4-ethylenedioxythiophene) polystyrene sulfonate, HRP: Heat Resistant Polymer, PVA: poly(vinyl alcohol), PMMA: poly(methyl methacrylate)).

Material	Sheet Resistance ( $\Omega/\text{sq}$ )	Transmittance at 550 nm (%)	Attained Maximum Temperature ( $^{\circ}\text{C}$ )	Applied Voltage at Maximum Temperature (V)	Reference
Ag NW – Graphene Sheets	27	80	230	15	[95]
Ag NW- PEDOT:PSS	4	70	120	6	[96]
Ag NW – HRP	10	79	230	13	[13]
Ag NW – PVA Film	6	81	100	3	[97]
Cu NW - PMMA	6.1	77	150	8	[98]
Cu NW – $\text{Al}_2\text{O}_3$	Resistance: 19 $\Omega$	Not specified	200	7	[99]

In Cu NW – PMMA study, Cu NWs were synthesized via solution based method and deposited onto glass and polyethylene terephthalate (PET) substrates by spray coating. Various networks that have different NW densities were prepared. Then, hydrophobic polymers such as PMMA, polyacrylate (PA) and polydimethylsiloxane (PDMS) were deposited onto Cu NW networks via spin coating. It is reported that, under the same applied bias, higher NW density networks reached to higher temperatures compared to lower NW density networks. The PMMA protected Cu NW network with a sheet resistance and transmittance of  $6.1 \Omega/\text{sq}$  and 77%, respectively, was heated to  $150 \text{ }^\circ\text{C}$  under an applied bias of 8 V. A heating rate of  $14 \text{ }^\circ\text{C/s}$  was reported [98]. Thermal response of networks with 2 different NW densities under various applied voltages are provided in Figures 1.16 (a) and (b).

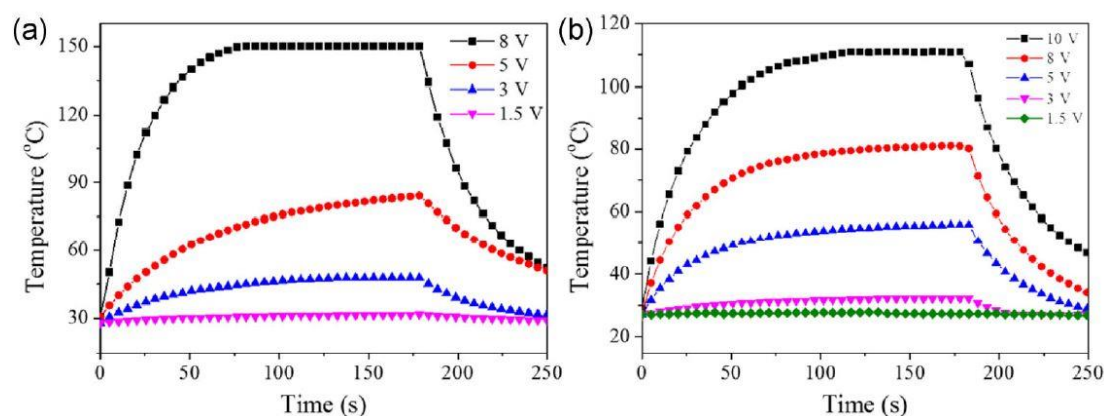


**Figure 1. 16** Thermal response of networks with (a)  $6.1 \Omega/\text{sq}$  and (b)  $17 \Omega/\text{sq}$  sheet resistance, under various applied voltages [98].

In another Cu NW based TTFH study, Cu NWs were synthesized via solution based method and deposited onto glass substrates by spray deposition. Then,  $\text{Al}_2\text{O}_3$  was deposited onto Cu NW networks via atmospheric pressure spatial atomic layer deposition (AP-SALD). The conformal  $\text{Al}_2\text{O}_3$  thickness was reported to be about 50 nm. Although networks with high electrical conductivity and optical transmittance were studied for stability tests, the sheet resistance and transmittance of Cu NW based TTFH was not specified. Only the resistance of the network was reported as 19

$\Omega$ . Optical transmittance of the networks both before and after  $\text{Al}_2\text{O}_3$  deposition were not disclosed. These Cu NW networks with a 50 nm  $\text{Al}_2\text{O}_3$  protection layer was heated to 200 °C under an applied bias of 7 V. Moreover, Cu NW based TTFHs were heated to 50 °C for 2.5 hours and 10 repetitive heating and cooling cycles were practiced in order to demonstrate their long term stability [99].

#### **1.2.2.6. Metal Mesh**

Metal mesh electrodes are metal wires formed on a substrate with a mesh geometry. Metallic wires can be formed on a substrate either in a symmetrical and uniform geometry or in a random geometry. Uniform and symmetrical metal mesh electrodes are produced by photolithography, laser printing and electron beam lithography. Random metal mesh electrodes, on the other hand are produced by inkjet printing, electrospinning and crackle lithography [100]. Metal mesh electrodes can be produced with various metal thicknesses and widths. Although the transmittance of electrodes are larger than 80% they are not regarded as transparent since metal meshes are visible with pattern widths above tens of microns. To have transparent metal mesh electrodes, the wire width must be below 5  $\mu\text{m}$ . The major disadvantage of metal mesh electrodes is the high cost of fabrication since the metallic patterns are not easy to prepare. The fabrication cost increase with decreasing metal thickness. Recently introduced crackle lithography offers a solution to the formation of random metal mesh electrodes. Metal mesh electrodes with low metal mesh thicknesses can be produced by this method. Although, crackle lithography lowers the cost of metal mesh geometry formation, physical deposition of metals require expensive high vacuum based processes. Metal mesh electrodes offer high mechanical flexibility and environmental stability over metal NW networks since the wire thickness is higher [101]. The optical transmittance and sheet resistance of metal mesh electrodes depend on the type of material, mesh geometry, metal width and thicknesses. Upon optimization high performance transparent metal mesh electrodes with sheet resistance and optical transmittance of 7  $\Omega/\text{sq}$  and 86 were produced, respectively [102].

Metal mesh based TTFHs were investigated in the literature using Ag, Cu and Au meshes. Ag mesh based TTFH was produced by crackle lithography method on PET substrates. The thickness and width of Ag layers were within 75 - 150 nm and 5.4  $\mu\text{m}$ , respectively. Ag metal mesh based TTFHs with a sheet resistance and optical transmittance of 8.9  $\Omega/\text{sq}$  and 75%, respectively, were heated to 95  $^{\circ}\text{C}$  under an applied bias of 6 V. Moreover, successful deicing tests were performed with these metal meshes [100]. In another study by Khan et al., Cu mesh based TTFH was produced using photolithography on glass substrates. The thickness and width of Cu layers were around 1.8  $\mu\text{m}$  and 4  $\mu\text{m}$ , respectively. High performance meshes with very low sheet resistance (0.3  $\Omega/\text{sq}$ ) at reasonable transmittance (78%) was produced with this method. This mesh was heated to 80  $^{\circ}\text{C}$  under an applied bias of 0.21 V. The low sheet resistance of Cu mesh based TTFH enabled energy efficient temperature increase even at low applied biases. The time dependent thermal behavior of this mesh under different applied biases is provided in Figure 1.17 [103].

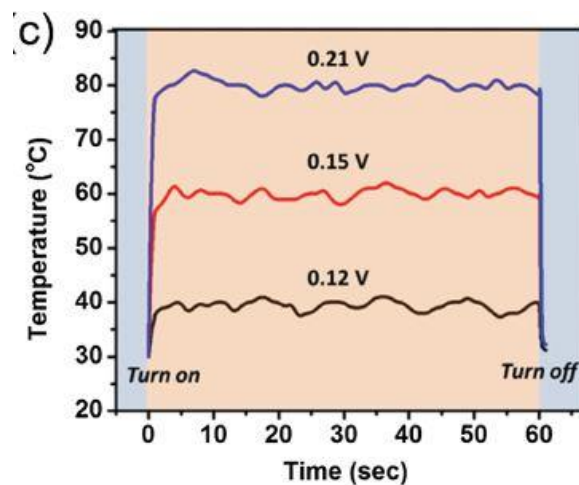


**Figure 1. 17** Time dependent thermal behavior of Cu mesh based TTFH under different applied voltages [103].

Au mesh based TTFH was also studied in literature by Rao et al. Au mesh based TTFH was fabricated by crackle lithography method on quartz substrates. The

thickness and width of Au layers were 220 nm and 2  $\mu\text{m}$ , respectively. High performance meshes with a sheet resistance and optical transmittance of 5.4  $\Omega/\text{sq}$  and 87%, respectively, were produced in this study. This mesh was heated to 600  $^{\circ}\text{C}$  under an applied bias of 15 V. This is the highest temperature obtained for TTFHs in the literature and this result has not been reproduced by any other research group either with gold mesh or with other materials. The highest achieved temperatures lie around 300  $^{\circ}\text{C}$  in literature disregarding this particular work [65]. In addition, Rayleigh instability did not occur and was not mentioned in this work.

### **1.3. Motivation for This Thesis**

In recent years, transparent heaters gained attention due to demand of applications such as defogging and deicing of optical displays and windows and extending operation temperature of LCDs. Conventional transparent heater material is ITO. However, as discussed earlier, ITO has a lot of disadvantages so studies mainly focused on replacing ITO with more advantageous TC materials. Mainly, TTFHs are made of metal oxides such as FTO, AZO and GZO, CNT network, graphene, metal NW networks (such as Ag and Cu), hybrid materials and metal meshes (such as Ag, Cu and Au). There are some advantages and disadvantages of all these materials as disclosed before. The important parameters for TTFHs are sheet resistance, transmittance and process cost. The sheet resistance should be as low as possible due to Joule heating principle. The transmittance should be as high as possible. Low process cost is favorable for the large scale utilization of these heaters. All these, TTFH materials utilized in literature are compared in terms of overall sheet resistance, transmittance and process cost in Table 1.3.

**Table 1. 3** Comparison chart for different TTFH materials [20].

Plus signs indicate better values.

<b>Paramaters</b>	<b>Metal Oxides</b>	<b>CNTs</b>	<b>Graphene</b>	<b>Metal NW</b>	<b>Hybrid</b>	<b>Metal Mesh</b>
Sheet Resistance	++++	+++	+++	++	+	+
Transmittance	+++	+++	++++	++++	++++	+++
Process Cost	++	++	+++	+	++	++

Metal NW networks, hybrid materials and metal meshes are apparently the best materials for TTFHs according to Table 1.3. In general, for metal NW networks, Ag NWs are used due to their high optoelectronic performance. In recent years, Cu NWs are started to be used and started to replace Ag NWs in some of the applications. This is because Cu is almost equally conductive and much cheaper than Ag in bulk form. There is only limited amount of research on Cu NW based TTFHs and all of them utilized a protection layer in hybrid form on Cu NWs to prevent oxidation of Cu NWs at elevated temperatures.

In this thesis, TTFH performance of Cu NW networks with ALD deposited shells were investigated in detail. Two different oxides were utilized in these investigations namely  $\text{Al}_2\text{O}_3$  and ZnO. The latter oxide was used for the first time as protection layer on Cu NW networks for TTFHs. 4 different oxide thicknesses were investigated. The aim of this thesis is to provide a detailed parametric analysis on optoelectronic performance and thermal behavior of Cu NW / metal oxide core / shell hybrid structures.

## CHAPTER 2

### EXPERIMENTAL DETAILS

#### 2.1. Synthesis of Copper Nanowires

For the synthesis of Cu NWs, a slightly modified recipe of solution based method was used [78]. Copper (II) chloride dihydrate ( $\text{CuCl}_2$ ) ( $\geq 99.0\%$ ), D-(+) - glucose monohydrate (anhydrous, 97.5-102.0%), hexadecylamine (HDA) ( $\geq 94.0\%$  (a/a)) and deionized water (18.3 M $\Omega$ ) were used in this route. All chemicals were purchased from Sigma-Aldrich.  $\text{CuCl}_2$ , glucose and HDA were used as the copper source, reducing agent and capping agent, respectively. 147 mg  $\text{CuCl}_2$ , 350 mg glucose and 1260 mg HDA were dissolved in 70 mL distilled water and left for stirring for 12 hours at room temperature. After 12 hours, homogeneous mixture with whitish blue color was obtained. Then, this mixture was placed in a 100 mL capacity Teflon lined autoclave. The autoclave temperature was increased to 100 °C with the help of a laboratory oven and left at this temperature for 12 hours under autogenous pressure. Afterwards, autoclave was taken out from the oven and allowed to cool to room temperature. The color of the final mixture was brownish red which included Cu NWs, Cu byproducts and supernatant. Photos showing the solutions both before and after the synthesis are provided in Figure 2.1.

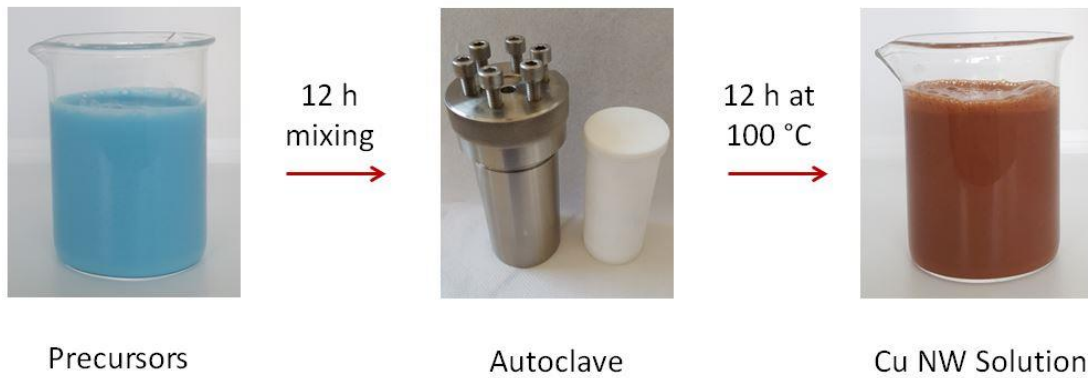


**Figure 2. 1** Photographs of Cu NW solutions before and after the synthesis with Teflon lined autoclave.

Following synthesis, NWs were purified through two times washing with deionized water via centrifugation (at 7000 rpm for 10 minutes). Afterwards, byproducts such as nanoparticles, nanospheres and nanopyramids were eliminated from the NWs via multiphase separation. Supernatant free Cu NW solution was suspended in DI water and chloroform (hydrophobic organic solvent). The solution was stirred via a magnetic stirrer for 5 minutes. After that, DI water and chloroform were immediately separated from each other and formed a clear interface. Due to the surface tension, NWs were gathered in chloroform and byproducts sink to the bottom of water. Then, chloroform solution with Cu NWs were separated from the DI water and centrifuged at 7000 rpm for 10 minutes to get rid of chloroform [104]. To obtain a dispersed NW solution for further operations, 2 wt% polyvinylpyrrolidone (PVP) (MW = 55000, monomer-based calculation) - ethanol solution was prepared. The NWs were centrifuged with this solution twice at 7000 rpm for 10 minutes. Finally, to get rid of excess PVP, NWs were washed with ethanol twice at 7000 rpm for 10 minutes [105].

## 2.2. Fabrication of Copper Nanowire Networks

Dispersed and byproduct free Cu NWs were mixed with ethanol. Quartz was utilized as a substrate due to lower thermal expansion coefficient compared to silica glass. 2.54 x 2.54 cm and 1 mm thick quartz substrates were cleaned before network deposition with the help of acetone ( $\geq 99.9\%$ ), ethanol ( $\geq 99.9\%$ ) and deionized water (18.3 M $\Omega$ ) through ultrasonication. Cu NWs were deposited onto quartz substrates with N<sub>2</sub> fed air brush through spray deposition. Quartz substrates were placed onto a hot plate at 100 °C to instantly remove ethanol. In spray deposition, N<sub>2</sub> pressure and the distance between the air brush and the substrates are important parameters for the performance of networks. The distance and N<sub>2</sub> pressure was 15 cm and 1.5 atm during spray deposition, respectively. A photograph taken during spray coating of Cu NW - ethanol solution onto quartz substrates is shown in Figure 2.2.

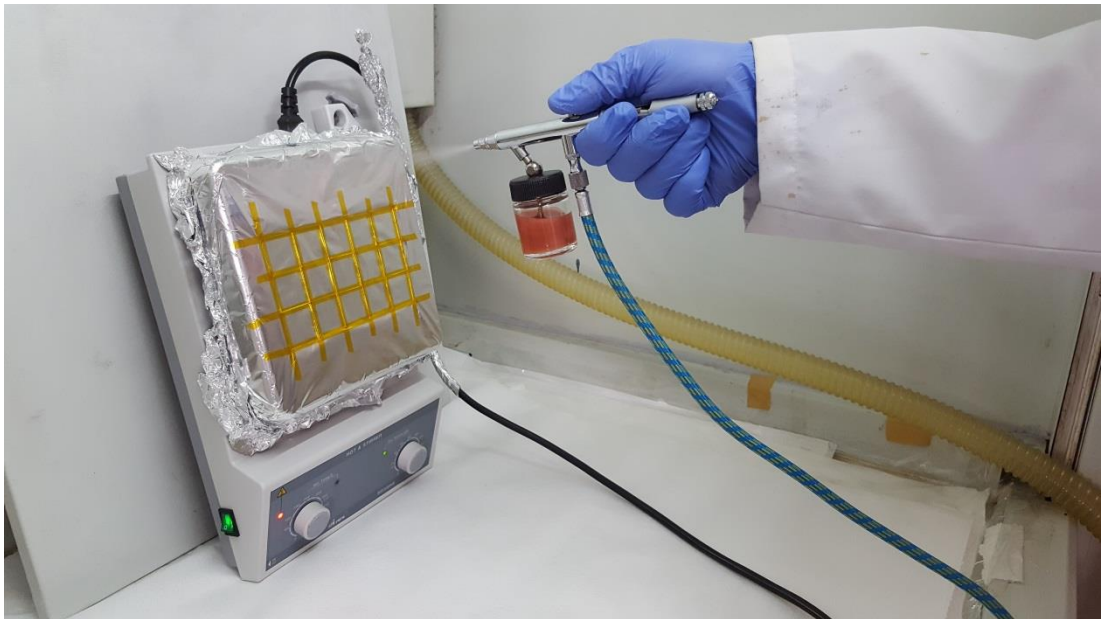


**Figure 2. 2** Spray deposition of Cu NWs onto quartz substrates.

Following deposition, resistance of Cu NW networks were measured around  $M\Omega$ . This is because of the residual organics, PVP and high contact resistance of the junctions. Therefore, Cu NW networks were annealed under inert atmosphere to get rid of excess synthesis organics, PVP and to fuse Cu NWs at junctions. Annealing was performed under vacuum at 200 °C with the help of Aixtron – Nano-instruments Black Magic II plasma enhanced chemical vapor deposition (PECVD) system.

### 2.3. Contact Formation with Physical Vapor Deposition

The contacts were deposited onto Cu NW networks for biasing and resistance measurements. Contacts were deposited using a shadow mask. The shadow mask geometry was two parallel 3 mm wide lines that are 12 mm away from each other. 100 nm thick Ag contacts were deposited onto Cu NW networks at a rate of 1.2 Å/s through thermal evaporation at a base pressure of  $2.4 \times 10^{-6}$  atm. A photograph of Cu NW network on quartz with Ag contacts is provided in Figure 2.3.

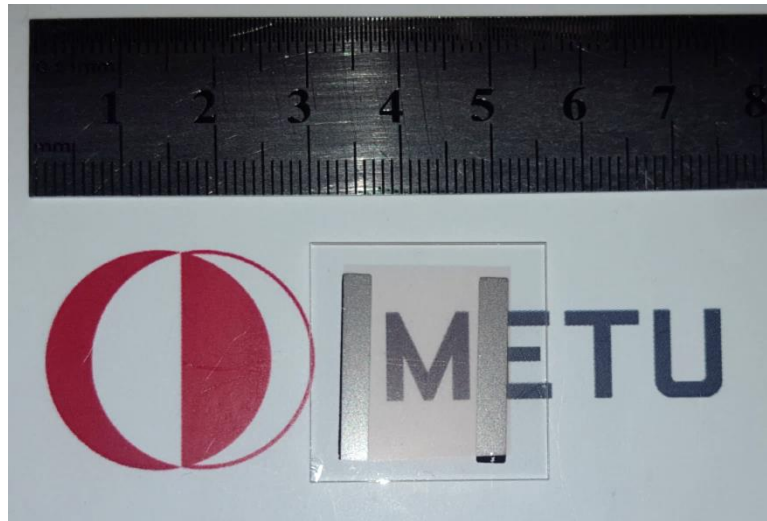


**Figure 2. 3** Parallel Ag thin film contacts deposited onto Cu NW network.

## 2.4. Atomic Layer Deposition onto Copper Nanowire Networks

Cu NW networks with parallel contacts were placed into the ALD chamber. In ALD, thin films were deposited onto substrates cycle by cycle until the desired thickness is obtained. In Al<sub>2</sub>O<sub>3</sub> deposition onto Cu NW networks, the precursors and carrier gas were trimethylaluminum (TMA - Al(CH<sub>3</sub>)<sub>3</sub>), water (H<sub>2</sub>O) and N<sub>2</sub>, respectively. The consecutive 15ms/10s/15ms/10s (under 20 sccm carrier N<sub>2</sub> gas) injections of TMA/N<sub>2</sub>/H<sub>2</sub>O/N<sub>2</sub> were applied onto Cu NW networks, respectively. The overall reaction for 1 cycle ALD of Al<sub>2</sub>O<sub>3</sub> is provided in following reaction;



The ALD count of cycles was optimized prior to the deposition for the deposition of metal oxides with desired thickness. ALD of Al<sub>2</sub>O<sub>3</sub> was operated under 3.5x10<sup>-1</sup> torr and 200 °C for 40, 120, 200 and 400 cycles to obtain Al<sub>2</sub>O<sub>3</sub> thicknesses of 5, 15, 25 and 50 nm, respectively.

For ZnO deposition onto Cu NW networks, the precursors and carrier gas were diethyl zinc (DEZ – Zn(C<sub>2</sub>H<sub>5</sub>)<sub>2</sub>), H<sub>2</sub>O and N<sub>2</sub>, respectively. The consecutive 50ms/10s/50ms/10s (under 20 sccm carrier N<sub>2</sub> gas) injections of DEZ/N<sub>2</sub>/H<sub>2</sub>O/N<sub>2</sub> were applied onto Cu NW networks, respectively. The overall reaction for 1 cycle ALD of ZnO is provided in following reaction;



The ALD count of cycles was optimized prior to the deposition to achieve desired thickness. ALD of ZnO was operated under 5.2x10<sup>-1</sup> torr and 175 °C for 25, 75, 125 and 250 cycles to obtain ZnO thicknesses of 5, 15, 25 and 50 nm, respectively.

## **2.5. Characterization Methods**

### **2.5.1. Scanning Electron Microscopy (SEM)**

The morphology of as synthesized Cu NWs, bare and Al<sub>2</sub>O<sub>3</sub> and ZnO deposited Cu NW networks were examined using scanning electron microscopy (SEM). SEM studies were performed on FEI NOVA NANO SEM 430 at an operating voltage of 10 kV. SEM samples of as synthesized Cu NWs were prepared by dropping Cu NW solution onto single crystal silicon (Si) wafers and then evaporating the solvent (ethanol or chloroform) via a hot plate. Si wafers were cleaned before dropping Cu NW solution with the help of acetone, ethanol and deionized water through ultrasonication. Since bare and Al<sub>2</sub>O<sub>3</sub> and ZnO deposited Cu NW networks were electrically conductive no extra gold / carbon was used for SEM analysis.

### **2.5.2. Transmission Electron Microscopy (TEM)**

Transmission electron microscopy (TEM) was used to further characterize the morphology of as synthesized Cu NWs and Al<sub>2</sub>O<sub>3</sub> and ZnO deposited Cu NW networks. TEM studies were performed on JEOL TEM 2100F at an operating voltage of 200 kV. To observe cross section of Cu NWs, single Cu NW placed on Si substrates was cut by Focused Ion Beam (FIB) and TEM sample was prepared by it (courtesy of Meltem Sezen from Sabancı University). For TEM analysis of Al<sub>2</sub>O<sub>3</sub> and ZnO deposited Cu NW networks, networks were scraped off from the substrates, sonicated with ethanol and drop casted onto carbon coated Cu mesh TEM grids.

### **2.5.3. Sheet Resistance Measurements**

The sheet resistance measurements were carried out using a Keithley 2400 sourcemeter. To measure the sheet resistance of bare and Al<sub>2</sub>O<sub>3</sub> and ZnO deposited

Cu NW networks, a homemade 2 probe measurement setup was used. Eutectic gallium-indium (Ga-In) alloy was used as the contacts. Eutectic Ga-In was in liquid form at room temperature, which enables easier contact formation with NWs during measurements. Probes had a diameter ( $D$ ) of 1.5 mm and their separation ( $L$ ) was 3 mm. The resistance of the networks was measured through a  $\pm 1V$  scan at a scan speed of 100 mV/s. Sheet resistance of the networks was then calculated by Equation 2.1.

$$R = R_s \frac{L}{D} \quad (2.1)$$

, where  $R$  is resistance ( $\Omega$ ),  $R_s$  is sheet resistance ( $\Omega/\text{sq}$ ),  $L$  is length (3 mm) and  $D$  is diameter of the contacts (1.5 mm).

#### **2.5.4. Transparency Measurements**

The transparency measurements were carried out on Agilent 8453 UV-VIS spectrometer. Bare and  $\text{Al}_2\text{O}_3$  and ZnO deposited Cu NW networks were used for the measurements. The measurements were taken in the visible range (390 to 700 nm).

#### **2.5.5. Areal Mass Density Calculations**

The optoelectronic properties of Cu NW networks strongly depend on the NW density. Areal mass density (amd) was used to define the NW density within the networks. Amd is simply the mass of NWs over total area in the network. Image J program with Geom-Density-Macro plugin was used to calculate amds of the fabricated networks. To calculate amds, SEM images of the networks converted to gray scale images and calculation was performed by Geom-Density-Macro plugin. This plugin calculates the geometrical density of the networks. The formula of geometrical density is provided in Equation 2.2.

$$\text{Geometrical density} = \frac{l_T}{A_T} \quad (2.2)$$

, where  $l_T$  is total length of NWs in the SEM image and  $A_T$  is total area of the image.

Volume of NWs in the image was calculated through Equation 2.3.

Volume = Number of wires x volume of single NW

$$\text{Volume} = \frac{l_T}{l_{average}} \pi r_{average}^2 l_{average}$$

$$\text{Volume} = l_T \pi r_{average}^2 \quad (2.3)$$

, where  $l_{average}$  and  $r_{average}$  are average length and radius of Cu NWs, respectively.

Mass of the NWs in the image was calculated through Equation 2.4.

Mass = Volume of NWs x density of Cu

$$\text{Mass} = l_T \pi r_{average}^2 \rho \quad (2.4)$$

, where  $\rho$  is density of copper.

Finally, amd of Cu NW networks in the image was calculated through Equation 2.5.

amd = Mass of NWs / Total Area

$$\text{amd} = \frac{l_T \pi r_{average}^2 \rho}{A_T}$$

$$\text{amd} = \text{Geometrical Density} \pi r_{average}^2 \rho \quad (2.5)$$

### **2.5.6. X-Ray Diffraction (XRD) Analysis**

X-Ray Diffraction (XRD) analysis was carried out on as synthesized Cu NWs to examine the phases present and the crystal structure of Cu NWs. As synthesized Cu NW foils were produced by vacuum filtration method to prevent any substrate related diffractions. A Rigaku D Max – 2000 PC diffractometer at a scan rate of 2°/min with Cu K $\alpha$  radiation at an operating voltage of 40 kV was used for XRD analysis. The 2 $\theta$  angle varied from 10 to 90 °.

Crystalline structure of bare Al<sub>2</sub>O<sub>3</sub> and ZnO thin films were determined by grazing incidence X-ray diffraction (GIXD) method. Al<sub>2</sub>O<sub>3</sub> and ZnO deposited quartz substrates were used for these measurements. A Rigaku Ultima IV diffractometer at a scan rate of 2 °/min with Cu K $\alpha$  radiation at an operating voltage of 40 kV and an incident angle of 0.4° was used for GIXD analysis. The 2 $\theta$  angle varied from 30 to 70 °.

### **2.5.7. X-Ray Photoelectron Spectroscopy (XPS) Analysis**

X-Ray photoelectron spectroscopy (XPS) analysis was carried out on Al<sub>2</sub>O<sub>3</sub> and ZnO deposited Cu NW networks before and after thermal measurements to examine the chemical changes in the networks. XPS was collected by PHI 5000 Versa Probe Spectrometer (284.8 eV was set as C1s reference).

### **2.5.8. Atomic Force Microscopy (AFM)**

The topography of bare Al<sub>2</sub>O<sub>3</sub> and ZnO thin films were analyzed using atomic force microscopy (AFM). AFM studies were performed on Veeco Multimode V instrument under tapping mode. Roughness values of the thin films were obtained

from an area of 2  $\mu\text{m}$  x 2  $\mu\text{m}$ . ALD deposited bare  $\text{Al}_2\text{O}_3$  and ZnO thin films on quartz substrates were used for AFM measurements.

### **2.5.9. Ellipsometry Measurements**

Spectroscopic ellipsometry (SE) measurements were performed on bare  $\text{Al}_2\text{O}_3$  and ZnO thin films on quartz substrates by vertical variable angle spectroscopic ellipsometry (V-VASE) within the wavelength region of 400 to 1000 nm with angles of 60, 65 and 70°. The measured data were analyzed with WVASE32 software. Ellipsometry measures two quantities; namely amplitude ratio ( $\Psi$ ) and phase difference ( $\Delta$ ). These quantities were fitted into an equation with multiple angles of incidence to calculate the refractive index ( $n$ ) of bare  $\text{Al}_2\text{O}_3$  and ZnO thin films.

### **2.5.10. Thermal Measurements**

Copper wires were attached to the networks on top of previously deposited 100 nm thick Ag contacts via Ag paste. This protected both the networks and contacts from the damage that might occur with crocodile clips. A special setup was built for thermal measurements including a power supply, thermocouples and a computer. This thermal measurement setup is schematized in Figure 2.4.

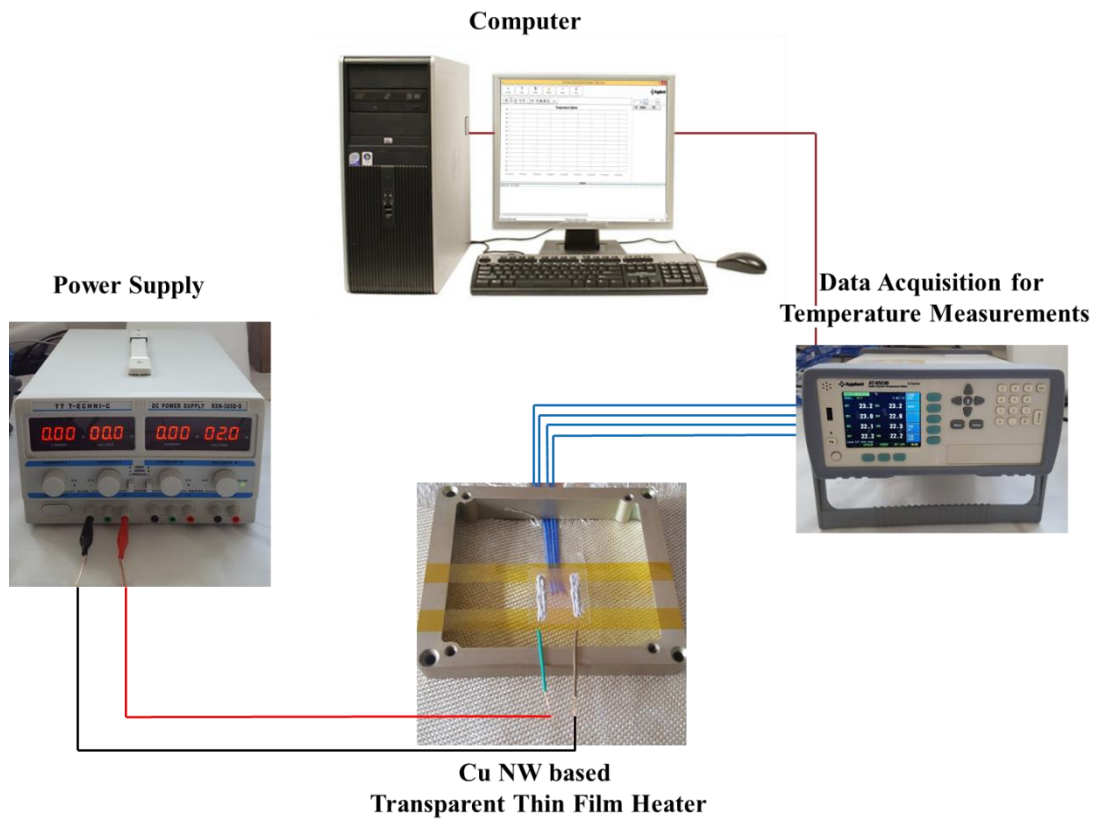


**Figure 2. 4** Illustration of the thermal measurement setup used in this work.

A DC Power Supply (RXN-305D-II) was connected to the Cu NW network for biasing. 4 T type copper - constantan thermocouples were attached to the backside of the substrates carrying Cu NW networks and the data was collected by an Applent AT4508 Multi-Channel Temperature Meter using a computer and AT45X software.

For defrosting application, substrates with Cu NW networks were placed into the freezer part of refrigerator for 1 hour for frost formation. Then, constant bias was applied to these substrates until complete defrosting.

### **2.5.11. Thermal Camera Imaging**

To determine the thermal homogeneity of the heated networks under voltage, a thermal camera (Optris PI 400 Infrared Camera) was used. Copper wire attached networks that were used for thermal measurements were also utilized for thermal camera imaging. The samples were placed onto an aluminium plate ( 1 mm thick) that was held at 60 °C on a hot plate to provide thermal contrast from the background. Data were collected using a computer and Optris PI Connect software.

## CHAPTER 3

### RESULTS AND DISCUSSION

#### 3.1. Characterization of Cu NWs

Morphological analysis of Cu NWs that were synthesized by solution based method in this work was performed by SEM. An SEM image of by-products eliminated and dispersed Cu NW network on Si wafer is provided in Figure 3.1. Homogeneously distributed Cu NWs in network form with a very few Cu nanoparticles are visible in the figure.

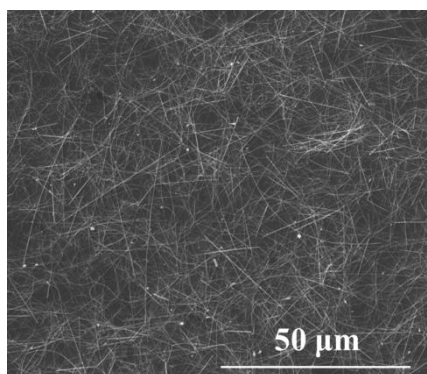


**Figure 3. 1** A SEM image of Cu NW network on Si wafer substrate.

Diameter and length distribution of synthesized Cu NWs were obtained with the help of high resolution SEM images. 100 Cu NWs were randomly selected and their diameter and lengths were measured. The diameter and length distribution of Cu NWs are provided in Figures 3.2 (a) and (b), respectively. According to these analyses, Cu NWs with diameters in the range of 30 and 100 nm and lengths up to 0.1 mm were synthesized in this work. Mean diameter and length of NWs were calculated as 50 nm and 25 μm, respectively.

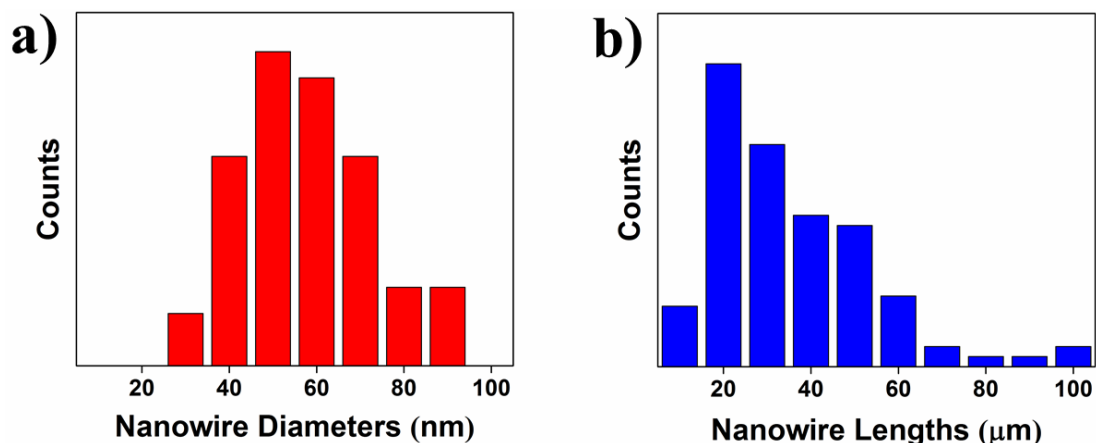


**Figure 3. 2** (a) Diameter and (b) length distributions of synthesized Cu NWs in this work.

The further morphological analysis of the as synthesized Cu NWs was performed by TEM with the help of FIB (courtesy of Meltem Sezen from Sabancı University). Cross sectional TEM image of a Cu NW is provided in Figure 3.3 (a). In the image five {111} planes of crystalline Cu are visible. Moreover, XRD analysis was performed to monitor the phase purity. The XRD pattern for as synthesized Cu NWs is provided in Figure 3.3 (b). The  $2\theta$  peaks corresponds to (111), (200) and (220) planes of FCC Cu without any CuO and Cu<sub>2</sub>O peaks within the detection limit of XRD apparatus (JCPDS 03-1018) [80].

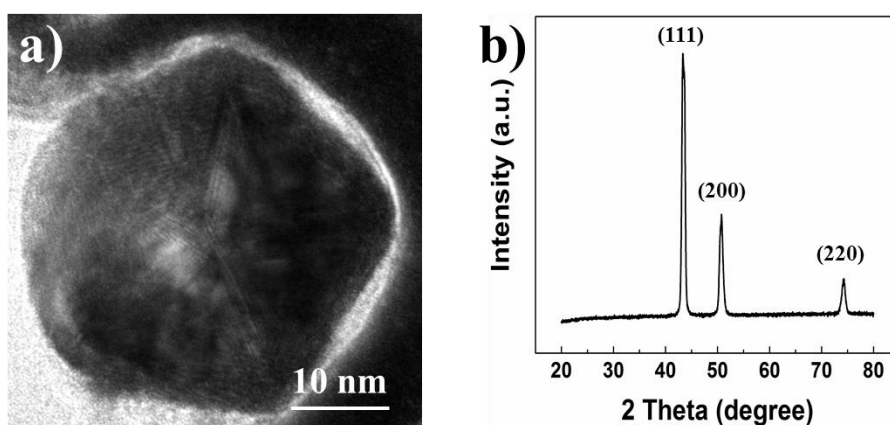


**Figure 3. 3** (a) Cross sectional TEM image of an individual Cu NW and (b) XRD pattern for as synthesized Cu NWs.

### 3.2. Effect of Nanowire Density on Optoelectronic Properties

The two important parameters for TTFHs are sheet resistance and optical transmittance both of which depend on the NW density within the networks. To investigate the effects of NW density on the performance of networks, Cu NW networks with 10 different NW densities were prepared. The difference in NW density was simply adjusted by increasing the number of spray deposition cycles. Then, sheet resistance, transmittance at a wavelength of 550 nm and amd of these networks were measured. Plot showing the sheet resistance with respect to amd of networks is provided in Figure 3.4 (a). As it is discussed in Chapter 1, after critical NW density ( $N_c$ , percolation threshold), increasing NW density results in a decrease of sheet resistance of the networks. This is due to the increase in the number of pathways for charge transport. It should be noted that power law decrease in sheet resistance was observed with the increase in amd since number of pathways did not increase linearly with spray deposition cycles. Plot showing changes in optical transmittance with respect to amd is provided in Figure 3.4 (b). The increase in amd resulted in a decrease in transmittance since area coverage of NWs was increased. It means less light was transmitted through the networks and scattering increased with the NW density in the networks. The relationship between transmittance and amd was almost inversely linear.

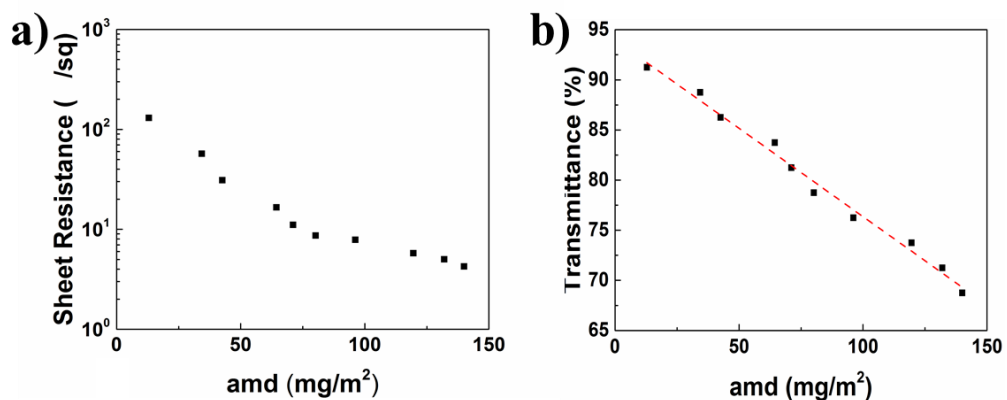


**Figure 3. 4** (a) Sheet resistance and (b) optical transmittance with respect to amd within the Cu NW networks fabricated in this work.

The relationship between transmittance and sheet resistance was determined with respect to amds of Cu NW networks. To determine the standard deviation between them, Cu NW networks with 40 different NW densities were prepared. The optical transmittance with respect to sheet resistance with standard deviation is provided in Figure 3.5. It is obvious that deviation in sheet resistance is higher in networks with lower amds. Both sheet resistance and optical transmittance of the networks should be high for optimum TTFHs performance.

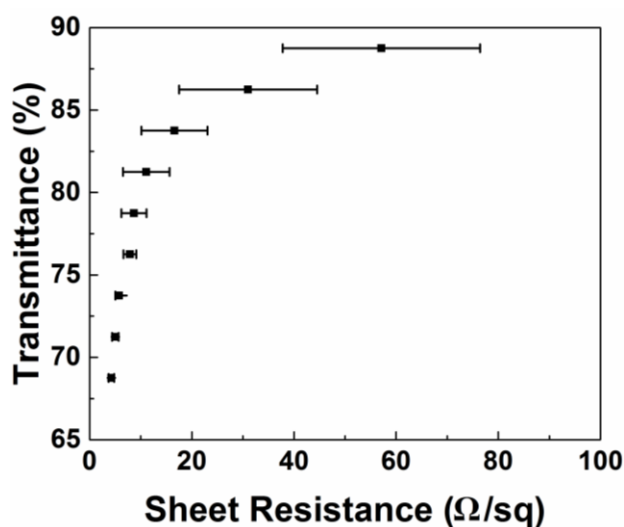


**Figure 3. 5** Transmittance versus sheet resistance graph for Cu NW networks fabricated in this work.

### 3.3. Bare Copper Nanowire Networks

To investigate the effect of NW density on thermal response, Cu NW networks with 3 different NW densities were prepared on quartz substrates for both separate  $\text{Al}_2\text{O}_3$  and ZnO depositions. The SEM images of Cu NW networks with 68.8, 101.2 and 142.0  $\text{mg/m}^2$  amds that were prepared for  $\text{Al}_2\text{O}_3$  deposition are provided in Figures 3.6 (a) - (c), respectively. As it is discussed in earlier sections, number of pathways for charge transfer was increased with the amds. Therefore, this resulted in a decrease in sheet resistance. The sheet resistances of Cu NW networks with amds of 68.8, 101.2 and 142.0  $\text{mg/m}^2$  were 10, 5 and 3.5  $\Omega/\text{sq}$ , respectively.

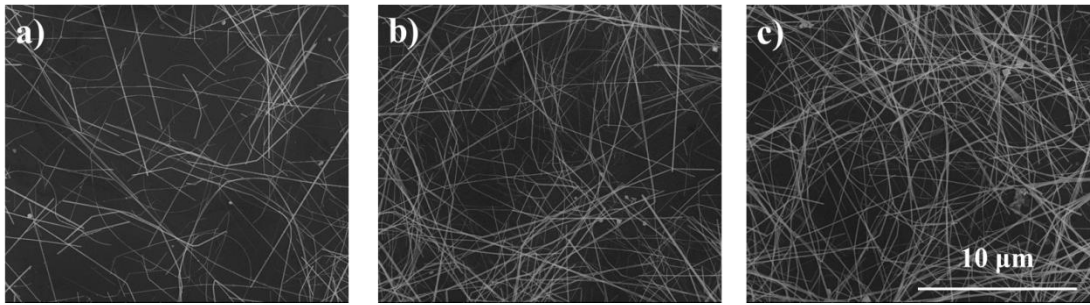


**Figure 3. 6** SEM images of Cu NW networks with amds of (a) 68.8, (b) 101.2 and (c) 142.0 mg/m<sup>2</sup>. All scales are the same.

Transmittance of these networks within the visible portion of the spectrum is provided in Figure 3.7. As it is discussed in earlier sections, number of NWs increase with the amd of networks. Therefore, these NWs result in more blockage of light and thus an overall decrease in transmittance is observed. The optical transmittances (at a wavelength of 550 nm) of Cu NW networks with amds of 68.8, 101.2 and 142.0 mg/m<sup>2</sup> were measured as 82.6, 75.3 and 68.2 %, respectively.

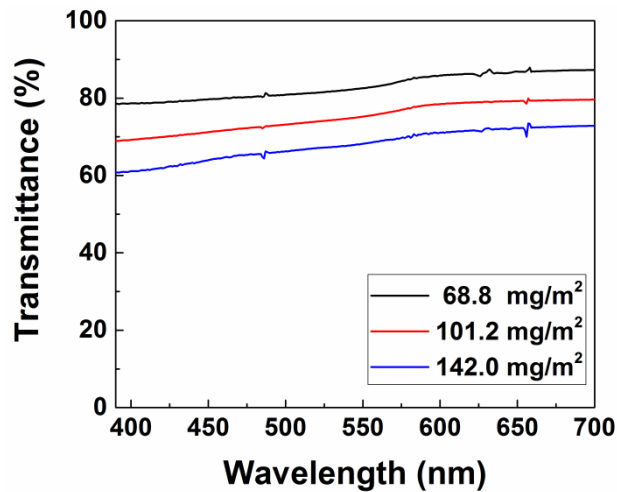


**Figure 3. 7** Spectral transmittance of Cu NW networks with amds of 68.8, 101.2 and 142.0 mg/m<sup>2</sup> used in this work for Al<sub>2</sub>O<sub>3</sub> deposition.

The SEM images of Cu NW networks with amds of 40.7, 73.1 and 101.6 mg/m<sup>2</sup> that were prepared for ZnO deposition are provided in Figures 3.8 (a) - (c), respectively. Similar to previous set for Al<sub>2</sub>O<sub>3</sub> deposition, sheet resistance of these networks were decreased with increased amds. The sheet resistances of Cu NW networks with amds of 40.7, 73.1 and 101.6 mg/m<sup>2</sup> were 15, 8 and 4.8 Ω/sq, respectively.

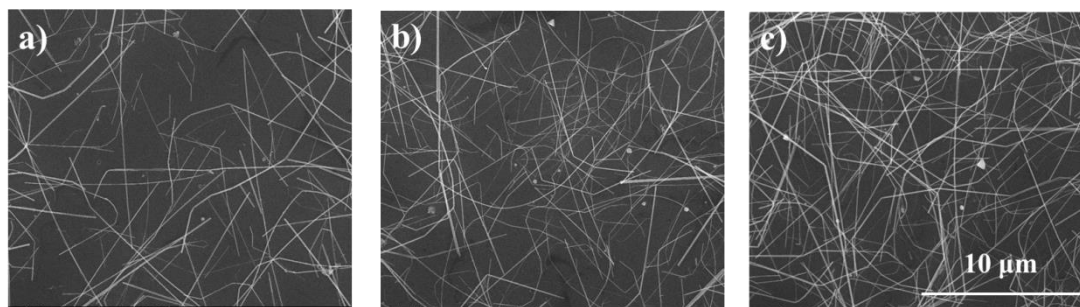


**Figure 3. 8** SEM images of Cu NW networks with amds of (a) 40.7, (b) 73.1 and (c) 101.6 mg/m<sup>2</sup>. All scales are the same.

Spectral transmittance of these networks within the visible portion of the spectrum is provided in Figure 3.9. Optical transmittances of networks were decreased with increased amds. The transmittances (at a wavelength of 550 nm) of Cu NW networks with amds of 40.7, 73.1 and 101.6 mg/m<sup>2</sup> were 86.4, 80.2 and 75.2 %, respectively.

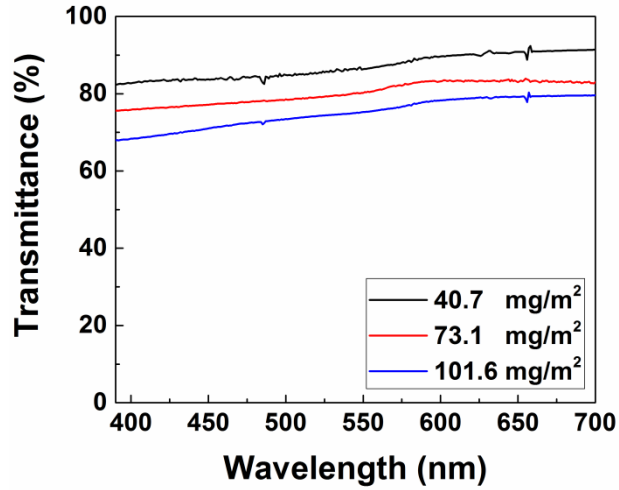


**Figure 3. 9** Spectral transmittance of Cu NW networks with amds of 40.7, 73.1 and 101.6 mg/m<sup>2</sup> used in this work for ZnO thin film deposition.

### 3.3.1. Thermal Measurements

To investigate the effect of NW density on thermal response, thermal measurements of bare Cu NW networks were performed under constant applied biases. Applied bias was increased with 1 V intervals until the networks fail. Failure is defined as the moment where the attained temperature drops gradually corresponding to an increase in sheet resistance. The bias was applied for 20 minutes and then networks were allowed to cool down to room temperature for 10 minutes. Time dependent thermal response of Cu NW networks with different amds are provided in Figures 3.10 (a) – (f).

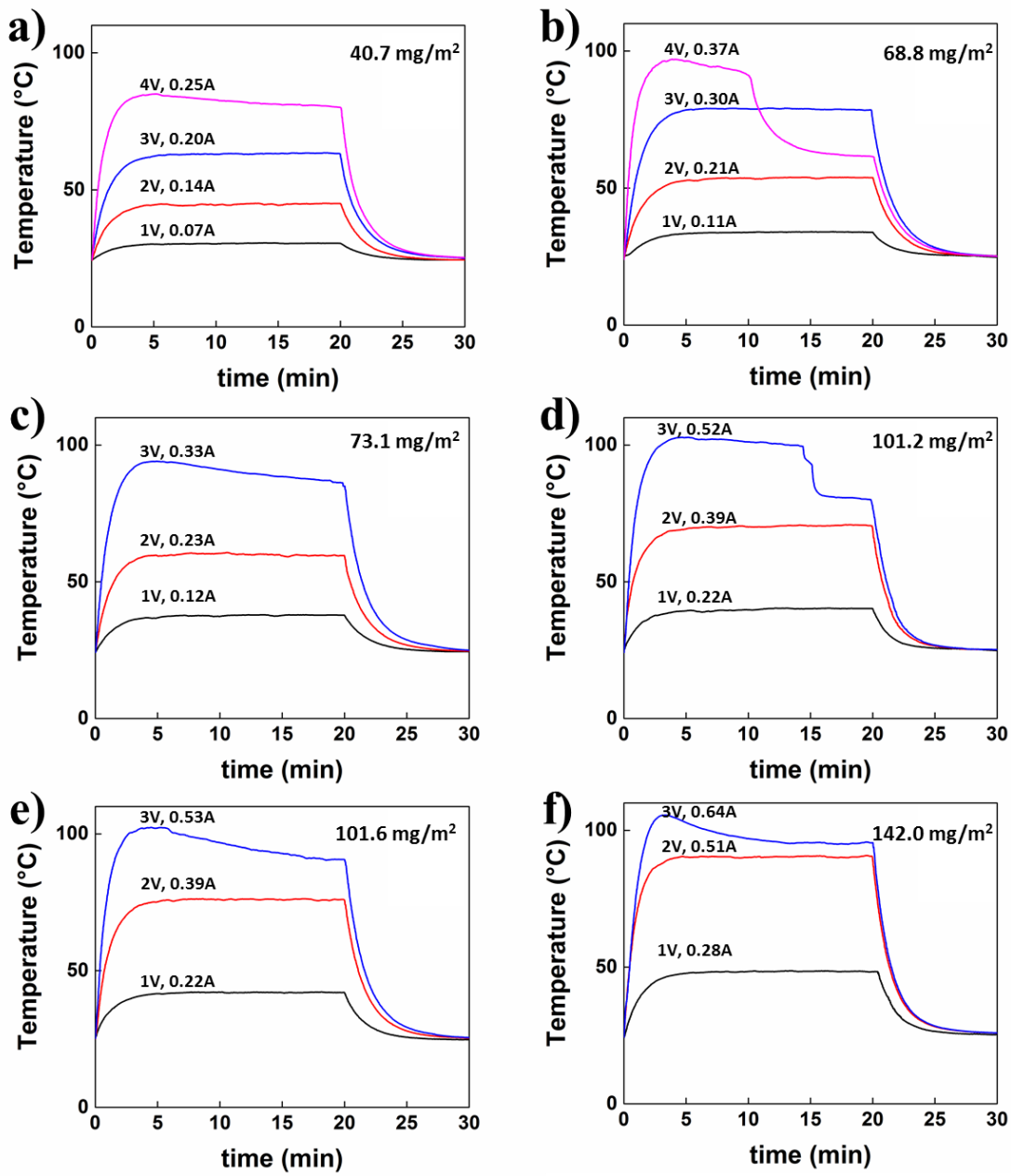


**Figure 3. 10** Time dependent thermal responses of Cu NW networks with different areal densities of (a) 40.7, (b) 68.8, (c) 73.1, (d) 101.2, (e) 101.6 and (f) 142.0 mg/m<sup>2</sup> under various applied voltages.

It is clear from Figure 3.10 that the attained temperatures without failure increases with the amd of Cu NW networks. This is in accordance to Joule heating principle. According to Joule heating, for maximum heat dissipation, maximum power is needed. At a constant applied bias, maximum power can be achieved by decreasing the sheet resistance and thus by increasing the amd of the networks. Cu NW networks with an amd of 40.7 and 68.8 mg/ m<sup>2</sup> were found to fail at an applied bias of 4V, where that the other amds were 3V. The failure results in a gradual decrease in the attained temperatures due to an increase in sheet resistance of the networks. Apart from the network with an amd of 40.7 mg/m<sup>2</sup>, Cu NW networks failed around 100 °C. This was due to oxidation of Cu NWs at elevated temperatures.

To investigate the power requirements of these networks, input power densities were calculated using Equation 3.1.

$$\text{Power density} = \frac{P}{A} = \frac{IV}{A} \quad (3.1)$$

, where  $P$  is input power,  $A$  is the effective sample area that NW networks occupy,  $I$  is the current passing through network and  $V$  is the applied bias.

Although maximum attained temperatures for most of the networks were around 100 °C, in power density calculations, maximum reproducible and stable temperatures ( $T_{\max}$ ) before failure were taken into account. Moreover, effective sample area was taken as 3.24 cm<sup>2</sup> with regard to a network size of 1.8 cm x 1.8 cm. The sheet resistance, transmittance (at 550 nm),  $T_{\max}$  and input power density values of bare Cu NW networks with different amds are provided in Table 3.1. It is observed from the table that input power density increases with increasing  $T_{\max}$  regardless of NW density within the networks.

**Table 3. 1** Optoelectronic properties and thermal response characteristics of bare Cu NW networks with different amds used in this work.

amd (mg/m <sup>2</sup> )	Sheet Resistance (Ω /sq)	Transmittance (%) (at 550 nm)	T <sub>max</sub> (°C)	Bias at T <sub>max</sub> (V)	Current at T <sub>max</sub> (A)	Input Power Density (W/cm <sup>2</sup> )
40.7	15	86.4	64	3	0.2	0.19
68.8	10	82.6	79	3	0.3	0.28
73.1	8	80.2	60	2	0.23	0.14
101.2	5	75.3	71	2	0.38	0.23
101.6	4.8	75.2	76	2	0.39	0.24
142.0	3.5	68.2	90	2	0.51	0.31

### 3.4. Aluminum Oxide Deposited Copper Nanowire Networks

To investigate the Al<sub>2</sub>O<sub>3</sub> thickness on the protection level of Cu NWs and thermal response, Cu NW networks with 4 different Al<sub>2</sub>O<sub>3</sub> thicknesses (5, 15, 25 and 50 nm) were prepared. The SEM and TEM images of an individual 50 nm Al<sub>2</sub>O<sub>3</sub> deposited Cu NW are provided in Figures 3.11 (a) and (b), respectively.

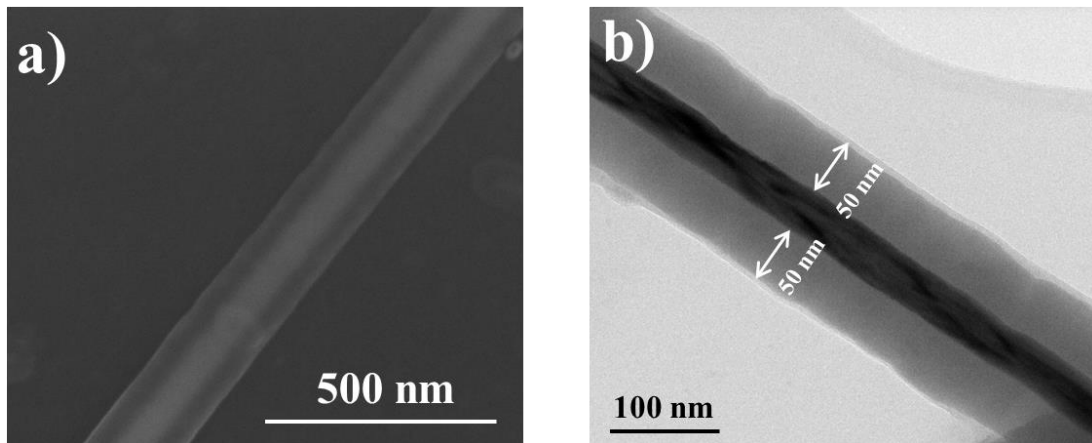


**Figure 3. 11** (a) SEM and (b) TEM images of an individual 50 nm Al<sub>2</sub>O<sub>3</sub> deposited Cu NW.

The core-shell structure with definite boundaries and smooth surface was observed in Figure 3.11. ALD deposited  $\text{Al}_2\text{O}_3$  conformally covered the whole NW network with uniform thickness. The sheet resistance of Cu NW networks remain unchanged following ALD deposition. This is because oxide shells were deposited onto already percolating and annealed network. On the other hand, overall optical transmittance values of the networks with different  $\text{Al}_2\text{O}_3$  thicknesses were found to get strongly affected because of an overall increase in the diameter of NWs and the change in effective refractive index of the medium. The optical transmittance (at 550 nm) values were found to decrease with  $\text{Al}_2\text{O}_3$  thickness. Spectral transmittance for networks with an amd of  $68.8 \text{ mg/m}^2$  and different  $\text{Al}_2\text{O}_3$  thicknesses within the visible portion of the spectrum is provided in Figure 3.12.

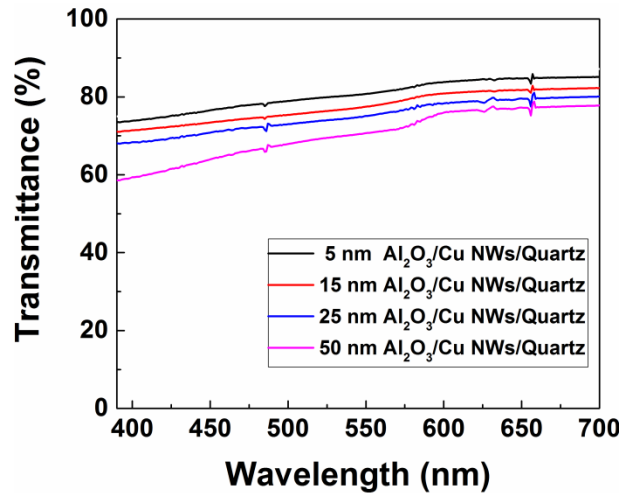


**Figure 3. 12** Spectral transmittance of Cu NW networks with an amd of  $68.8 \text{ mg/m}^2$  and different  $\text{Al}_2\text{O}_3$  thicknesses of 5, 15, 25 and 50 nm.

The XPS analysis was performed for detailed chemical analysis of the  $\text{Al}_2\text{O}_3$  deposited networks. XPS spectra of 5 nm  $\text{Al}_2\text{O}_3$  deposited Cu NW network are provided in Figure 3.13. All the XPS peaks were interpreted according to 284.8 eV for C1s reference.

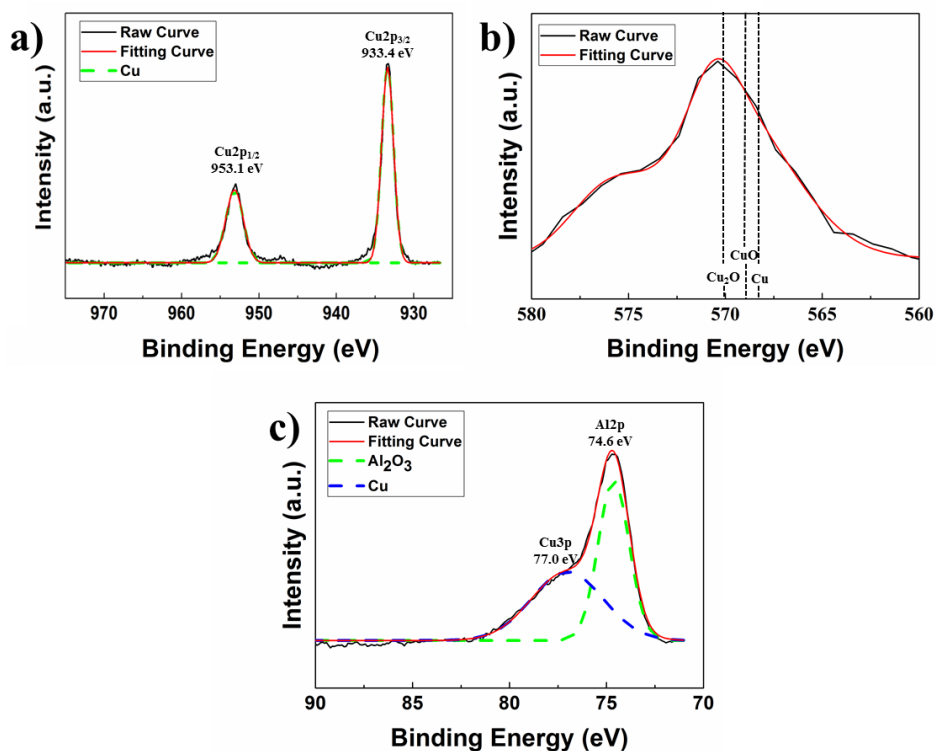


**Figure 3. 13** XPS spectra of (a) Cu<sub>2</sub>p<sub>1/2</sub> and Cu<sub>2</sub>p<sub>3/2</sub>, (b) Cu LMM Auger and (c) Cu<sub>3</sub>p and Al<sub>2</sub>p for 5 nm Al<sub>2</sub>O<sub>3</sub> deposited Cu NW network.

As it is observed from Figure 3.13 (a), the binding energy difference (19.7 eV) between Cu<sub>2</sub>p<sub>1/2</sub> (953.1 eV) and Cu<sub>2</sub>p<sub>3/2</sub> (933.4 eV) peaks is lower than 19.8 eV. It means that these peaks do belong to either metallic Cu or Cu<sub>2</sub>O [106]. Cu<sub>2</sub>p<sub>1/2</sub> and Cu<sub>2</sub>p<sub>3/2</sub> peak positions are very similar for Cu and Cu<sub>2</sub>O, so that they cannot be differentiated using these peaks [107]. To differentiate chemical state of Cu, utilizing Cu LMM Auger spectra is more appropriate since this spectra has higher sensitivity to the surface oxides. The corresponding Cu LMM characteristic peaks for Cu<sub>2</sub>O (570.1 eV), CuO (568.9 eV) and Cu (568.3 eV) are positioned on the Auger spectra [81]. Cu LMM Auger spectra (Figure 3.13 (b)) signifies presence of Cu<sub>2</sub>O rather than Cu. However, high electrical conductivity of networks and XRD analysis of as synthesized Cu NWs that is free from Cu<sub>2</sub>O or CuO peaks state that Cu NWs did not get oxidized entirely. This is because of surface oxidation of Cu NWs upon reacting with oxygen so we believe thin layer of Cu<sub>2</sub>O forms on Cu NWs in the first cycles of

ALD due to H<sub>2</sub>O precursor [108]. In Figure 3.13 (c), Cu3p and Al2p are present in the XPS spectra of Al. The Cu3p and Al2p peaks overlap with each other in the presence of Cu in Al media. Al2p peak (74.6 eV) signifies the oxidation state of the Al compound as Al<sub>2</sub>O<sub>3</sub> [109].

#### **3.4.1. Thermal Measurements**

Thermal response of Al<sub>2</sub>O<sub>3</sub> deposited Cu NW networks were monitored under constant applied biases. Applied bias was increased with 1 V intervals until the networks fail which was indicated by an increase in sheet resistance. Similar to bare networks, the bias was applied for 20 minutes and then networks were allowed to cool down to room temperature for 10 minutes. Time dependent thermal response of Cu NW networks with an amd of 68.8 mg/m<sup>2</sup> with different Al<sub>2</sub>O<sub>3</sub> thicknesses are provided in Figures 3.14 (a) – (d).

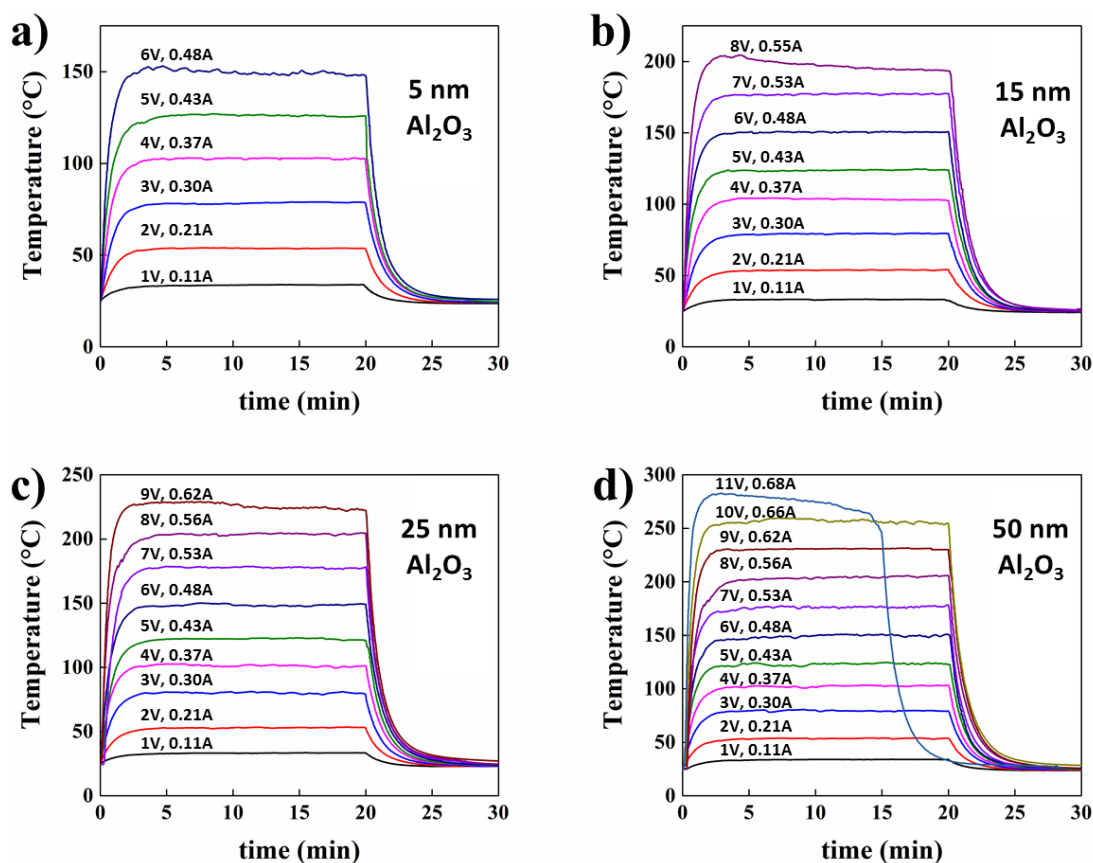


**Figure 3. 14** Time dependent thermal response of Al<sub>2</sub>O<sub>3</sub> deposited Cu NW networks with an amd of 68.8 mg/m<sup>2</sup> and different Al<sub>2</sub>O<sub>3</sub> thicknesses of (a) 5, (b) 15, (c) 25 and (d) 50 nm.

As it can be deduced from Figure 3.14, with an increase in Al<sub>2</sub>O<sub>3</sub> thickness, the networks endured higher applied biases without any change in their sheet resistances. To test the limits of these networks, applied bias was increased until failure of the networks. The failure results in a gradual decrease in attained temperatures due to sheet resistance increase of the networks. As discussed before, the fundamental problem of Cu NW heaters is the oxidation at elevated temperatures because of the free oxygen in air. The Al<sub>2</sub>O<sub>3</sub> shell layer on Cu NWs cut the interface between NWs and air. Upon the deposition of only 5 nm Al<sub>2</sub>O<sub>3</sub> onto Cu NW networks, TTFHs successfully reached to 153 °C. Increase in the thickness of Al<sub>2</sub>O<sub>3</sub> provided even better protection for the Cu NW heaters. As a result of that, T<sub>max</sub> was found to

increase with Al<sub>2</sub>O<sub>3</sub> thickness. A maximum temperature of 280 °C was attained upon deposition of 50 nm Al<sub>2</sub>O<sub>3</sub> onto Cu NW networks.

To investigate the effect of NW density on thermal response in Al<sub>2</sub>O<sub>3</sub> protected networks, thermal measurements of Cu NW networks with amds of 101.2 and 142.0 mg/m<sup>2</sup> were also performed under constant applied bias. Time dependent thermal response of 50 nm Al<sub>2</sub>O<sub>3</sub> deposited Cu NW networks with amds of 101.2 and 142.0 mg/m<sup>2</sup> are provided in Figures 3.15 (a) and (b), respectively.

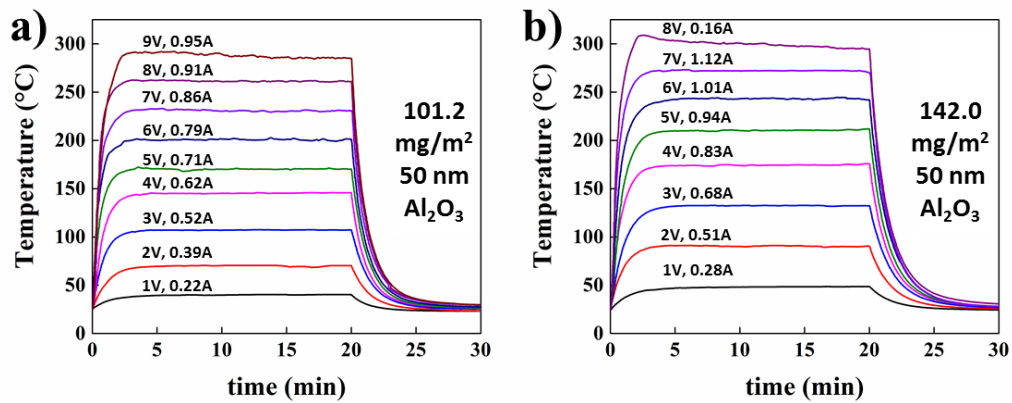


**Figure 3. 15** Time dependent thermal response of 50 nm Al<sub>2</sub>O<sub>3</sub> deposited Cu NW networks with different amds of (a) 101.2 and (b) 142.0 mg/m<sup>2</sup>.

It is evident from Figure 3.14 (d) and Figure 3.15 that the networks with higher NW densities can reach higher temperatures under the same applied bias, maximum power can be achieved by increasing the NW density within the networks. Moreover, T<sub>max</sub> was increased slightly with increasing the NW density. There are higher numbers of alternative pathways for charge transport. Therefore, even though NWs were disconnected at some points, charge transport can still take place through other alternative pathways without changing the sheet resistance of the networks. As a result of that, networks with higher NW densities endure slightly higher temperatures compared to the others with lower NW densities. Maximum temperatures of 292 °C

and 309 °C were attained through deposition of 50 nm Al<sub>2</sub>O<sub>3</sub> onto Cu NW networks with amds of 101.2 and 142.0 mg/m<sup>2</sup>, respectively.

The heating and cooling rates of Al<sub>2</sub>O<sub>3</sub> deposited Cu NW networks were calculated by differentiating the thermal response. The calculations were performed on highest applied biases for the networks. The heating and cooling rate of the networks slightly varies with applied voltages and amds of networks. For instance, the heating and cooling rates of Cu NW network with an amd of 68.8 mg/m<sup>2</sup> with 50 nm Al<sub>2</sub>O<sub>3</sub> thickness were found to be 15 °C/s and – 5 °C/s, respectively, under an applied bias of 11 V (0.68 A) corresponding to a temperature of 280 °C. Heating and cooling rate as a function of time for this network is provided in Figure 3.16. In average, heating and cooling rates of Al<sub>2</sub>O<sub>3</sub> deposited Cu NW networks were found to be 14 °C/s and – 5 °C/s, respectively. The heating rates of metal NW based hybrid TTFHs were reported between 1 and 18 °C/s [19] [74] [110] and heating rates obtained in this work were considered as high [98].

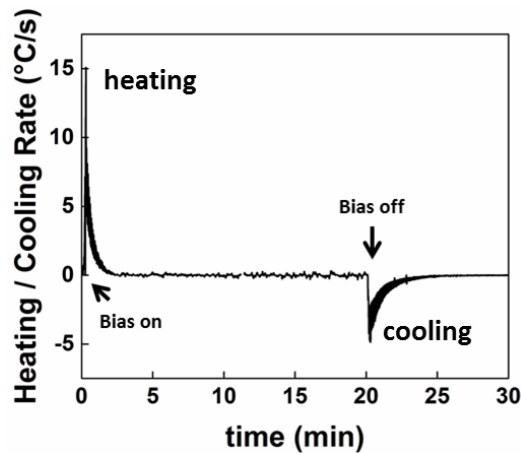


**Figure 3. 16** Heating and cooling rate as a function of time for Cu NW network with an amd of 68.8 mg/m<sup>2</sup> and Al<sub>2</sub>O<sub>3</sub> thickness of 50 nm under an applied bias of 11 V.

To investigate the power requirements of these networks, input power densities were calculated. It should be noted that  $T_{\max}$  stands for maximum reproducible and stable temperature and  $3.24 \text{ cm}^2$  ( $1.8 \text{ cm} \times 1.8 \text{ cm}$ ) was taken as the effective sample area. The sheet resistance, transmittance (at 550nm),  $T_{\max}$  and input power density values of the  $\text{Al}_2\text{O}_3$  deposited Cu NW networks with different amds and different oxide thicknesses are tabulated and provided in Table 3.2.

**Table 3. 2** Optoelectronic properties and thermal response characteristics of  $\text{Al}_2\text{O}_3$  deposited Cu NW networks with different amds and different  $\text{Al}_2\text{O}_3$  thicknesses.

amd ( $\text{mg}/\text{m}^2$ )	Sheet Resistance ( $\Omega/\text{sq}$ )	$\text{Al}_2\text{O}_3$ Thickness (nm)	Transmittance (%) (at 550nm)	$T_{\max}$ ( $^{\circ}\text{C}$ )	Bias at $T_{\max}$ (V)	Current at $T_{\max}$ (A)	Input Power Density ( $\text{W}/\text{cm}^2$ )
68.8	10	5	80.8	127	5	0.43	0.66
		15	77.5	178	7	0.53	1.14
		25	75.1	205	8	0.56	1.38
		50	70.7	260	10	0.66	2.04
101.2	5	5	73.5	146	4	0.62	0.76
		15	70.2	171	5	0.71	1.10
		25	67.9	202	6	0.79	1.46
		50	63.4	263	8	0.91	2.25
142.0	3.5	5	66.5	133	3	0.52	0.48
		15	63.2	175	4	0.83	1.02
		25	60.8	210	5	0.94	1.45
		50	58.0	273	7	1.12	2.42

It is observed from Table 3.2 that at the same applied bias, input power density of Cu NW networks with higher amds was higher since current passes through them was higher than networks with lower amds. As a result of that higher temperatures were attained by Cu NW networks with higher amds. For similar attained temperatures, input power density of some Cu NW networks were close to each other regardless of

the NW density. For instance, input power densities of 1.46 and 1.45 W/cm<sup>2</sup> were required to increase the temperature of the networks around 205 °C (Cu NW networks with 25 nm Al<sub>2</sub>O<sub>3</sub> thickness with amds of 101.2 and 142.0 mg/m<sup>2</sup>). However, for Cu NW network with 25 nm Al<sub>2</sub>O<sub>3</sub> thickness with an amd of 68.8 mg/m<sup>2</sup>, an input power density of 1.38 mg/m<sup>2</sup> was required to increase the temperature of the network to the same temperature. Therefore, there is no strong correlation between input power densities and attained temperatures of the networks in terms of NW density.

### 3.4.2. Repetitive Heating and Cooling Cycles

To investigate the reproducibility of thermal response of Al<sub>2</sub>O<sub>3</sub> protected Cu NW networks, repetitive heating and cooling cycles were practiced. Thermal response of 25 nm Al<sub>2</sub>O<sub>3</sub> deposited network with an amd of 68.8 mg/m<sup>2</sup> is provided in Figure 3.17 under repetitive heating and cooling cycles with an applied bias of 7 V. The procedure is the same; bias was applied for 20 minutes and networks were allowed to cool to room temperature for 10 minutes. The procedure was repeated for 10 times.

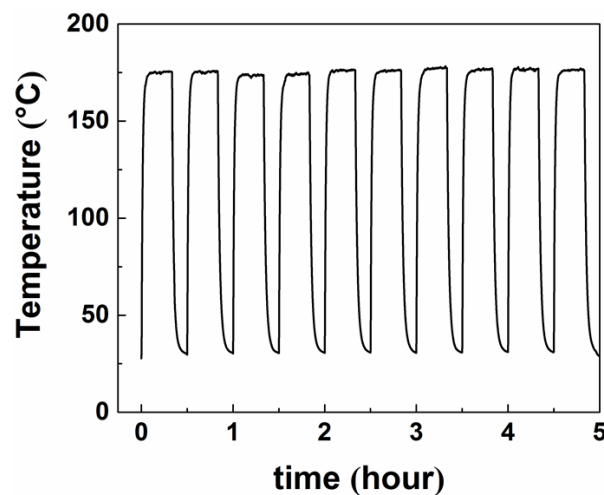


**Figure 3. 17** Thermal response of 25 nm Al<sub>2</sub>O<sub>3</sub> deposited Cu NW network with an amd of 68.8 mg/m<sup>2</sup> under repetitive heating and cooling cycles with an applied bias of 7 V.

It was observed from Figure 3.17 that the thermal performance of the network was almost identical for each cycle and not affected by repetitive heating and cooling cycles. In all the cycles, temperature was increased to around 175 °C. After the 10<sup>th</sup> cycle, the sheet resistance of the network was measured, where no change was observed. This showed that Cu NW networks can be used in applications that require successive heating and cooling cycles.

### 3.4.3. Long Term Stability

To investigate the long term stability of Al<sub>2</sub>O<sub>3</sub> protected Cu NW networks, thermal response of the networks were monitored for 24 hours under an applied bias. Thermal response of 25 nm Al<sub>2</sub>O<sub>3</sub> deposited network with an amd of 68.8 mg/m<sup>2</sup> under an applied bias of 6 V is provided in Figure 3.18. Ambient temperature was also monitored with another thermocouple as a reference, which is also provided in the figure.

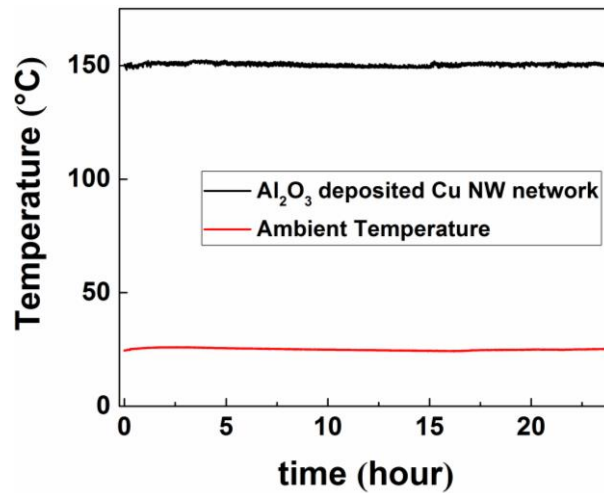


**Figure 3. 18** Long term thermal response of 25 nm Al<sub>2</sub>O<sub>3</sub> deposited Cu NW network with an amd of 68.8 mg/m<sup>2</sup> under an applied bias of 6 V.

It was observed from the figure that the temperature was highly stable for 24 hours. The temperature was found to increase to 150 °C upon the application of 6 V bias. At the end of the process, sheet resistance of the network was measured and no alteration was observed. This showed that Cu NW network TTFHs have long-term stability at the target temperatures for at least 24 h.

#### **3.4.4. Failure Mechanism**

The Al<sub>2</sub>O<sub>3</sub> protected networks were found to fail at their highest applied biases. The sheet resistances of these networks were increased and color changes were observed at some points (red brown to black) visible with the naked eye. These color changes indicate the oxidation of Cu NWs to CuO since CuO is black in color. In order to further investigate the chemical changes, XPS analysis was performed on failed networks. XPS spectra of 5 nm Al<sub>2</sub>O<sub>3</sub> deposited Cu NW network at failed points are provided in Figure 3.19. All the XPS peaks were interpreted according to 284.8 eV for C1s reference.

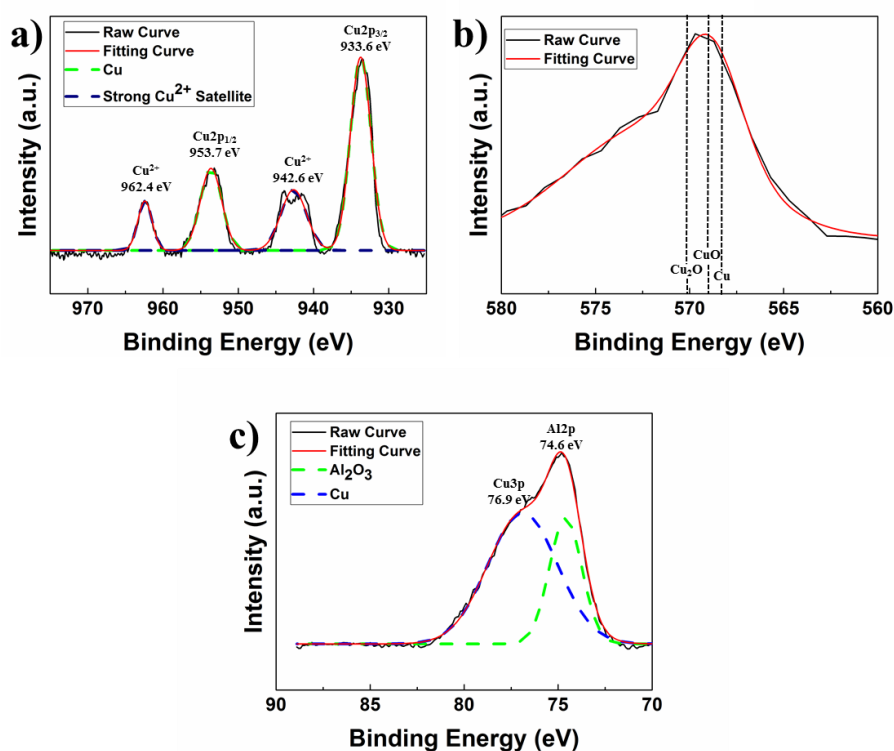


**Figure 3. 19** XPS spectra of (a) Cu<sub>2p<sub>1/2</sub></sub> and Cu<sub>2p<sub>3/2</sub></sub>, (b) Cu LMM Auger, and (c) Cu<sub>3p</sub> and Al<sub>2p</sub> of 5 nm Al<sub>2</sub>O<sub>3</sub> deposited Cu NW network at failed points.

As it is observed from Figure 3.19 (a), the binding energy difference (20.1 eV) between Cu<sub>2p<sub>1/2</sub></sub> (953.7 eV) and Cu<sub>2p<sub>3/2</sub></sub> (933.6 eV) peaks was higher than 20.0 eV. It means that these peaks do belong to CuO [106]. Moreover, strong satellite Cu<sup>2+</sup> peaks and Cu LMM Auger spectra (Figure 3.19 (b)) also supported this fact [107]. Therefore, at some points, Cu NWs were failed and oxidized to CuO. Since electrical conductivity of CuO is much lower than Cu, this failure caused an abrupt increase in the sheet resistance of the networks. Al<sub>2p</sub> peak (74.6 eV) in Figure 3.19 (c) signifies oxidation state of the Al compound as Al<sub>2</sub>O<sub>3</sub> [109]. Therefore, the chemical form of the deposited Al<sub>2</sub>O<sub>3</sub> was found unchanged at the failure points.

The morphological analysis of failed points was performed by SEM. Since the attained maximum temperatures increased with increasing Al<sub>2</sub>O<sub>3</sub> thickness, SEM analysis was conducted for all Al<sub>2</sub>O<sub>3</sub> thicknesses at failed points. SEM images of Cu

NW networks with an amd of  $68.8 \text{ mg/m}^2$  and different  $\text{Al}_2\text{O}_3$  thicknesses at failed points are provided in Figures 3.20 (a) – (d).

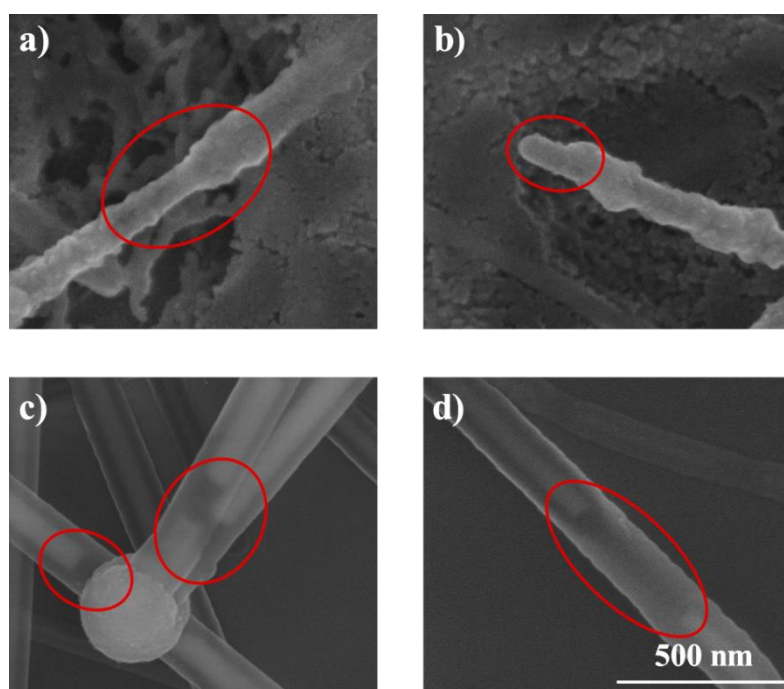


**Figure 3. 20** SEM images of failed Cu NW networks with an amd of  $68.8 \text{ mg/m}^2$  with different  $\text{Al}_2\text{O}_3$  thicknesses of (a) 5, (b) 15, (c) 25 and (d) 50 nm.

It is observed from Figure 3.19 and 3.20 that the failure mechanism of  $\text{Al}_2\text{O}_3$  protected Cu NW networks was both Rayleigh instability and oxidation of Cu NWs. Cu was accumulated at the junction points of NWs at elevated temperatures due to Rayleigh instability [74]. As a result of that Cu NWs got thinner. For low  $\text{Al}_2\text{O}_3$  thicknesses of 5 and 15 nm, thinning of NWs caused structural deformation on  $\text{Al}_2\text{O}_3$  layer so NWs were separated from the oxide shell and oxidized. The thinning and stripping of NWs from structurally deformed  $\text{Al}_2\text{O}_3$  shell were marked with red circles and provided in Figures 3.20 (a) and (b). Higher temperatures were attained for higher  $\text{Al}_2\text{O}_3$  thicknesses of 25 and 50 nm and thus further accumulation of Cu was observed on the junction points. However, the structural form of  $\text{Al}_2\text{O}_3$  did not change this time. The Cu NWs were broken into pieces inside of oxide shell [93]. Moreover, accumulated Cu on the junction points was separated from the oxide shell

and get oxidized. The sheet resistance of the networks was increased due to discontinuity between NWs and oxidation of NWs [111]. The discontinuous parts between NWs were marked with red circles and provided in Figures 3.20 (c) and (d).

### 3.4.5. Thermal Imaging

Thermal camera images of  $\text{Al}_2\text{O}_3$  protected Cu NW networks were taken to examine the thermal homogeneity of networks. Thermal camera images for 50 nm  $\text{Al}_2\text{O}_3$  deposited Cu NW network with an amd of  $68.8 \text{ mg/m}^2$  before and after failure are provided in Figures 3.21 (a) and (b), respectively. Before the failure, the network reached to  $260 \text{ }^\circ\text{C}$  under an applied bias of 10 V. A homogeneous thermal distribution (Figure 3.21 (a)) was obtained for this network. This network was failed under an applied bias of 11 V so that its sheet resistance was increased. Following failure, the network only reached  $250 \text{ }^\circ\text{C}$  under an applied bias of 11 V. The thermal image of this network (Figure 3.21 (b)) revealed presence of hot spots on the sample and showed that the temperature distribution is not uniform.

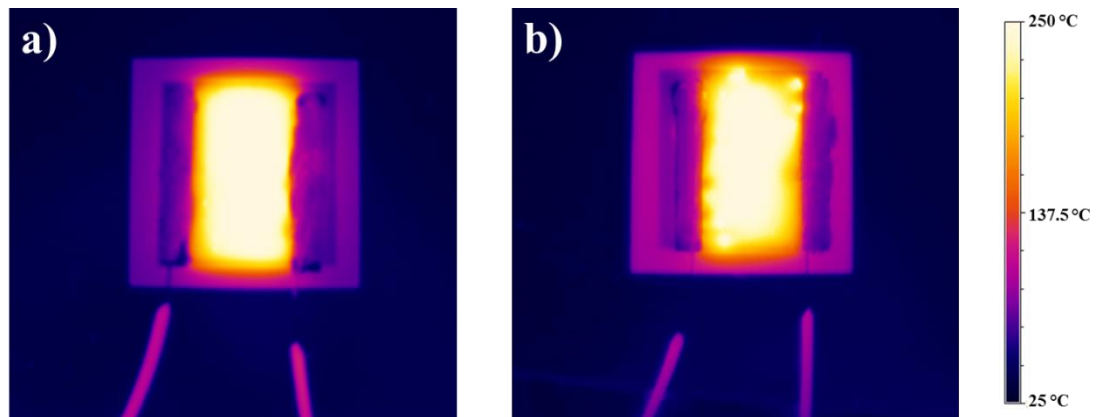


**Figure 3. 21** Thermal camera images of the Cu NW network with an amd of  $68.8 \text{ mg/m}^2$  and 50 nm  $\text{Al}_2\text{O}_3$  thickness (a) before (10 V applied bias) and (b) after (11 V applied bias) failure.

### 3.4.6. Defrosting Application

In order to demonstrate real life applicability of  $\text{Al}_2\text{O}_3$  protected Cu NW network heaters, they were utilized in defrosting applications. High heating rates ( $14\text{ }^\circ\text{C/s}$ ) and significant optoelectronic performance of the networks made them suitable for this application. Photographs of the  $5\text{ nm}$   $\text{Al}_2\text{O}_3$  deposited Cu NW network with an amount of  $68.8\text{ mg/m}^2$  both before and after defrosting application are provided in Figures 3.22 (a) and (b), respectively. The METU logo printed on a piece of paper behind the network was invisible due to the frost formation on the network as shown in Figure 3.22 (a). The frost on the network was completely removed after 28 s under an applied bias of 3 V corresponding to a temperature of  $80\text{ }^\circ\text{C}$ . After defrosting application, original transparency of the network was recovered and the METU logo on the background was clearly visible again. Rapid defrosting application was successfully demonstrated with the  $\text{Al}_2\text{O}_3$  protective layer.

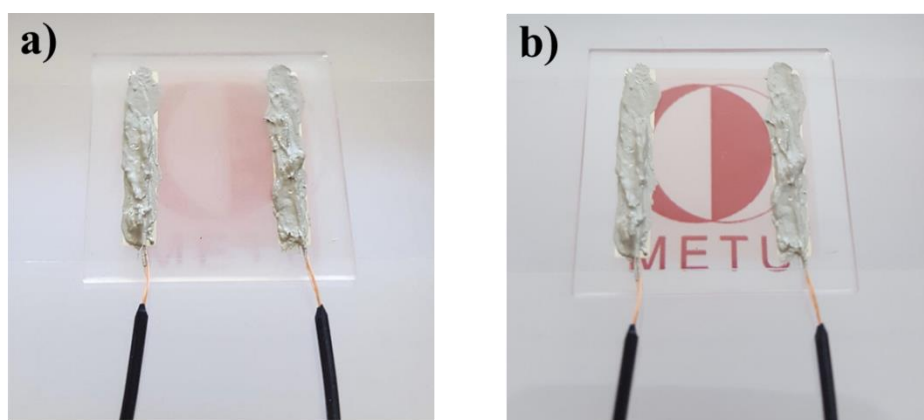


**Figure 3. 22** Photos of the  $5\text{ nm}$   $\text{Al}_2\text{O}_3$  deposited Cu NW network with an amount of  $68.8\text{ mg/m}^2$  (a) before and (b) after defrosting application.

### 3.5. Zinc Oxide Deposited Copper Nanowire Networks

ZnO deposition was also investigated onto Cu NW networks. Similar to Al<sub>2</sub>O<sub>3</sub> case ZnO thin films were conformally deposited using ALD method. The use of ZnO on Cu NWs is highly promising not only for TTFHs but also for optoelectronics since ZnO is a semiconductor. Therefore, in the forthcoming layers in an optoelectronic device charge injection and transfer will not be problematic. On the other hand, ZnO deposited Cu NWs have not been used as TTFHs to the best of our knowledge.

Cu NW networks with 4 different ZnO thicknesses (5, 15, 25 and 50 nm) were prepared to investigate the effect of ZnO thickness on the protection level and thermal response of Cu NWs. The SEM and TEM images of an individual 50 nm ZnO deposited Cu NW are provided in Figures 3.23 (a) and (b), respectively.

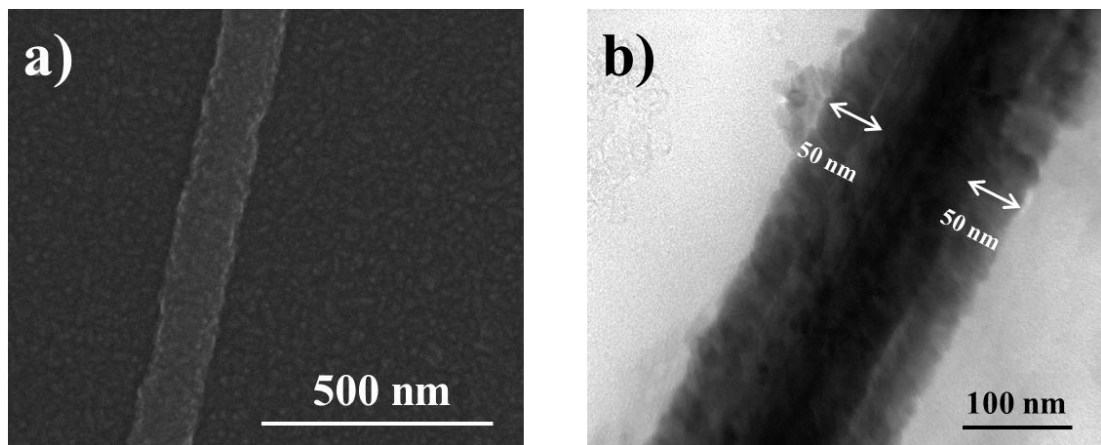


**Figure 3. 23** (a) SEM and (b) TEM images of an individual 50 nm ZnO deposited Cu NW.

It was observed from Figure 3.23 that the surface of the Cu NWs upon ZnO deposition was a lot rougher compared to Al<sub>2</sub>O<sub>3</sub> deposited ones (Figure 3.11). Although, definite boundaries of Cu NW and ZnO was not revealed by the SEM image (Figure 3.23 (a)), the core shell structure was clearly observed from the TEM image (Figure 3.23 (b)). To compare the roughness of the oxide deposited networks,

AFM analysis was conducted on bare  $\text{Al}_2\text{O}_3$  and ZnO thin films with different thicknesses of 5, 15, 25 and 50 nm. Topographical 3D and 2D AFM images of  $\text{Al}_2\text{O}_3$  and ZnO thin films with 50 nm thicknesses are provided in Figures 3.24 (a) – (d).

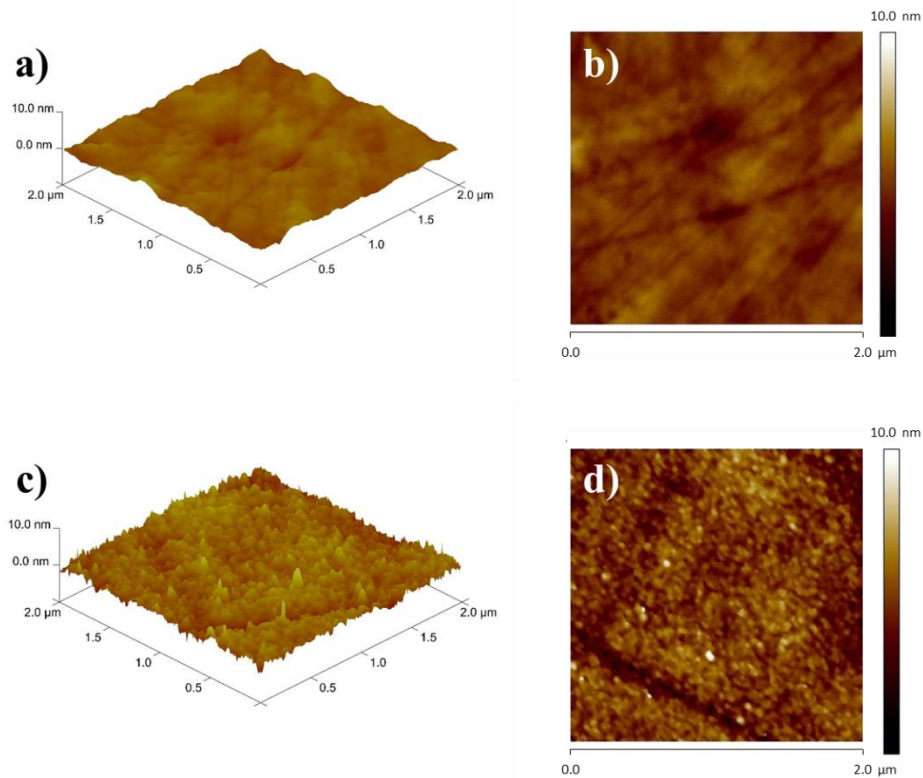


**Figure 3. 24** (a) 3D and (b) 2D topographical AFM images of  $\text{Al}_2\text{O}_3$  thin film. (c) 3D and (d) 2D topographical AFM images of ZnO thin film.

It is evident from Figure 3.24 that the surface of  $\text{Al}_2\text{O}_3$  thin film was a lot smoother than the ZnO thin film. In agreement with the SEM and TEM images, surface of ZnO thin film is rougher (Figure 3.24).  $R_a$  (average roughness) and RMS (root mean square roughness) values of 50 nm  $\text{Al}_2\text{O}_3$  thin films were 0.385 and 0.504 nm, respectively. On the other hand,  $R_a$  and RMS values of 50 nm ZnO thin films were 0.719 and 0.917 nm, respectively. Both surface roughness values ( $R_a$  and RMS) of ZnO thin films were higher than those for  $\text{Al}_2\text{O}_3$  thin films. This phenomenon was

found to be valid for all oxide thicknesses.  $R_a$  and RMS values of  $Al_2O_3$  and ZnO thin films with different oxide thicknesses are tabulated and provided in Table 3.3.

**Table 3.3**  $R_a$  and RMS values of  $Al_2O_3$  and ZnO thin films with different thicknesses.

	<b>Oxide Type</b>			
	<b><math>Al_2O_3</math></b>		<b>ZnO</b>	
<b>Oxide Thickness (nm)</b>	<b><math>R_a</math> (nm)</b>	<b>RMS (nm)</b>	<b><math>R_a</math> (nm)</b>	<b>RMS (nm)</b>
5	0.672	0.987	1.04	1.42
15	0.460	0.611	0.506	0.659
25	0.309	0.398	0.638	0.826
50	0.385	0.504	0.719	0.917

It is observed from Table 3.3 that for all oxide thicknesses,  $R_a$  and RMS values of ZnO thin films were higher than that of  $Al_2O_3$  thin films. The roughness of  $Al_2O_3$  thin films were found to decrease up to 25 nm thickness and then increased for higher thicknesses. On the other hand, the roughness of ZnO thin films were decreased down to 15 nm thickness and then increased for higher thicknesses. A linear relationship could not be obtained between the thin film roughness and thickness. To decrease the surface roughness of ZnO thin films, the effect of different deposition parameters were investigated. Lower surface roughnesses were achieved by tuning the pulsing times of the precursors. The lowest surface roughness value

was achieved for 15 ms injections of both DEZ and H<sub>2</sub>O precursors. However, only 50 ms injections of both DEZ and H<sub>2</sub>O precursors were utilized in this work.

Similar results (to Al<sub>2</sub>O<sub>3</sub> deposited Cu NW networks) were obtained in the sheet resistance and optical transmittance of ZnO deposited Cu NW networks. The sheet resistance of the networks remained the same upon ZnO deposition, since ZnO was deposited conformally on already percolating and annealed networks. The transmittance (at 550 nm) of the networks decreased with increasing ZnO thickness due to an overall increase in the diameter of the NWs and the change in effective refractive index. Visible spectral transmittance for the networks with an amd of 40.7 mg/m<sup>2</sup> with different ZnO thicknesses is provided in Figure 3.25. It was observed from Figure 3.12 and Figure 3.25 that, even though the surface smoothness and refractive indexes of Al<sub>2</sub>O<sub>3</sub> and ZnO thin films were different, decreases in transmittance at a wavelength of 550 nm were similar.

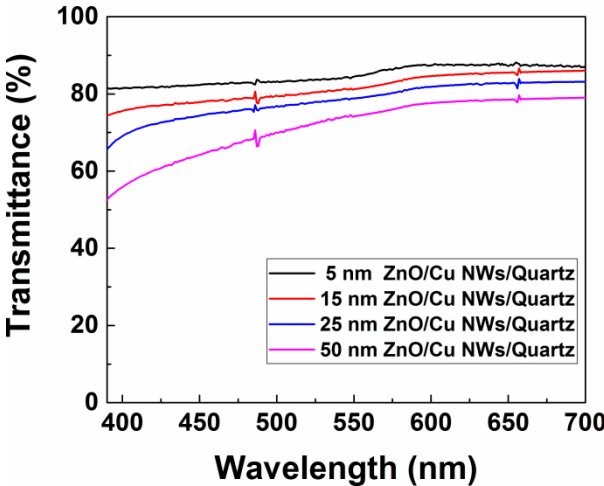


**Figure 3. 25** Spectral transmittance of Cu NW networks with an amd of 40.7 mg/m<sup>2</sup> and different ZnO thicknesses of 5, 15, 25 and 50 nm.

Refractive index ( $n$ ) as another important optical parameter was calculated for the oxide thin films.  $\text{Al}_2\text{O}_3$  and ZnO thin films on quartz substrates were used for these calculations. The refractive index ( $n$ ) of  $\text{Al}_2\text{O}_3$  and ZnO thin films as a function of wavelength with 80 nm oxide thicknesses are provided in Figures 3.26 (a) and (b), respectively.

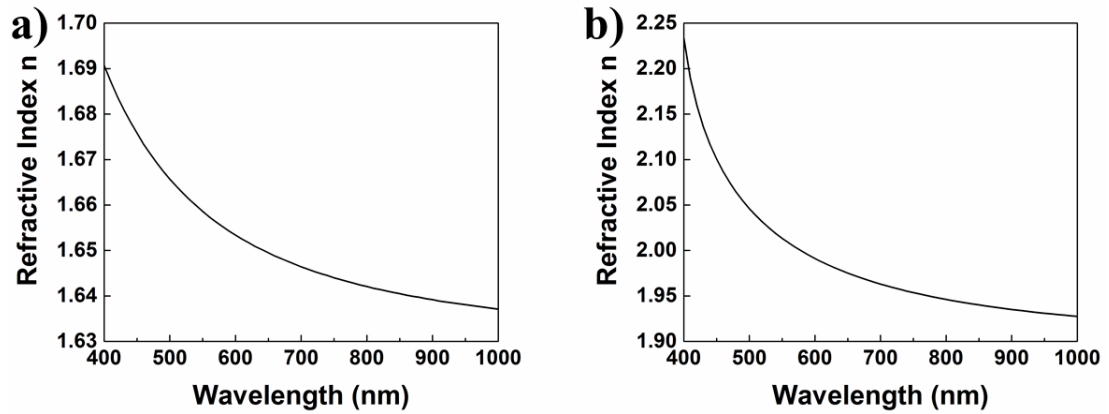


**Figure 3. 26** Refractive index ( $n$ ) as a function of the wavelength for (a)  $\text{Al}_2\text{O}_3$  and (b) ZnO thin films.

It is observed from Figure 3.26 that the refractive index ( $n$ ) of both oxides shows a decreasing trend with increasing wavelength. The refractive index ( $n$ ) of ZnO thin film was higher than that of  $\text{Al}_2\text{O}_3$  thin film for all wavelengths. These values were in agreement with the ones reported in literature [112] [113]. The refractive index ( $n$ ) of  $\text{Al}_2\text{O}_3$  and ZnO thin films at 550 nm are 1.66 and 2.01, respectively. This means that the refraction of light is more pronounced when it is incident onto ZnO deposited Cu NW networks compared to the  $\text{Al}_2\text{O}_3$  deposited counterparts.

XRD analysis of the oxides was performed to determine their crystal structure. The GIXD patterns for bare  $\text{Al}_2\text{O}_3$  and ZnO thin films with 100 nm oxide thicknesses are provided in Figures 3.27 (a) and (b), respectively.

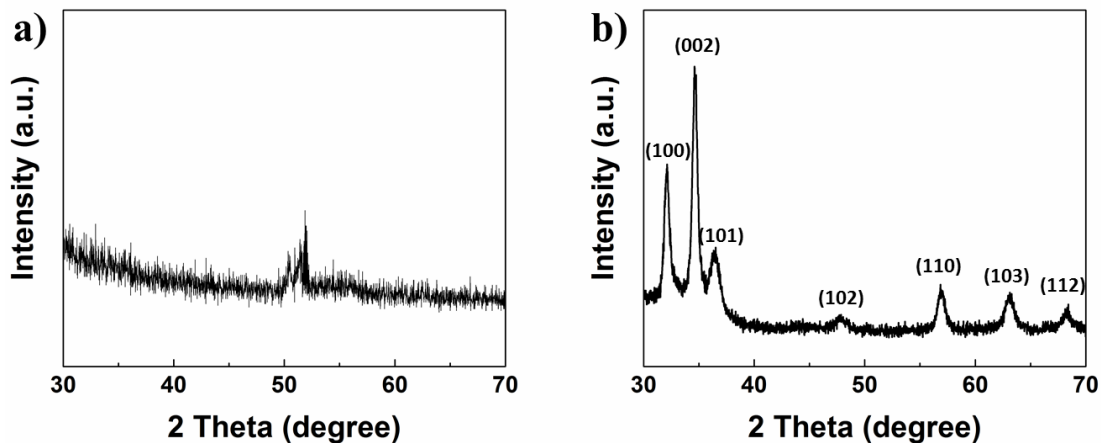


**Figure 3. 27** GIXD patterns for bare (a) Al<sub>2</sub>O<sub>3</sub> and (b) ZnO thin films on quartz substrates.

It is evident from Figure 3.27 (a) that the degree of crystallinity for Al<sub>2</sub>O<sub>3</sub> thin films were remarkably low since there are no distinct and high intensity peaks in the GIXD pattern. On the other hand, ZnO thin films were highly crystalline (Figure 3.27 (b)). The 2θ peaks corresponds to (100), (002), (101), (102), (110), (103) and (112) planes of polycrystalline wurtzite structure of ZnO (JCPDS 36-1451) [114].

The chemical analysis of ZnO deposited Cu NW networks were performed by XPS. XPS spectra of 5 nm ZnO deposited Cu NW network are provided in Figure 3.28.

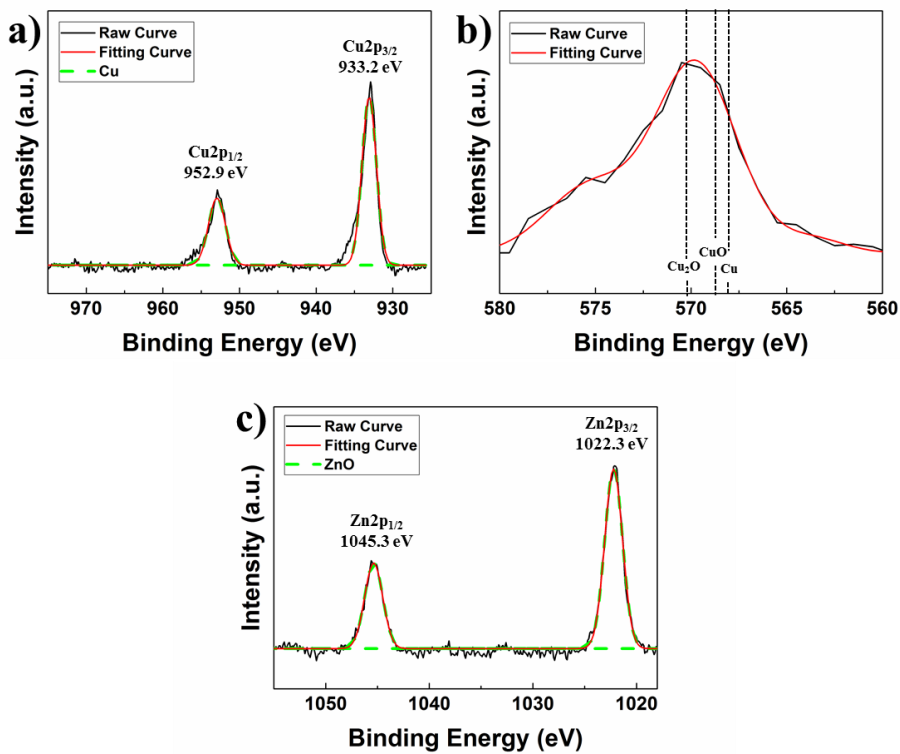


**Figure 3. 28** XPS spectra of (a) Cu<sub>2p<sub>1/2</sub></sub> and Cu<sub>2p<sub>3/2</sub></sub>, (b) Cu LMM Auger, and (c) Zn<sub>p<sub>1/2</sub></sub> and Zn<sub>p<sub>3/2</sub></sub> of 5 nm ZnO deposited Cu NW network.

As it is shown in Figure 3.28 (a), Cu<sub>2p<sub>1/2</sub></sub> and Cu<sub>2p<sub>3/2</sub></sub> peaks belong to either metallic Cu or Cu<sub>2</sub>O since the binding energy difference (19.7 eV) between them is lower than 19.8 eV [106]. To differentiate chemical state of Cu, Cu LMM Auger spectra (Figure 3.28 (b)) was used. Cu LMM Auger spectra signifies the presence of Cu<sub>2</sub>O rather than metallic Cu [107]. XRD analysis of the as synthesized Cu NWs and high electrical conductivity of the networks indicate that the oxidation of Cu NWs is not throughout the whole network. The thin layer of Cu<sub>2</sub>O on Cu NWs were developed in the first cycles of ALD due to the use of H<sub>2</sub>O precursor. Moreover, the positions of Zn<sub>p<sub>1/2</sub></sub> (1045.3 eV) and Zn<sub>p<sub>3/2</sub></sub> (1022.3 eV) peaks in Figure 3.28 (c) signifies the oxidation state of Zn compound as ZnO [115].

### 3.5.1. Thermal Measurements

To investigate the effect of ZnO thickness, thermal response of Cu NW networks with different ZnO thicknesses were monitored under a constant applied bias. Applied bias was increased with 1 V intervals until the failure of the networks, which was indicated by an increase in the sheet resistance. Similar to before, the bias was applied for 20 minutes and then the networks were allowed to cool to room temperature for 10 minutes. Time dependent thermal response of Cu NW networks with an amd of  $40.7 \text{ mg/m}^2$  with different ZnO thicknesses are provided in Figures 3.29 (a) – (d).

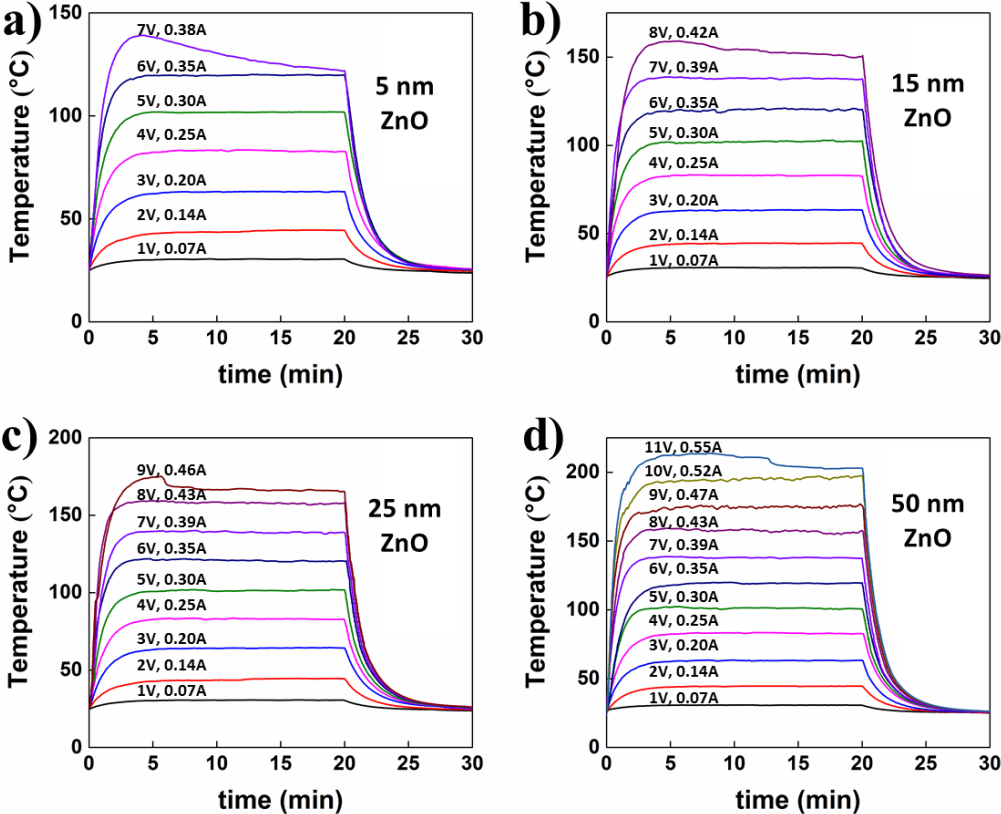


**Figure 3. 29** Time dependent thermal response of ZnO deposited Cu NW networks with an amd of  $40.7 \text{ mg/m}^2$  and different ZnO thicknesses of (a) 5, (b) 15, (c) 25 and (d) 50 nm.

It was observed from Figure 3.29 that the networks attained higher temperatures with an increase in ZnO thickness. This was certainly because thicker ZnO layers provide better protection. To investigate the highest achievable temperatures by Cu NW networks, applied bias was increased until failure of the networks. The gradual temperature decrease was observed in failed networks due to an increase in the sheet resistance. The ZnO shell layer solved rapid oxidation problem of Cu NW networks at elevated temperatures by cutting the interface between NWs and air. Maximum temperatures of 139 °C and 214 °C were attained upon the deposition of 5 and 50 nm ZnO thin films onto Cu NW networks, respectively.

To investigate the effect of NW density on the thermal response of ZnO protected Cu NW networks, thermal measurements of networks with different amds of 73.1 and 101.6 mg/m<sup>2</sup> were performed under a constant applied bias. Time dependent thermal response of 50 nm ZnO deposited Cu NW networks with amds of 73.1 and 101.6 mg/m<sup>2</sup> are provided in Figures 3.30 (a) and (b), respectively.

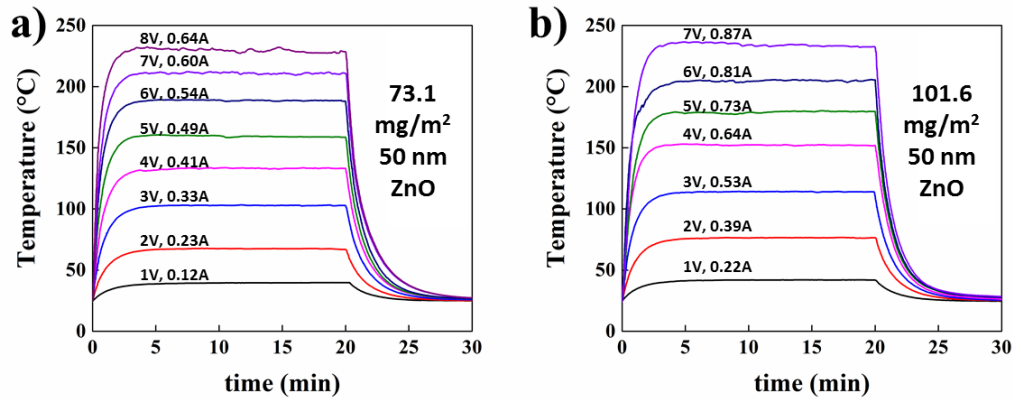


**Figure 3. 30** Time dependent thermal responses under various applied voltages of 50 nm ZnO deposited Cu NW networks with different amds of (a) 73.1 and (b) 101.6 mg/m<sup>2</sup>.

It was observed from Figure 3.29 (d) and Figure 3.30 that the networks with higher NW densities reach slightly higher temperatures compared to the counterparts with lower NW densities. This is because of higher number of alternative pathways in networks with high NW densities. Therefore, sheet resistance was remained the same since charges were transported via alternative pathways. Upon the deposition of 50 nm ZnO onto Cu NW networks with amds of 73.1 and 101.6 mg/m<sup>2</sup> TTFHs reached maximum temperatures of 232 °C and 237 °C, respectively.

The heating and cooling rates of ZnO deposited Cu NW networks were calculated by differentiating thermal response. The heating rate calculations were performed on networks at their highest applied biases. For example, the heating and cooling rates of Cu NW network with an amd of 101.6 mg/m<sup>2</sup> with 50 nm ZnO thickness were found to be 10 °C/s and – 4 °C/s, respectively, under an applied bias of 7 V (corresponding to a current of 0.87A) corresponding to a temperature of 237 °C. Heating and cooling rate as a function of time for this network is provided in Figure 3.31. In average, heating and cooling rates of 12 °C/s and – 5 °C/s were found for ZnO deposited Cu NW networks, respectively. This value is very close to Al<sub>2</sub>O<sub>3</sub> deposited Cu NW networks and it is still considered as a high heating rate when compared to the literature [98].

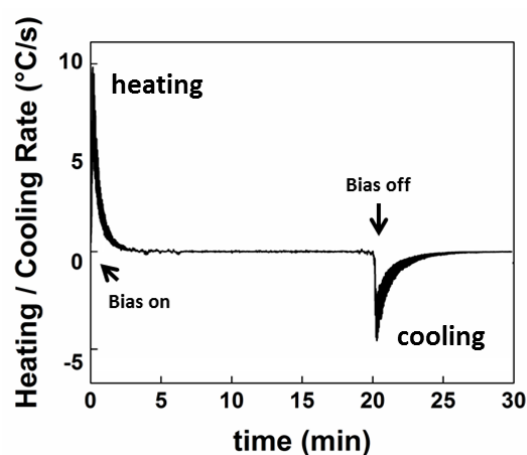


**Figure 3. 31** Heating and cooling rate as a function of time for Cu NW network with an amd of 101.6 mg/m<sup>2</sup> and ZnO thickness of 50 nm under an applied bias of 7 V.

Input power densities of the networks at their highest reproducible and stable temperatures were calculated to investigate the power requirements. Similar to Al<sub>2</sub>O<sub>3</sub> case, the effective sample area was taken as 3.24 cm<sup>2</sup> (1.8 cm x 1.8 cm). The sheet resistance, transmittance (at 550 nm), T<sub>max</sub> and input power density values of ZnO deposited Cu NW networks with different amds and different oxide thicknesses are tabulated and provided in Table 3.4.

**Table 3. 4** Optoelectronic properties and thermal response characteristics of Cu NW networks with different amds and ZnO thicknesses.

amd (mg/m <sup>2</sup> )	Sheet Resistance (Ω /sq)	Al <sub>2</sub> O <sub>3</sub> Thickness (nm)	Transmittance (%) (at 550nm)	T <sub>max</sub> (°C)	Bias at T <sub>max</sub> (V)	Current at T <sub>max</sub> (A)	Input Power Density (W/cm <sup>2</sup> )
40.7	15	5	84.4	119	6	0.35	0.65
		15	81.2	139	7	0.39	0.84
		25	78.8	159	8	0.43	1.06
		50	74.2	194	10	0.52	1.60
73.1	8	5	78.3	124	4	0.41	0.51
		15	75.3	150	5	0.49	0.76
		25	72.6	176	6	0.54	1.00
		50	68.5	201	7	0.60	1.30
101.6	4.8	5	73.5	115	3	0.53	0.49
		15	70.3	152	4	0.64	0.79
		25	67.8	178	5	0.73	1.13
		50	63.2	204	6	0.81	1.50

It is shown in Table 3.2 and Table 3.4 that Al<sub>2</sub>O<sub>3</sub> deposited networks reached higher temperatures compared to ZnO deposited counterparts. Two networks with nearly identical amd values were compared for Al<sub>2</sub>O<sub>3</sub> (101.2 mg/m<sup>2</sup>) and ZnO (101.6 mg/m<sup>2</sup>) deposition. The sheet resistance, transmittance (at 550 nm), T<sub>max</sub> and input power densities of these networks with different oxide thicknesses are provided in Figures 3.32 (a) – (d). Values of bare networks are also provided for comparison.

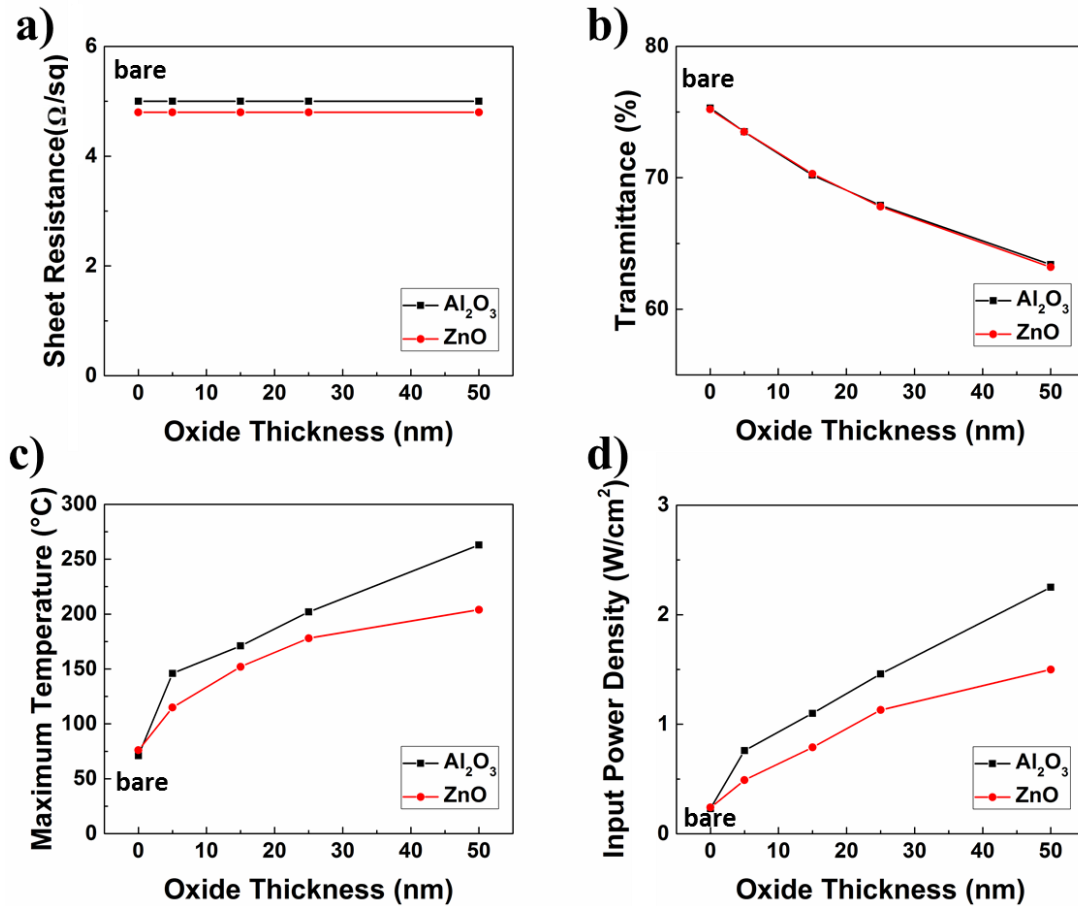


**Figure 3.32** (a) The sheet resistance, (b) transmittance, (c)  $T_{\max}$  and (d) input power densities of Cu NW networks with amds of  $101.2 \text{ mg/m}^2$  (for  $\text{Al}_2\text{O}_3$  deposition) and  $101.6 \text{ mg/m}^2$  (for ZnO deposition) with different oxide thicknesses. Lines are for visual aid.

It is observed from Figure 3.32 (a) that the sheet resistance values of the networks were similar and remain unchanged through oxide deposition. Similar decreases in the transmittance values at a wavelength of 550 nm with oxide different thickness were observed as shown in Figure 3.32 (b). A  $T_{\max}$  of 263 °C and 204 °C were obtained for 50 nm  $\text{Al}_2\text{O}_3$  and ZnO deposited Cu NW networks, respectively.  $T_{\max}$  of  $\text{Al}_2\text{O}_3$  deposited network was higher than that of the ZnO counterpart. This phenomenon was found to be valid for all oxide thicknesses (Figure 3.32 (c)). As a

result of that, the input power densities  $\text{Al}_2\text{O}_3$  deposited networks were found to be higher than that of  $\text{ZnO}$  deposited networks (to reach higher temperatures) for all oxide thicknesses (Figure 3.32 (d)). Therefore,  $\text{Al}_2\text{O}_3$  deposition was provided better protection level for Cu NW networks compared to  $\text{ZnO}$  deposition. This is associated with the roughness and porosity of oxide layers.  $\text{ZnO}$  layer was a lot rougher compared to  $\text{Al}_2\text{O}_3$  layer. Moreover,  $\text{ZnO}$  deposited with ALD is highly porous compared to  $\text{Al}_2\text{O}_3$  deposited with ALD [116]. In literature, corrosion protection of Cu was monitored with ALD deposited  $\text{ZnO}$  and  $\text{Al}_2\text{O}_3$ .  $\text{Al}_2\text{O}_3$  deposited ones showed better protection compared to  $\text{ZnO}$  deposited ones due to high porosity of  $\text{ZnO}$  [117].

### **3.5.2. Failure Mechanism**

The  $\text{ZnO}$  protected Cu NW networks were failed at their highest applied biases, which was indicated by an increase in the sheet resistance. Moreover, at some points, color changes from red brown to black were observed.  $\text{CuO}$  has black color so this indicated that Cu NWs were oxidized to  $\text{CuO}$ . Therefore, to investigate the chemical changes in networks, XPS analysis was performed. XPS spectra of 5 nm  $\text{ZnO}$  deposited Cu NW network at failed points is provided in Figure 3.33.

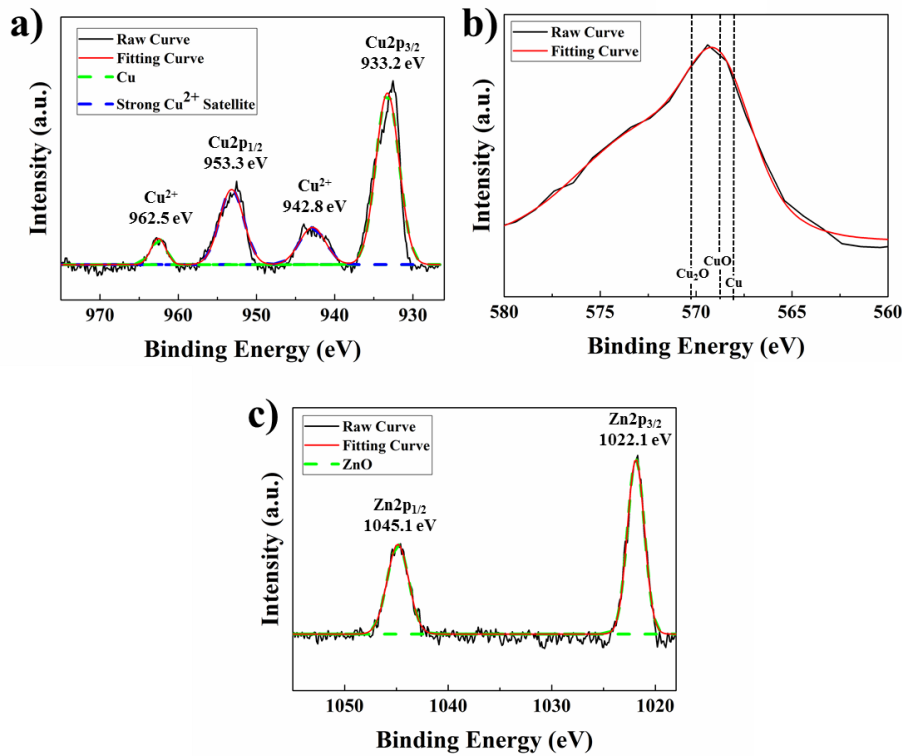


**Figure 3.33** XPS spectra of (a) Cu $2p_{1/2}$  and Cu $2p_{3/2}$ , (b) Cu LMM Auger and (c) Zn $p_{1/2}$  and Zn $p_{3/2}$  of 5 nm ZnO deposited Cu NW network at failed points.

The difference (20.1 eV) between Cu $2p_{1/2}$  (953.3 eV) and Cu $2p_{3/2}$  (933.2 eV) peaks, strong Cu $^{2+}$  satellite peaks (942.8 and 962.5 eV) and CuO peak (568.9 eV) at Cu LMM Auger spectra signify that Cu NWs were oxidized to CuO at failed points [107] [108]. As a result of that, sheet resistance of the failed networks were found to increase. Moreover, Zn $p_{1/2}$  and Zn $p_{3/2}$  peaks signifies the oxidation state of Zn compound as ZnO [115]. Therefore, ZnO did not change its chemical form at failed points.

The morphological analysis of failed points was performed by SEM for all thicknesses. SEM images of Cu NW networks with an amd of 40.7 mg/m<sup>2</sup> and different ZnO thicknesses at failed points are provided in Figures 3.34 (a) – (d).

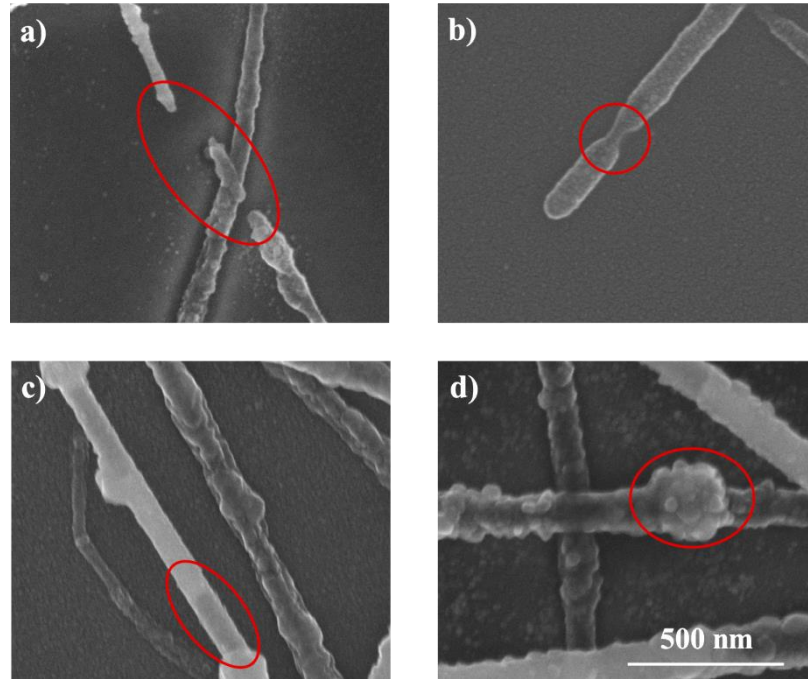


**Figure 3.34** SEM images of Cu NW networks with an areal density of  $40.7 \text{ mg/m}^2$  and ZnO thicknesses of (a) 5, (b) 15, (c) 25 and (d) 50 nm, at failed points.

It is observed from Figure 3.33 and 3.34, the failure mechanism of ZnO protected Cu NWs were both oxidation and Rayleigh instability similar to  $\text{Al}_2\text{O}_3$  protected Cu NWs. However, ZnO protected Cu NWs were found to fail at lower temperatures compared to  $\text{Al}_2\text{O}_3$  protected counterparts. For lower ZnO thicknesses of 5 and 15 nm, thinning and breaking of Cu NWs were observed [74]. Thinning of NWs caused structural deformation on ZnO layer so NWs were separated from the oxide shell and oxidized. Therefore, sheet resistance of networks were increased due to oxidation and failure of Cu NWs. Breaking and thinning of NWs are marked by red circles and provided in Figures 3.34 (a) and (b). For higher ZnO thicknesses of 25 and 50 nm, accumulation of Cu on junction points and breaking of NWs inside the oxide shell were observed [93]. Accumulated Cu on junction points was separated from the oxide shell and get oxidized. Therefore, sheet resistance of the networks were increased due to discontinuities between NWs and oxidation of NWs [111]. The discontinuous parts of NWs and accumulation point are marked by red circles and provided in Figures 3.34 (c) and (d).



## CHAPTER 4

### CONCLUSIONS AND FUTURE RECOMMENDATIONS

#### 4.1. Conclusions

In this thesis oxide shell protected Cu NW networks were utilized as TTFHs. Firstly, Cu NWs were synthesized via a simple solution based method. Oxide free Cu NWs with a mean diameter and length of 50 nm and 25  $\mu\text{m}$  were synthesized in this work, respectively.

Secondly, purified and dispersed Cu NWs were deposited onto quartz substrates through spray deposition. Different NW density networks were prepared to investigate the effect of NW density on the sheet resistance and optical transmittance. Both sheet resistance and transmittance showed decreasing behavior with increasing NW density within the networks. An almost linear decrease in transmittance with increasing NW density in addition to a power law decrease in the sheet resistance of the networks was observed.

Thirdly, thermal response of the networks with different NW densities were measured under constant bias. It was found that bare Cu NW networks only reached to 100  $^{\circ}\text{C}$  regardless of the NW density due to rapid oxidation at elevated temperatures. To solve the oxidation problem of Cu NWs,  $\text{Al}_2\text{O}_3$  and ZnO protection layers were deposited through ALD method at 4 different thicknesses. Cu NW networks with 3 different NW densities were prepared for both  $\text{Al}_2\text{O}_3$  and ZnO deposition. Crystalline structures of  $\text{Al}_2\text{O}_3$  and ZnO thin films resulted as amorphous and polycrystalline wurtzite, respectively. Core / shell structures were observed upon both  $\text{Al}_2\text{O}_3$  and ZnO deposition. The shell layers protected NWs from oxidation and the attained temperatures increased with increasing the shell layer thickness. Cu

NWs with Al<sub>2</sub>O<sub>3</sub> shell showed better thermal characteristics with respect to ZnO shell due to high porosity of the ZnO films. Upon the deposition of only 5 nm oxide shell, networks reached to 153 °C (68.8 mg/m<sup>2</sup>) and 139 °C (40.7 mg/m<sup>2</sup>) for Al<sub>2</sub>O<sub>3</sub> and ZnO deposition, respectively. For the deposition of 50 nm oxide shell, the temperatures were increased to 283°C (68.8 mg/m<sup>2</sup>) and 214 °C (40.7 mg/m<sup>2</sup>) for Al<sub>2</sub>O<sub>3</sub> and ZnO deposition, respectively. However, the optical transmittances of the networks were decreased with increasing oxide shell thickness. The maximum attained temperatures for a 50 nm shell layer of Al<sub>2</sub>O<sub>3</sub> and ZnO were 309 °C (142.0 mg/m<sup>2</sup>) and 237 °C (101.6 mg/m<sup>2</sup>), respectively. The heating rates of Al<sub>2</sub>O<sub>3</sub> and ZnO deposited Cu NWs were calculated as 14 °C/s and 12 °C/s, respectively.

Then, failure mechanisms of shell layer protected Cu NW networks were investigated. It was found that for both Al<sub>2</sub>O<sub>3</sub> and ZnO layers, failure mechanism was the combination of oxidation and Rayleigh instability of Cu NWs.

Finally, further thermal measurements were performed on Al<sub>2</sub>O<sub>3</sub> deposited Cu NWs since their performance was better compared to ZnO protection layer. Repetitive heating and cooling cycles were investigated and thermal response for each cycle was found almost identical for 10 cycles till 175 °C. Long term stability was also investigated and the temperature remained stable for 24 h at a target temperature of 150 °C without any failure. Thermal camera images of the fabricated networks revealed homogeneous temperature distribution at a target temperature of 260 °C. Cu NW networks were utilized for defrosting applications due to high heating rates of the networks. Complete defrosting was obtained under an applied bias of 3 V after 28 s.

#### **4.2. Future Recommendations**

Deposition of Al<sub>2</sub>O<sub>3</sub> and ZnO layers onto Cu NW networks through ALD provided oxidation protection at elevated temperatures for TTFHs. A future study may involve measuring the long term stability of Al<sub>2</sub>O<sub>3</sub> and ZnO deposited Cu NW networks at

room temperature and also at different temperatures and humidity conditions. Moreover, different oxides such as titanium dioxide ( $\text{TiO}_2$ ) or AZO may be deposited onto Cu NW networks and their effect on thermal response may be investigated.

Haze is another important parameter for TTFHs. Haze is defined as the ratio of diffuse transmittance to total transmittance. Metal NW networks suffer from high haze factors. Therefore, haze factors of oxide layer protected Cu NW networks utilized in this work should be measured.

$\text{Al}_2\text{O}_3$  deposited Cu NW network was utilized as defroster in this work due to high heating rates. Different applications utilizing TTFHs developed in this work such as LCD screen awakening at low temperatures will be highly valuable to investigate.

ALD deposition of oxides onto metallic NW networks may decrease the surface roughness of networks by filling empty spaces between the NWs. Although, roughness is not an important factor for TTFHs, it is an important factor for photovoltaics and LEDs. Therefore, the effect of oxide thickness on the roughness of networks can be investigated. This will improve the photovoltaics and LEDs utilizing Cu NW networks. These devices can be fabricated and their performance can be examined.

ZnO is an n-type semiconductor and its deposition onto Cu NW networks is highly important also in terms of optoelectronic devices. Relatively lower  $T_{\text{max}}$  for ZnO deposited Cu NW network TTFHs was attributed to the porosity of the oxide film. Therefore, ALD parameters to minimize porosity upon deposition onto Cu NW networks will be very important to investigate.



## REFERENCES

- [1] M. Chen, Z. L. Pei, X. Wang, Y. H. Yu, X. H. Liu, and C. Sun, “Intrinsic limit of electrical properties,” *J. Phys. D. Appl. Phys.*, vol. 33, pp. 2538–2548, 2000.
- [2] A. Klein, C. Körber, A. Wachau, F. Säuberlich, Y. Gassenbauer, S. P. Harvey, D. E. Proffit, and T. O. Mason, “Transparent conducting oxides for photovoltaics: Manipulation of fermi level, work function and energy band alignment,” *Materials (Basel)*., vol. 3, no. 11, pp. 4892–4914, 2010.
- [3] P. Barquinha, R. Martins, L. Pereira, and E. Fortunato, *Transparent Oxide Electronics: From Materials to Devices*. 2012.
- [4] Z. Wu, Z. Chen, X. Du, J. M. Logan, J. Sippel, M. Nikolou, K. Kamaras, J. R. Reynolds, D. B. Tanner, A. F. Hebard, and A. G. Rinzler, “Transparent, conductive carbon nanotube films,” *Science (80-. )*., vol. 305, no. 5688, pp. 1273–1276, 2004.
- [5] L. Liu, Y. Cheng, X. Zhang, Y. Shan, X. Zhang, W. Wang, and D. Li, “Graphene-based transparent conductive films with enhanced transmittance and conductivity by introducing antireflection nanostructure,” *Surf. Coatings Technol.*, vol. 325, pp. 611–616, 2017.
- [6] C. F. Guo and Z. Ren, “Flexible transparent conductors based on metal nanowire networks,” *Mater. Today*, vol. 18, no. 3, pp. 143–154, 2015.
- [7] S. Coskun, E. Selen Ates, and H. Emrah Unalan, “Optimization of silver nanowire networks for polymer light emitting diode electrodes,” *Nanotechnology*, vol. 24, no. 12, 2013.
- [8] Q. Dai, L. Zhu, J. Sun, X. Zhang, and Y. Wang, “Organic photodetectors based on transparent electrodes for application in ultraviolet light detection,” *Sci. China Technol. Sci.*, vol. 55, no. 6, pp. 1551–1555, 2012.
- [9] R. A. Maniyara, V. K. Mkhitarian, T. L. Chen, D. S. Ghosh, and V. Pruneri, “An antireflection transparent conductor with ultralow optical loss (<2 %) and

- electrical resistance ( $<6\Omega\text{sq}^{-1}$ ),” *Nat. Commun.*, vol. 7, pp. 1–8, 2016.
- [10] C. Hudaya, B. J. Jeon, and J. K. Lee, “High thermal performance of SnO<sub>2</sub>:F thin transparent heaters with scattered metal nanodots,” *ACS Appl. Mater. Interfaces*, vol. 7, no. 1, pp. 57–61, 2015.
- [11] Y. Kim, H. R. Lee, T. Saito, and Y. Nishi, “Ultra-thin and high-response transparent and flexible heater based on carbon nanotube film,” *Appl. Phys. Lett.*, vol. 110, no. 15, 2017.
- [12] J. J. Bae, S. C. Lim, G. H. Han, Y. W. Jo, D. L. Doung, E. S. Kim, S. J. Chae, T. Q. Huy, N. Van Luan, and Y. H. Lee, “Heat dissipation of transparent graphene defoggers,” *Adv. Funct. Mater.*, vol. 22, no. 22, pp. 4819–4826, 2012.
- [13] J. Li, J. Liang, X. Jian, W. Hu, J. Li, and Q. Pei, “A flexible and transparent thin film heater based on a silver nanowire/heat-resistant polymer composite,” *Macromol. Mater. Eng.*, vol. 299, no. 11, pp. 1403–1409, 2014.
- [14] Y. H. Yoon, J. W. Song, D. Kim, J. Kim, J. K. Park, S. K. Oh, and C. S. Han, “Transparent film heater using single-walled carbon nanotubes,” *Adv. Mater.*, vol. 19, no. 23, pp. 4284–4287, 2007.
- [15] H. Y. Lu, C. Y. Chou, J. H. Wu, J. J. Lin, and G. S. Liou, “Highly transparent and flexible polyimide-AgNW hybrid electrodes with excellent thermal stability for electrochromic applications and defogging devices,” *J. Mater. Chem. C*, vol. 3, no. 15, pp. 3629–3635, 2015.
- [16] L. R. Shobin and S. Manivannan, “Enhancement of electrothermal performance in single-walled carbon nanotube transparent heaters by room temperature post treatment,” *Sol. Energy Mater. Sol. Cells*, vol. 174, no. August 2017, pp. 469–477, 2018.
- [17] N. Tiwari, Ankit, M. Rajput, M. R. Kulkarni, R. A. John, and N. Mathews, “Healable and flexible transparent heaters,” *Nanoscale*, vol. 9, no. 39, pp. 14990–14997, 2017.
- [18] S. Sorel, D. Bellet, and J. N. Coleman, “Relationship between material properties and transparent heater performance for both bulk-like and percolative nanostructured networks,” *ACS Nano*, vol. 8, no. 5, pp. 4805–

4814, 2014.

- [19] C. Celle, C. Mayousse, E. Moreau, H. Basti, A. Carella, and J. P. Simonato, “Highly flexible transparent film heaters based on random networks of silver nanowires,” *Nano Res.*, vol. 5, no. 6, pp. 427–433, 2012.
- [20] R. Gupta, K. D. M. Rao, S. Kiruthika, and G. U. Kulkarni, “Visibly Transparent Heaters,” *ACS Appl. Mater. Interfaces*, vol. 8, no. 20, pp. 12559–12575, 2016.
- [21] H. Liu, V. Avrutin, N. Izyumskaya, Ü. Özgr, and H. Morkoç, “Transparent conducting oxides for electrode applications in light emitting and absorbing devices,” *Superlattices Microstruct.*, vol. 48, no. 5, pp. 458–484, 2010.
- [22] K. Badeker, *Ann. Phys.*, vol. 22, no. 4, p. 749, 1907.
- [23] A. W. Metz, J. R. Ireland, J. G. Zheng, R. P. S. M. Lobo, Y. Yang, J. Ni, C. L. Stern, V. P. Dravid, N. Bontemps, C. R. Kannewurf, K. R. Poepelmeier, and T. J. Marks, “Transparent conducting oxides: Texture and microstructure effects on charge carrier mobility in MOCVD-derived CdO thin films grown with a thermally stable, low-melting precursor,” *J. Am. Chem. Soc.*, 2004.
- [24] D. M. Carballeda-Galicia, R. Castanedo-Pérez, O. Jiménez-Sandoval, S. Jiménez-Sandoval, G. Torres-Delgado, and C. I. Zúñiga-Romero, “High transmittance CdO thin films obtained by the sol-gel method,” *Thin Solid Films*, vol. 371, no. 1, pp. 105–108, 2000.
- [25] A. Walsh, J. L. F. Da Silva, S. H. Wei, C. Körber, A. Klein, L. F. J. Piper, A. Demasi, K. E. Smith, G. Panaccione, P. Torelli, D. J. Payne, A. Bourlange, and R. G. Egdell, “Nature of the band gap of In<sub>2</sub>O<sub>3</sub> revealed by first-principles calculations and X-ray spectroscopy,” *Phys. Rev. Lett.*, vol. 100, no. 16, pp. 2–5, 2008.
- [26] M. Batzill and U. Diebold, “The surface and materials science of tin oxide,” *Prog. Surf. Sci.*, vol. 79, no. 2–4, pp. 47–154, 2005.
- [27] T. Minami, T. Miyata, Presentation given at SPIE, January 23 2008.
- [28] H. Kim, C. M. Gilmore, A. Piqué, J. S. Horwitz, H. Mattoussi, H. Murata, Z. H. Kafafi, and D. B. Chrisey, “Electrical, optical, and structural properties of indium-tin-oxide thin films for organic light-emitting devices,” *J. Appl. Phys.*,

- vol. 86, no. 11, pp. 6451–6461, 1999.
- [29] F. Kurdesau, G. Khripunov, A. F. da Cunha, M. Kaelin, and A. N. Tiwari, “Comparative study of ITO layers deposited by DC and RF magnetron sputtering at room temperature,” *J. Non. Cryst. Solids*, vol. 352, no. 9–20 SPEC. ISS., pp. 1466–1470, 2006.
- [30] Y. Luo, S. Chen, P. Ma, Y. Pu, J. Zhu, J. Zhu, and D. Xiao, “Influence of thickness on electrical and optical property of ITO thin films,” *Yadian Yu Shengguang/Piezoelectrics Acousto-optics*, vol. 32, no. 6, pp. 1–4, 2010.
- [31] K. Im, K. Cho, J. Kim, and S. Kim, “Transparent heaters based on solution-processed indium tin oxide nanoparticles,” *Thin Solid Films*, vol. 518, no. 14, pp. 3960–3963, 2010.
- [32] S. J. Hong, S. J. Cha, J. Y. Lee, and Y. S. Kim, “Improvement of particle size of indium tin oxide nanoparticles by in-situ dispersion method for solution based transparent heater,” *Electron. Mater. Lett.*, vol. 13, no. 1, pp. 37–44, 2017.
- [33] Z. Lin, J. Wang (Eds.). (2014). *Low-cost Nanomaterials Toward Greener and More Efficient Energy Applications*. New York: Springer-Verlag.
- [34] J. W. Bae, S. W. Lee, and G. Y. Yeom, “Doped-Fluorine on Electrical and Optical Properties of Tin Oxide Films Grown by Ozone-Assisted Thermal CVD,” *J. Electrochem. Soc.*, vol. 154, no. 1, p. D34, 2007.
- [35] X. H. Shi and K. J. Xu, “Properties of fluorine-doped tin oxide films prepared by an improved sol-gel process,” *Mater. Sci. Semicond. Process.*, vol. 58, no. June 2016, pp. 1–7, 2017.
- [36] D.-J. Kwak, B.-H. Moon, D.-K. Lee, C.-S. Park, and Y.-M. Sung, “Comparison of transparent conductive indium tin oxide, titanium-doped indium oxide, and fluorine-doped tin oxide films for dye-sensitized solar cell application,” *J. Electr. Eng. Technol.*, vol. 6, no. 5, pp. 684–687, 2011.
- [37] C. Hudaya, J. H. Park, W. Choi, and J. K. Lee, “Characteristics of Fluorine-Doped Tin Oxide as a Transparent Heater on PET Prepared by ECR-MOCVD,” *ECS Trans.*, vol. 53, no. 4, pp. 161–166, 2013.

- [38] H. Y. Liu, V. Avrutin, N. Izyumskaya, M. A. Reshchikov, Ü. Özgür, and H. Morkoç, “Highly conductive and optically transparent GZO films grown under metal-rich conditions by plasma assisted MBE,” *Phys. Status Solidi - Rapid Res. Lett.*, vol. 4, no. 3–4, pp. 70–72, 2010.
- [39] H. Agura, A. Suzuki, T. Matsushita, T. Aoki, and M. Okuda, “Low resistivity transparent conducting Al-doped ZnO films prepared by pulsed laser deposition,” *Thin Solid Films*, vol. 445, no. 2, pp. 263–267, 2003.
- [40] S. M. Park, T. Ikegami, and K. Ebihara, “Effects of substrate temperature on the properties of Ga-doped ZnO by pulsed laser deposition,” *Thin Solid Films*, vol. 513, no. 1–2, pp. 90–94, 2006.
- [41] V. Bhosle, A. Tiwari, and J. Narayan, “Electrical properties of transparent and conducting Ga doped ZnO,” *J. Appl. Phys.*, vol. 100, no. 3, 2006.
- [42] P. H. Chen, W. C. Lai, L. C. Peng, C. H. Kuo, C. L. Yeh, J. K. Sheu, and C. J. Tun, “GaN-based LEDs with AZO:Y upper contact,” *IEEE Trans. Electron Devices*, vol. 57, no. 1, pp. 134–139, 2010.
- [43] B. Du Ahn, S. H. Oh, D. U. Hong, D. H. Shin, A. Moujoud, and H. J. Kim, “Transparent Ga-doped zinc oxide-based window heaters fabricated by pulsed laser deposition,” *J. Cryst. Growth*, vol. 310, no. 14, pp. 3303–3307, 2008.
- [44] M. K. Roul, B. Obasogie, G. Kogo, J. R. Skuza, R. M. Mundle, and A. K. Pradhan, “Transparent and flexible heaters based on Al:ZnO degenerate semiconductor,” *J. Appl. Phys.*, vol. 122, no. 13, pp. 0–8, 2017.
- [45] H. G. Cheong, J. H. Kim, J. H. Song, U. Jeong, and J. W. Park, “Highly flexible transparent thin film heaters based on silver nanowires and aluminum zinc oxides,” *Thin Solid Films*, vol. 589, pp. 633–641, 2015.
- [46] E. Ando and M. Miyazaki, “Moisture resistance of the low-emissivity coatings with a layer structure of Al-doped ZnO/Ag/Al-doped ZnO,” *Thin Solid Films*, vol. 392, no. 2, pp. 289–293, 2001.
- [47] D. Janas and K. K. Koziol, “A review of production methods of carbon nanotube and graphene thin films for electrothermal applications,” *Nanoscale*, vol. 6, no. 6, pp. 3037–3045, 2014.
- [48] M. P. Garrett, I. N. Ivanov, R. A. Gerhardt, A. A. Puretzky, and D. B.

- Geohegan, "Separation of junction and bundle resistance in single wall carbon nanotube percolation networks by impedance spectroscopy," *Appl. Phys. Lett.*, vol. 97, no. 16, 2010.
- [49] E. J. E. Stuart and M. Pumera, "Nanographite impurities of single-walled and double-walled carbon nanotubes are responsible for the observed 'electrocatalytic' effect towards the reduction of azo groups," *Chem. - An Asian J.*, vol. 6, no. 3, pp. 804–807, 2011.
- [50] D. Jung, D. Kim, K. H. Lee, L. J. Overzet, and G. S. Lee, "Transparent film heaters using multi-walled carbon nanotube sheets," *Sensors Actuators, A Phys.*, vol. 199, pp. 176–180, 2013.
- [51] J. Kang, H. Kim, K. S. Kim, S. K. Lee, S. Bae, J. H. Ahn, Y. J. Kim, J. B. Choi, and B. H. Hong, "High-performance graphene-based transparent flexible heaters," *Nano Lett.*, vol. 11, no. 12, pp. 5154–5158, 2011.
- [52] J. W. Suk, A. Kitt, C. W. Magnuson, Y. Hao, S. Ahmed, J. An, A. K. Swan, B. B. Goldberg, and R. S. Ruoff, "Transfer of CVD-grown monolayer graphene onto arbitrary substrates," *ACS Nano*, vol. 5, no. 9, pp. 6916–6924, 2011.
- [53] T.-H. Han, Y. Lee, M.-R. Choi, S.-H. Woo, S.-H. Bae, B. H. Hong, J.-H. Ahn, and T.-W. Lee, "Extremely efficient flexible organic light-emitting diodes with modified graphene anode," *Nat. Photonics*, vol. 6, no. 2, pp. 105–110, 2012.
- [54] S. Bae, H. Kim, Y. Lee, X. Xu, J. S. Park, Y. Zheng, J. Balakrishnan, T. Lei, H. Ri Kim, Y. Il Song, Y. J. Kim, K. S. Kim, B. Özyilmaz, J. H. Ahn, B. H. Hong, and S. Iijima, "Roll-to-roll production of 30-inch graphene films for transparent electrodes," *Nat. Nanotechnol.*, vol. 5, no. 8, pp. 574–578, 2010.
- [55] S. J. Lee, Y. H. Kim, J. K. Kim, H. Baik, J. H. Park, J. Lee, J. Nam, J. H. Park, T. W. Lee, G. R. Yi, and J. H. Cho, "A roll-to-roll welding process for planarized silver nanowire electrodes," *Nanoscale*, vol. 6, no. 20, pp. 11828–11834, 2014.
- [56] X. Wang, G. Kang, B. Seong, I. Chae, H. T. Yudistira, H. Lee, H. Kim, and D. Byun, "Transparent arrays of silver nanowire rings driven by evaporation of sessile droplets," *J. Phys. D. Appl. Phys.*, vol. 50, no. 45, 2017.

- [57] C. H. Liu and X. Yu, "Silver nanowire-based transparent, flexible, and conductive thin film," *Nanoscale Res. Lett.*, vol. 6, no. 1, p. 75, 2011.
- [58] A. M. Bernal, A. M. Ardila, and M. Vega-verdugo, "Fabrication and study of thin transparent conductive films prepared by Spin Coating from metal nanowires," *Mater Sci+*, vol. 132, no. 2, pp. 125–132, 2016.
- [59] V. Scardaci, R. Coull, P. E. Lyons, D. Rickard, and J. N. Coleman, "Spray deposition of highly transparent, low-resistance networks of silver nanowires over large areas," *Small*, vol. 7, no. 18, pp. 2621–2628, 2011.
- [60] D. Bellet, M. Lagrange, T. Sanniccolo, S. Aghazadehchors, V. H. Nguyen, D. P. Langley, D. Muñoz-Rojas, C. Jiménez, Y. Bréchet, and N. D. Nguyen, "Transparent electrodes based on silver nanowire networks: From physical considerations towards device integration," *Materials (Basel)*, vol. 10, no. 6, 2017.
- [61] M. Song, D. S. You, K. Lim, S. Park, S. Jung, C. S. Kim, D. H. Kim, D. G. Kim, J. K. Kim, J. Park, Y. C. Kang, J. Heo, S. H. Jin, J. H. Park, and J. W. Kang, "Highly efficient and bendable organic solar cells with solution-processed silver nanowire electrodes," *Adv. Funct. Mater.*, vol. 23, no. 34, pp. 4177–4184, 2013.
- [62] S. Ye, A. R. Rathmell, I. E. Stewart, Y.-C. Ha, A. R. Wilson, Z. Chen, and B. J. Wiley, "A rapid synthesis of high aspect ratio copper nanowires for high-performance transparent conducting films," *Chem. Commun.*, vol. 50, no. 20, pp. 2562–2564, 2014.
- [63] S. I. White, R. M. Mutiso, P. M. Vora, D. Jahnke, S. Hsu, J. M. Kikkawa, J. Li, J. E. Fischer, and K. I. Winey, "Electrical percolation behavior in silver nanowire-polystyrene composites: Simulation and experiment," *Adv. Funct. Mater.*, vol. 20, no. 16, pp. 2709–2716, 2010.
- [64] R. M. Mutiso, M. C. Sherrott, A. R. Rathmell, B. J. Wiley, and K. I. Winey, "Integrating simulations and experiments to predict sheet resistance and optical transmittance in nanowire films for transparent conductors," *ACS Nano*, vol. 7, no. 9, pp. 7654–7663, 2013.
- [65] K. D. M. Rao and G. U. Kulkarni, "A highly crystalline single Au wire

- network as a high temperature transparent heater,” *Nanoscale*, vol. 6, no. 11, pp. 5645–5651, 2014.
- [66] Y. Sun, B. Gates, B. Mayers, and Y. Xia, “Crystalline Silver Nanowires by Soft Solution Processing,” *Nano Lett.*, vol. 2, no. 2, pp. 165–168, 2002.
- [67] S. Coskun, B. Aksoy, and H. E. Unalan, “Polyol synthesis of silver nanowires: An extensive parametric study,” *Cryst. Growth Des.*, vol. 11, no. 11, pp. 4963–4969, 2011.
- [68] N. V. Nghia, N. N. K. Truong, N. M. Thong, and N. P. Hung, “Synthesis of Nanowire-Shaped Silver by Polyol Process of Sodium Chloride,” *Int. J. Mater. Chem.*, vol. 2, no. 2, pp. 75–78, 2012.
- [69] S. H. Zhang, Z. Y. Jiang, Z. X. Xie, X. Xu, R. Bin Huang, and L. S. Zheng, “Growth of silver nanowires from solutions: A cyclic penta-twinned-crystal growth mechanism,” *J. Phys. Chem. B*, vol. 109, no. 19, pp. 9416–9421, 2005.
- [70] J. Lee, P. Lee, H. Lee, D. Lee, S. S. Lee, and S. H. Ko, “Very long Ag nanowire synthesis and its application in a highly transparent, conductive and flexible metal electrode touch panel,” *Nanoscale*, vol. 4, no. 20, pp. 6408–6414, 2012.
- [71] J. Y. Lee, S. T. Connor, Y. Cui, and P. Peumans, “Solution-processed metal nanowire mesh transparent electrodes,” *Nano Lett.*, vol. 8, no. 2, pp. 689–692, 2008.
- [72] D. P. Langley, M. Lagrange, G. Giusti, C. Jiménez, Y. Bréchet, N. D. Nguyen, and D. Bellet, “Metallic nanowire networks: Effects of thermal annealing on electrical resistance,” *Nanoscale*, vol. 6, no. 22, pp. 13535–13543, 2014.
- [73] S. Nanowire, L. Hu, H. S. Kim, J. Lee, P. Peumans, and Y. Cui, “Scalable Coating and Properties of transparent Ag nanowire,” *ACS Nano*, vol. 4, no. 5, pp. 2955–2963, 2010.
- [74] O. Ergun, S. Coskun, Y. Yusufoglu, and H. E. Unalan, “High-performance, bare silver nanowire network transparent heaters,” *Nanotechnology*, vol. 27, no. 44, 2016.
- [75] Y. Chang, M. L. Lye, and H. C. Zeng, “Large-scale synthesis of high-quality ultralong copper nanowires,” *Langmuir*, vol. 21, no. 9, pp. 3746–3748, 2005.

- [76] Y. Shi, H. Li, L. Chen, and X. Huang, "Obtaining ultra-long copper nanowires via a hydrothermal process," *Sci. Technol. Adv. Mater.*, vol. 6, no. 7, pp. 761–765, 2005.
- [77] H. Guo, N. Lin, Y. Chen, Z. Wang, Q. Xie, T. Zheng, N. Gao, S. Li, J. Kang, D. Cai, and D. L. Peng, "Copper nanowires as fully transparent conductive electrodes," *Sci. Rep.*, vol. 3, 2013.
- [78] M. Mohl, P. Pusztai, A. Kukovecz, Z. Konya, J. Kukkola, K. Kordas, R. Vajtai, and P. M. Ajayan, "Low-temperature large-scale synthesis and electrical testing of ultralong copper nanowires," *Langmuir*, vol. 26, no. 21, pp. 16496–16502, 2010.
- [79] M. Kevin, G. Y. R. Lim, and G. W. Ho, "Facile control of copper nanowire dimensions via the Maillard reaction: Using food chemistry for fabricating large-scale transparent flexible conductors," *Green Chem.*, vol. 17, no. 2, pp. 1120–1126, 2015.
- [80] M. Jin, G. He, H. Zhang, J. Zeng, Z. Xie, and Y. Xia, "Shape-controlled synthesis of copper nanocrystals in an aqueous solution with glucose as a reducing agent and hexadecylamine as a capping agent," *Angew. Chemie - Int. Ed.*, vol. 50, no. 45, pp. 10560–10564, 2011.
- [81] M. Galbiati, A. C. Stoot, D. M. A. Mackenzie, P. Bøggild, and L. Camilli, "Real-time oxide evolution of copper protected by graphene and boron nitride barriers," *Sci. Rep.*, vol. 7, no. 2, pp. 1–7, 2017.
- [82] Y. Won, A. Kim, D. Lee, W. Yang, K. Woo, S. Jeong, and J. Moon, "Annealing-free fabrication of highly oxidation-resistive copper nanowire composite conductors for photovoltaics," *NPG Asia Mater.*, vol. 6, no. 6, pp. e105-9, 2014.
- [83] C. Mayousse, C. Celle, A. Carella, and J.-P. Simonato, "Synthesis and purification of long copper nanowires. Application to high performance flexible transparent electrodes with and without PEDOT:PSS," *Nano Res.*, 2014.
- [84] A. R. Rathmell, M. Nguyen, M. Chi, and B. J. Wiley, "Synthesis of oxidation-resistant cupronickel nanowires for transparent conducting nanowire

- networks,” *Nano Lett.*, vol. 12, no. 6, pp. 3193–3199, 2012.
- [85] I. E. Stewart, S. Ye, Z. Chen, P. F. Flowers, and B. J. Wiley, “Synthesis of Cu-Ag, Cu-Au, and Cu-Pt Core-Shell Nanowires and Their Use in Transparent Conducting Films,” *Chem. Mater.*, vol. 27, no. 22, pp. 7788–7794, 2015.
- [86] L. Shi, R. Wang, H. Zhai, Y. Liu, L. Gao, and J. Sun, “A long-term oxidation barrier for copper nanowires: Graphene says yes,” *Phys. Chem. Chem. Phys.*, vol. 17, no. 6, pp. 4231–4236, 2015.
- [87] L. Dou, F. Cui, Y. Yu, G. Khanarian, S. W. Eaton, Q. Yang, J. Resasco, C. Schildknecht, K. Schierle-Arndt, and P. Yang, “Solution-Processed Copper/Reduced-Graphene-Oxide Core/Shell Nanowire Transparent Conductors,” *ACS Nano*, vol. 10, no. 2, pp. 2600–2606, 2016.
- [88] Z. Chen, S. Ye, I. E. Stewart, and B. J. Wiley, “Copper nanowire networks with transparent oxide shells that prevent oxidation without reducing transmittance,” *ACS Nano*, vol. 8, no. 9, pp. 9673–9679, 2014.
- [89] P. C. Hsu, H. Wu, T. J. Carney, M. T. McDowell, Y. Yang, E. C. Garnett, M. Li, L. Hu, and Y. Cui, “Passivation coating on electrospun copper nanofibers for stable transparent electrodes,” *ACS Nano*, vol. 6, no. 6, pp. 5150–5156, 2012.
- [90] R. H. J. Vervuurt, W. M. M. E. Kessels, and A. A. Bol, “Atomic Layer Deposition for Graphene Device Integration,” *Adv. Mater. Interfaces*, vol. 1700232, p. 1700232, 2017.
- [91] R. W. Johnson, A. Hultqvist, and S. F. Bent, “A brief review of atomic layer deposition: From fundamentals to applications,” *Mater. Today*, vol. 17, no. 5, pp. 236–246, 2014.
- [92] H. H. Khaligh and I. A. Goldthorpe, “Failure of silver nanowire transparent electrodes under current flow,” *Nanoscale Res. Lett.*, vol. 8, no. 1, p. 235, 2013.
- [93] M. E. T. Molaes, A. G. Balogh, T. W. Cornelius, R. Neumann, and C. Trautmann, “Fragmentation of nanowires driven by Rayleigh instability,” *Appl. Phys. Lett.*, vol. 85, no. 22, pp. 5337–5339, 2004.
- [94] J. L. Elechiguerra, L. Larios-Lopez, C. Liu, D. Garcia-Gutierrez, A. Camacho-

- Bragado, and M. J. Yacaman, “Corrosion at the nanoscale: The case of silver nanowires and nanoparticles,” *Chem. Mater.*, vol. 17, no. 24, pp. 6042–6052, 2005.
- [95] X. Zhang, X. Yan, J. Chen, and J. Zhao, “Large-size graphene microsheets as a protective layer for transparent conductive silver nanowire film heaters,” *Carbon N. Y.*, vol. 69, no. 2, pp. 437–443, 2014.
- [96] S. Ji, W. He, K. Wang, Y. Ran, and C. Ye, “Thermal response of transparent silver nanowire/PEDOT:PSS film heaters,” *Small*, vol. 10, no. 23, pp. 4951–4960, 2014.
- [97] W. Lan, Y. Chen, Z. Yang, W. Han, J. Zhou, Y. Zhang, J. Wang, G. Tang, Y. Wei, W. Dou, Q. Su, and E. Xie, “Ultraflexible Transparent Film Heater Made of Ag Nanowire/PVA Composite for Rapid-Response Thermotherapy Pads,” *ACS Appl. Mater. Interfaces*, vol. 9, no. 7, pp. 6644–6651, 2017.
- [98] H. Zhai, R. Wang, X. Wang, Y. Cheng, L. Shi, and J. Sun, “Transparent heaters based on highly stable Cu nanowire films,” *Nano Res.*, vol. 9, no. 12, pp. 3924–3936, 2016.
- [99] C. Celle, A. Cabos, T. Fontecave, B. Laguitton, A. Benayad, L. Guettaz, N. Pélissier, V. H. Nguyen, D. Bellet, D. Muñoz-Rojas, and J. P. Simonato, “Oxidation of copper nanowire based transparent electrodes in ambient conditions and their stabilization by encapsulation: Application to transparent film heaters,” *Nanotechnology*, vol. 29, no. 8, 2018.
- [100] C. Zhu, R. Tan, W. Song, B. Ouyang, M. Cai, S. Zhou, Y. Lu, and N. Li, “A cracked polymer templated Ag network for flexible transparent electrodes and heaters,” *Mater. Res. Express*, vol. 5, no. 6, p. 066427, 2018.
- [101] D. Lordan, M. Burke, M. Manning, A. Martin, A. Amann, D. O’Connell, R. Murphy, C. Lyons, and A. J. Quinn, “Asymmetric Pentagonal Metal Meshes for Flexible Transparent Electrodes and Heaters,” *ACS Appl. Mater. Interfaces*, vol. 9, no. 5, pp. 4932–4940, 2017.
- [102] K. D. M. Rao, R. Gupta, and G. U. Kulkarni, “Fabrication of Large Area, High-Performance, Transparent Conducting Electrodes Using a Spontaneously Formed Crackle Network as Template,” *Adv. Mater. Interfaces*, vol. 1, no. 6,

- pp. 1–7, 2014.
- [103] A. Khan, S. Lee, T. Jang, Z. Xiong, C. Zhang, J. Tang, L. J. Guo, and L. Wen-Di, “High-Performance Flexible Transparent Electrode with an Embedded Metal Mesh Fabricated by Cost-Effective Solution Process,” *Small*, vol. 12, no. 22, pp. 3021–3030, 2016.
- [104] F. Qian, P. C. Lan, T. Olson, C. Zhu, E. B. Duoss, C. M. Spadaccini, and T. Y. J. Han, “Multiphase separation of copper nanowires,” *Chem. Commun.*, vol. 52, no. 78, pp. 11627–11630, 2016.
- [105] M. S. Saterlie, H. Sahin, B. Kavlicoglu, Y. Liu, and O. A. Graeve, “Surfactant effects on dispersion characteristics of copper-based nanofluids: A dynamic light scattering study,” *Chem. Mater.*, vol. 24, no. 17, pp. 3299–3306, 2012.
- [106] J. S. Shaikh, R. C. Pawar, R. S. Devan, Y. R. Ma, P. P. Salvi, S. S. Kolekar, and P. S. Patil, “Synthesis and characterization of Ru doped CuO thin films for supercapacitor based on Bronsted acidic ionic liquid,” *Electrochim. Acta*, vol. 56, no. 5, pp. 2127–2134, 2011.
- [107] C. Toparli, A. Sarfraz, and A. Erbe, “A new look at oxide formation at the copper/electrolyte interface by in situ spectroscopies,” *Phys. Chem. Chem. Phys.*, vol. 17, no. 47, pp. 31670–31679, 2015.
- [108] T. Ghodselahi, M. A. Vesaghi, A. Shafiekhani, A. Baghizadeh, and M. Lameii, “XPS study of the Cu@Cu<sub>2</sub>O core-shell nanoparticles,” *Appl. Surf. Sci.*, vol. 255, no. 5 PART 2, pp. 2730–2734, 2008.
- [109] K. Benchouk, C. E. L. Moctar, J. C. Bernede, S. Marsillac, J. Pouzet, N. Barreau, and M. Emziane, “Growth and physicochemical characterization of CuAlTe<sub>2</sub> films obtained by reaction, induced by annealing, between Cu / Al / Te / Al / Cu . . . Al / Cu / Al / Te layers sequentially deposited,” vol. 4, pp. 1847–1853, 1999.
- [110] S. Yao, J. Cui, Z. Cui, and Y. Zhu, “Soft electrothermal actuators using silver nanowire heaters,” *Nanoscale*, vol. 9, no. 11, pp. 3797–3805, 2017.
- [111] Y. Qin, S. M. Lee, A. Pan, U. Gösele, and M. Knez, “Rayleigh-instability-induced metal nanoparticle chains encapsulated in nanotubes produced by atomic layer deposition,” *Nano Lett.*, vol. 8, no. 1, pp. 114–118, 2008.

- [112] P. Kumar, M. K. Wiedmann, C. H. Winter, and I. Avrutsky, "Optical properties of Al<sub>2</sub>O<sub>3</sub> thin films grown by atomic layer deposition," *Appl. Opt.*, vol. 48, no. 28, pp. 5407–5412, 2009.
- [113] Z. Montiel-Gonzalez, O. A. Castelo-Gonzalez, M. T. Aguilar-Gama, E. Ramirez-Morales, and H. Hu, "Thickness dependent growth of low temperature atomic layer deposited zinc oxide films," *Appl. Therm. Eng.*, vol. 114, pp. 1145–1151, 2017.
- [114] V. P. Dinesh, P. Biji, A. Ashok, S. K. Dhara, M. Kamruddin, A. K. Tyagi, and B. Raj, "Plasmon-mediated, highly enhanced photocatalytic degradation of industrial textile dyes using hybrid ZnO@Ag core-shell nanorods," *RSC Adv.*, vol. 4, no. 103, pp. 58930–58940, 2014.
- [115] N. Gogurla, A. K. Sinha, S. Santra, S. Manna, and S. K. Ray, "Multifunctional Au-ZnO plasmonic nanostructures for enhanced UV photodetector and room temperature NO sensing devices," *Sci. Rep.*, vol. 4, 2014.
- [116] S. Deng, M. Kurttepli, D. J. Cott, S. Bals, and C. Detavernier, "Porous nanostructured metal oxides synthesized through atomic layer deposition on a carbonaceous template followed by calcination," *J. Mater. Chem. A*, vol. 3, no. 6, pp. 2642–2649, 2015.
- [117] J. S. Daubert, G. T. Hill, H. N. Gotsch, A. P. Gremaud, J. S. Ovental, P. S. Williams, C. J. Oldham, and G. N. Parsons, "Corrosion protection of copper using Al<sub>2</sub>O<sub>3</sub>, TiO<sub>2</sub>, ZnO, HfO<sub>2</sub>, and ZrO<sub>2</sub> Atomic layer deposition," *ACS Appl. Mater. Interfaces*, vol. 9, no. 4, pp. 4192–4201, 2017.